



**NAVAL
POSTGRADUATE
SCHOOL**

MONTEREY, CALIFORNIA

DISSERTATION

**TOWARD A MICRO-SCALE ACOUSTIC
DIRECTION-FINDING SENSOR WITH INTEGRATED
ELECTRONIC READOUT**

by

Richard H. Downey

June 2013

Dissertation Supervisor:

Gamani Karunasiri

Approved for public release; distribution is unlimited

THIS PAGE INTENTIONALLY LEFT BLANK

REPORT DOCUMENTATION PAGE

Form Approved
OMB No. 0704-0188

The public reporting burden for this collection of information is estimated to average 1 hour per response, including the time for reviewing instructions, searching existing data sources, gathering and maintaining the data needed, and completing and reviewing the collection of information. Send comments regarding this burden estimate or any other aspect of this collection of information, including suggestions for reducing this burden to Department of Defense, Washington Headquarters Services, Directorate for Information Operations and Reports (0704-0188), 1215 Jefferson Davis Highway, Suite 1204, Arlington, VA 22202-4302. Respondents should be aware that notwithstanding any other provision of law, no person shall be subject to any penalty for failing to comply with a collection of information if it does not display a currently valid OMB control number. **PLEASE DO NOT RETURN YOUR FORM TO THE ABOVE ADDRESS.**

1. REPORT DATE (DD-MM-YYYY) 21-5-2013			2. REPORT TYPE Dissertation		3. DATES COVERED (From — To) 2010-07-01—2013-06-21	
4. TITLE AND SUBTITLE Toward a micro-scale acoustic direction-finding sensor with integrated electronic readout					5a. CONTRACT NUMBER	
					5b. GRANT NUMBER HIS-0610185, H98230117581	
					5c. PROGRAM ELEMENT NUMBER	
6. AUTHOR(S) Richard H. Downey					5d. PROJECT NUMBER	
					5e. TASK NUMBER	
					5f. WORK UNIT NUMBER	
7. PERFORMING ORGANIZATION NAME(S) AND ADDRESS(ES) Naval Postgraduate School Monterey, CA 93943					8. PERFORMING ORGANIZATION REPORT NUMBER	
9. SPONSORING / MONITORING AGENCY NAME(S) AND ADDRESS(ES) Department of the Navy					10. SPONSOR/MONITOR'S ACRONYM(S)	
					11. SPONSOR/MONITOR'S REPORT NUMBER(S)	
12. DISTRIBUTION / AVAILABILITY STATEMENT Approved for public release; distribution is unlimited						
13. SUPPLEMENTARY NOTES						
14. ABSTRACT Several advances are made toward a microelectromechanical (MEMS) acoustic direction-finding sensor based on the <i>Ormia ochracea</i> fly's ear. First, linear elastic stiffness models are presented and then validated by using a nanoindenter to measure the sensor's stiffness directly. The measured stiffness is highly linear, and the resonant frequencies are correctly predicted by the models presented. Additional nanoindenter results suggest that the sensor can be exposed to at least 162 decibel sound pressure level with no loss of function. Next, an improved capacitive readout system using branched comb fingers is presented. This design is shown to double electrical sensitivity to motion. Finally, it is shown that residual stress-induced curvature in the sensors greatly reduces their sensitivity by effectively shrinking the readout capacitors. A simple model of this curvature is presented and then verified by measurements. This model offers an extremely straightforward means of predicting curvature in similarly fabricated structures. It is also shown that perforations in the sensor's structure have no effect on curvature. The results presented here provide several essential tools for the continued development of the MEMS acoustic direction-finding sensor.						
15. SUBJECT TERMS MEMS, Microelectromechanical, Sensor, Acoustic, Sound, Directional, Direction-finding, Ormia ochracea.						
16. SECURITY CLASSIFICATION OF:			17. LIMITATION OF ABSTRACT UU	18. NUMBER OF PAGES 109	19a. NAME OF RESPONSIBLE PERSON	
a. REPORT Unclassified	b. ABSTRACT Unclassified	c. THIS PAGE Unclassified			19b. TELEPHONE NUMBER (include area code)	

THIS PAGE INTENTIONALLY LEFT BLANK

Approved for public release; distribution is unlimited

**TOWARD A MICRO-SCALE ACOUSTIC DIRECTION-FINDING SENSOR WITH
INTEGRATED ELECTRONIC READOUT**

Richard H. Downey
Commander, United States Navy
B.S., Physics, Massachusetts Institute of Technology, 1994
M.S., Physics, University of Illinois, 2003
Submitted in partial fulfillment of the
requirements for the degree of
DOCTOR OF PHILOSOPHY IN APPLIED PHYSICS
from the
NAVAL POSTGRADUATE SCHOOL
June 2013

Author: _____
Richard H. Downey

Approved by: _____
Gamani Karunasiri
Professor of Physics
Dissertation Advisor

Luke Brewer
Associate Professor of
Mechanical & Aerospace
Engineering

Bruce Denardo
Associate Professor of
Physics

Daphne Kapolka
Senior Lecturer of Physics

James Luscombe
Professor of Physics

Approved by: _____
Andres Larraza
Chair, Department of Physics

Approved by: _____
Douglas Moses
Vice Provost for Academic Affairs

THIS PAGE INTENTIONALLY LEFT BLANK

ABSTRACT

Several advances are made toward a microelectromechanical (MEMS) acoustic direction-finding sensor based on the *Ormia ochracea* fly's ear. First, linear elastic stiffness models are presented and then validated by using a nanoindenter to measure the sensor's stiffness directly. The measured stiffness is highly linear, and the resonant frequencies are correctly predicted by the models presented. Additional nanoindenter results suggest that the sensor can be exposed to at least 162 decibel sound pressure level with no loss of function. Next, an improved capacitive readout system using branched comb fingers is presented. This design is shown to double electrical sensitivity to motion. Finally, it is shown that residual stress-induced curvature in the sensors greatly reduces their sensitivity by effectively shrinking the readout capacitors. A simple model of this curvature is presented and then verified by measurements. This model offers an extremely straightforward means of predicting curvature in similarly fabricated structures. It is also shown that perforations in the sensor's structure have no effect on curvature. The results presented here provide several essential tools for the continued development of the MEMS acoustic direction-finding sensor.

THIS PAGE INTENTIONALLY LEFT BLANK

Table of Contents

1	Introduction	1
1.1	The state of the art	1
1.2	A brief description of the sensor	2
1.3	Overview of present research	4
2	Nanoindenter measurements validate linear elastic stiffness models	7
2.1	Linear elastic models.	9
2.2	Nanoindenter measurements	16
2.3	Conclusions	23
3	Branched comb fingers improve sensitivity to out-of-plane motion	25
3.1	Measurements	26
3.2	Discussion	31
3.3	Conclusions	38
4	Residual stress-generated curvature reduces sensitivity	39
4.1	Predicting curvature	39
4.2	Can perforations affect curvature?.	45
4.3	Electrical sensitivity and capacitor overlap	49
4.4	Conclusions	52
5	Conclusion	55
	Appendices	57

A	Sensor dimensions	57
B	COMSOL Multiphysics models	59
B.1	Recommended COMSOL techniques	59
B.2	Models used in this project	63
C	Wire bonding	69
C.1	Wire bonder parts	70
C.2	Bonding parameters	70
C.3	Normal operation techniques.	72
C.4	When something goes wrong	73
C.5	Conclusion.	74
D	MS3110 capacitive readout integrated circuit	75
E	Light and the sound sensor	77
F	Analytical treatment of fringe fields	79
F.1	Small displacement	80
F.2	Large displacement, large overlap.	81
F.3	Large displacement, small overlap	82
	List of References	85
	Initial Distribution List	91

List of Figures

Figure 1.1	A typical sensor	3
Figure 1.2	Depiction of vibrational modes	4
Figure 2.1	Photograph of the sensor	8
Figure 2.2	Bending mode model	10
Figure 2.3	Rocking mode model	11
Figure 2.4	Flexing mode models	13
Figure 2.5	Stiffness components	14
Figure 2.6	Nanoindenter schematic	17
Figure 2.7	Sample nanoindenter tests	18
Figure 2.8	Comparisons between models and nanoindenter measurements	19
Figure 2.9	Nanoindenter measurements with curve fits	20
Figure 2.10	Failure testing	22
Figure 3.1	Sensor with straight comb fingers	26
Figure 3.2	Sensor with branched comb fingers	27
Figure 3.3	Vibration spectra of acoustic DF sensors	28
Figure 3.4	Output waveform from capacitive readout	30
Figure 3.5	Electronic spectra of acoustic DF sensors	31
Figure 3.6	Sketch of comb fingers showing offset	32

Figure 3.7	Two-plate model of offset comb fingers	33
Figure 3.8	Numerical capacitance models	35
Figure 3.9	Capacitance vs. offset according to models	36
Figure 4.1	Sketch of circular curvature	40
Figure 4.2	Offset measurement photos	40
Figure 4.3	Offset measurement positions	41
Figure 4.4	Gen. 9 curvature	42
Figure 4.5	Gen. 6 curvature	42
Figure 4.6	Gen. 7 curvature	43
Figure 4.7	Sketch of perforations	46
Figure 4.8	Curvature simulation, deformation plot	48
Figure 4.9	Curvature simulation, contour plot	48
Figure 4.10	Curvature radius in COMSOL holes study	49
Figure 4.11	Electronic sensitivity raw measurements	51
Figure 4.12	Normalized electronic sensitivity	52
Figure 4.13	Simulated capacitance with offset, 10 μm vs. 25 μm	53
Figure A.1	Gen. 9 chip layout	58
Figure B.1	COMSOL stiffness model	64
Figure C.1	Kulicke & Soffa wire bonder	69
Figure C.2	Wire bonder closeup	71
Figure C.3	Wire bonder capillary unplugging	72
Figure D.1	MS3110 setup	75
Figure D.2	MS3110 evaluation board	76

List of Tables

Table 2.1	Sensor parameters	9
Table 2.2	Curve fit parameters	21
Table 2.3	Resonant frequencies estimated and measured	21
Table 4.1	Curvature and stress	44
Table 4.2	Normalized sensitivity	53
Table A.1	Gen. 7 and 9 dimensions	57
Table A.2	Branched comb finger dimensions	58

THIS PAGE INTENTIONALLY LEFT BLANK

List of Acronyms and Abbreviations

CGS Centimeter, Gram, Second
DF Direction Finding
FEM Finite Element Model
FWHM Full Width at Half-Maximum
IC Integrated Circuit
MASINT Measurement and Signature Intelligence
MEMS Microelectromechanical Systems
MKS Meter, Kilogram, Second
NCMR National Consortium for MASINT Research
NPS Naval Postgraduate School
rms root mean square
SI Système Internationale
SPAWAR U.S. Navy Space and Naval Warfare Systems Command
SPL Sound Pressure Level

THIS PAGE INTENTIONALLY LEFT BLANK

Acknowledgements

I managed to complete this project only with abundant support and encouragement. This work was funded in part by a National Consortium for MASINT Research (NCMR) grant, and in part by a U.S. Navy Space and Naval Warfare Systems Command (SPAWAR) fellowship.

Many people have given me technical assistance throughout this project. Distinguished Professor Young Kwon provided several helpful discussions on plate bending theory. When I broke electronic equipment (more than once), Sam Barone fixed it for me—and he never complained about my frequent forays into his office for filtered water, other than to suggest a larger bottle. Much of my research would not have been possible without equipment built by George Jaksha and Steve Jacobs. Jay Adeff took the photographs of the sensors in Chapter 3, and Steve Jensen produced the sketch of comb fingers in Fig. 3.6.

I am grateful to the NPS administration for maintaining the delicate balance between military requirements and academic excellence. In particular, I appreciate the work of Daniel Oliver and Leonard Ferrari, who were the NPS president and provost, respectively, during most of my time here. Even if some of their methods have been discredited, their legacy of superior research at NPS makes my degree more meaningful than it would be coming from a less research-focused institution.

This project would have been lonely indeed without the camaraderie and support of my fellow students and researchers. Brian Kearney was especially helpful with problems ranging from questions of theory to techniques of finite element modeling. Fabio Alves was a steady source of wisdom and help in the laboratory, and a model researcher for any graduate student to emulate. Finally, Mike Touse laid the groundwork for my research and introduced me to the laboratory equipment and the project.

I am indebted to the NPS Physics Department faculty for their excellent teaching, which prepared me well for doctoral studies and provided inspiration for my future career as a physics teacher. Particularly inspiring were Bob Armstead's pop quizzes, Brett Borden's probing exam problems, Pete Crooker's methodical lecture presentation, Scott Davis's thorough explanation of difficult textbook passages, Bruce Denardo's and Andres Larraza's wonderful demonstrations, Gamani Karunasiri's relation of abstract concepts to practical applications, and Jim Luscombe's astoundingly elegant lectures and notes.

I also thank my dissertation committee for their academic and professional advice. In particular, Luke Brewer gave many hours of valuable guidance on technical aspects of the work as well as writing, despite his absurdly busy schedule. Most of all, however, I could not have done this work without my dissertation advisor Gamani Karunasiri. He was constantly available for technical help and professional advice, but he also gave me the space to determine my own research direction and do my own work. I was continually inspired by his infectious enthusiasm for this project and the wider field of physics. I thank him also for nominating me for fellowships and awards at every opportunity. Job satisfaction depends primarily on the people you work with, and there could be no better advisor than Professor Karunasiri.

Finally, this work is dedicated to my family. My parents, Zeke and Bobbie Downey, gave me a love of learning and the confidence to try just about anything. My children, George, Eleanor, and James, have inspired me to succeed at work but also to keep my family first. I hope my involvement in this work will help them appreciate learning and the scientific method. Most important, my wife Emily has held our family together with her steadfast love and devotion while I have taken a series of difficult Navy tours including this doctorate degree. And although she would not want me to say I could not have done it without her, it certainly would not have been as much fun.

CHAPTER 1:

Introduction

There is an ongoing effort to develop a low-power, low-cost, lightweight micro-scale acoustic direction-finding sensor inspired by the hearing system of the parasitoid fly *Ormia ochracea*. Such a sensor would have countless applications both civilian and military. Potential uses include hearing aids, communication devices, sniper detection, aerial surveillance, and even monitoring of personnel exposure to Traumatic Brain Injury.

The feature of *Ormia ochracea* that makes it so intriguing is its exquisitely size-efficient directional hearing ability, described in a seminal paper by Miles et al. [1] and subsequent papers by Robert et al. [2, 3]. The fly’s essential feature is that its two eardrums, or tympana, are mechanically coupled by a flexible bridge. In this configuration the tympana can vibrate in two normal modes in response to incident sound: a “bending” mode, in which the tympana vibrate in phase, and a “rocking” mode, in which they vibrate out of phase. When the eardrums are excited by the sound field, the amplitude of the bending mode depends on the sum of the forces acting on the two eardrums, while the rocking mode depends on the difference between the forces [1]. The coupling effectively amplifies the differences in intensity and phase between the two ears, enabling the fly to determine its host’s azimuth to an accuracy of two degrees [4]. A simplified model of the fly ear physics is given by Denny [5].

1.1 The state of the art

Several attempts have been made to develop *Ormia ochracea*-inspired systems, but no one has yet replicated the physics of the fly’s ear in a sensor with fully integrated electronic readout. Some have only partially replicated the fly ear physics by using just one of the two vibration modes, in essence building a pressure-gradient microphone. For example, Miles and Hoy presented a rocking mode-only sensor [6], and Touse et al. presented a bending mode-only sensor [7]. Both of these approaches require an additional reference microphone in order to extract directional information.

Others have presented *Ormia* sensors using a capacitive back-plate readout, as in a condenser microphone, or more commonly an optical readout. A capacitive back-plate polysilicon design was shown by computer simulations to feature the desired interaction between rocking

and bending modes as reported by Gibbons and Miles [8]. This design was awarded a U.S. patent [9]. A similar design was presented by Saito et al. and Ono et al. [10, 11]. However, due to challenges with the capacitive readout, more recent efforts have used optical readout [12]. Several Ormia-type optically read sensors have been reported [13–19]. In particular, Liu, Yu and others have proposed a design consisting of a pair of coupled circular diaphragms with fiber optic interferometric readout [20–24]. A brief review of work up to 2009 was presented by Miles et al. [12]. In related work, Intel Corp. has patented a MEMS directional sound sensor involving two separate microphones with signal processing to artificially increase the phase and time differences between them [25]. The fly’s ear has even inspired radio-frequency direction-finding sensors using electronically coupled antennas analogous to the fly’s mechanically coupled ears [26–28].

Our goal has been to develop a micro-scale acoustic DF sensor that reproduces the essentials of the Ormia physics, with a fully integrated capacitive readout system. Continuing work begun by Touse [29] and others [30–35], the present focus has been understanding the structural mechanics and improving the electrical signal output. This dissertation reports recent progress in those areas.

1.2 A brief description of the sensor

This section briefly introduces the sensor. A more thorough description of its design, fabrication, and operation is given in Touse’s dissertation [29]. The sensor’s structure is a simplified version of the fly’s eardrum, having two relatively stiff wings connected by a bridge that can bend, which is in turn mounted on a pair of legs that can twist. A typical example is shown in Fig. 1.1. The entire “H”-shaped structure is free-standing except at the ends of the legs, and the substrate beneath the structure is etched away so that the wings are free to oscillate out of the device plane. The combination of bridge and legs results in two normal modes of vibration (rocking and bending) analogous to those in the fly’s ear as shown in Fig. 1.2 [29].

To detect the vibration of the wings, it is necessary to read out the nanometer-scale displacements that occur as the wings respond to acoustic signals. As mentioned above, most researchers have employed an optical readout for this purpose, while in some cases a condenser microphone-style capacitive back plate has been proposed. The capacitive readout has the advantage of a much lower profile compared to an optical readout which requires external lasers or fiber optics; however, the condenser microphone type has proven difficult to fabricate [12].

that varies linearly with varying input capacitance [7]. However, the final version of the sensor is intended to have the readout circuitry embedded in the chip with the moving parts, taking full advantage of MEMS technology to produce a truly integrated low-profile device. It is this potential for integration that makes the capacitive readout so attractive.

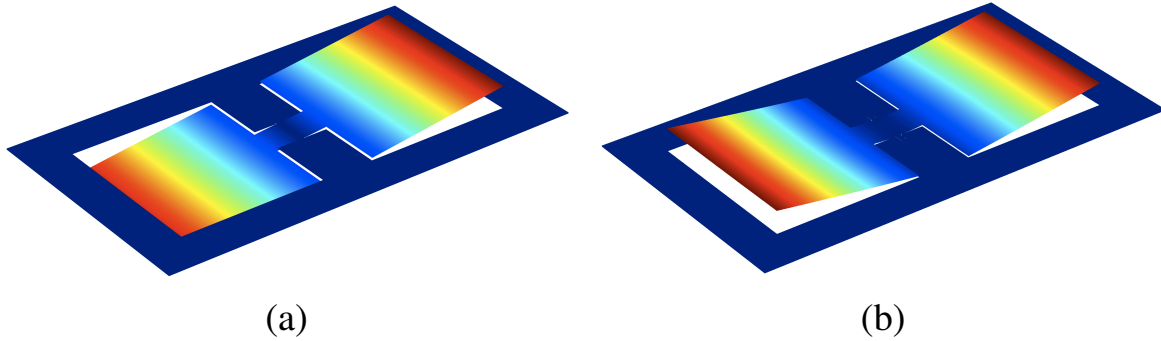


Figure 1.2: The “rocking” mode (a) and “bending” mode (b) of the MEMS sensor, obtained from a COMSOL Multiphysics finite element model. Displacement is greatly exaggerated for clarity; actual displacement of the wingtips is typically much less than one percent of the length of the sensor. Capacitive comb fingers are not shown here.

For the last several generations of development, the sensor and comb fingers have been constructed from the single-crystal silicon device layer of a silicon-on-insulator (SOI) wafer, using the SOI Multi-User MEMS process (SOIMUMPs) [36]. In this process, the device layer used for fabricating the wings and comb fingers is either $10\text{ }\mu\text{m}$ or $25\text{ }\mu\text{m}$ thick, and is mounted on a substrate wafer $400\text{ }\mu\text{m}$ thick with a $1\text{ }\mu\text{m}$ silicon dioxide (glass) layer between.

1.3 Overview of present research

The work presented in the following chapters consists of several advances toward a working *Ormia ochracea*-inspired directional microphone. Each chapter is a more or less self-contained study with its own discussion, results, and conclusions. Methods used include analytical modeling, numerical finite-element modeling, and laboratory observation of fabricated sensor prototypes. In most cases, all three methods have been used together. The results will enable future sensor designs to be optimized in various ways, specifically: by choosing sensor dimensions to get the desired separation between rocking and bending frequencies; by enabling inclusion of larger readout capacitors; and by maximizing the effective capacitor size by reducing the curvature from residual stress.

Chapter 2 presents analytical linear elastic stiffness models that may be used to estimate the rocking and bending frequencies of a sensor, given its dimensions. These models are found to agree with finite-element simulations. Moreover, the models are validated through direct stiffness measurement of the sensor at a series of different locations along its length. Stiffness is measured using a nanoindenter. The same instrument is also used to estimate the maximum sound pressure the sensor can be exposed to without loss of function. Similar techniques could be applied to other MEMS devices with multiple coupled structural components. The content of this chapter has been published in essentially the same form in *Sensors and Actuators A-Physical* [37] and was presented at the American Physical Society March Meeting 2012 [38].

In Chapter 3, a new design of readout capacitor is presented. This design uses branched comb fingers in place of the typical straight fingers. The branched design incorporates a larger number of comb fingers, each of which is much shorter than the corresponding straight fingers. The reduced length makes them more durable, while the greater number increases the overall capacitor size. The new capacitor is modeled analytically and through finite-element simulation. Models and laboratory measurements show that indeed the new design results in a more sensitive readout. Similar branched capacitors could be used in any MEMS device requiring readout of small out-of-plane displacements. The material in this chapter, in substantially the same form, has been submitted to the *Journal of Microelectromechanical Systems* and is presently under review for publication [39].

Chapter 4 investigates residual stress-induced curvature in the acoustic DF sensor. Curvature is important because it reduces the effective size of the wingtip capacitors as the wings curl away from the fixed comb fingers. This size reduction lowers the sensitivity of the readout system. First, it is shown that the curvature is spherical. This is done through analytical and numerical models verified by direct measurement of curvature in different sensors. Next it is shown that perforations in the wings have no effect on curvature. This is done by similar means, using analytical reasoning and computer simulation followed by direct measurement of curvature in sensors with and without holes. Finally, it is shown that a sensor with low curvature is in fact much more sensitive than one with high curvature, when adjusted for the nominal capacitor size. These findings highlight the importance of curvature in the sensor, and suggest that the best way to reduce it without abandoning the SOIMUMPs process is by choosing the thicker 25 μm device layer.

As a group, these findings represent significant progress toward a functioning *Ormia ochracea*-inspired directional sound sensor. The techniques and results presented here can be applied to

produce a more efficient future sensor prototype. The results from Chapter 2 can be used to tune the structure sizes for optimized frequency response in the bending and rocking modes, as well as to estimate tolerance of extreme sound pressures. The findings in Chapter 3 and Chapter 4 together promise an order of magnitude increase in electrical sensitivity. It is sincerely hoped that these advances will result in a future sensor with an electronically detectable, direction-dependent response.

CHAPTER 2:

Nanoindenter measurements validate linear elastic stiffness models

Note: the content of this chapter has been published in substantially the same form in the Elsevier journal Sensors and Actuators A–Physical [37]. Much of this work also was presented at the American Physical Society March Meeting 2012 [38].

In the MEMS acoustic direction-finding sensor, the directionally dependent response is created by the interaction of the bending and rocking vibration modes. To make progress developing a working sensor, it is necessary to understand how the various structural components combine to produce the vibration modes. In particular, to maximize the directional dependence of the sensor, it is essential to be able to optimize the frequency separation between the two modes. To do that, it is necessary to make reasonable estimates of the resonant frequencies of a proposed sensor design. Here, analytical models are presented to estimate resonant frequencies for the two modes, specifically a simple beam bending model for the bending mode and a torsion model for the rocking mode. These models assume linear stiffness of the material under the sensor's expected loading conditions. To validate this assumption and the stiffness models, a nanoindenter is used to directly measure the sensor's stiffness at various points. In addition, the nanoindenter is used to estimate the maximum sound pressure the sensor can tolerate without damage.

Nanoindenters are commonly used on micro-scale cantilever beams to investigate the elasticity and hardness of the beam material as originally described by Weihs et al. [40]. Nanoindenters have also been used to mechanically actuate MEMS components, either to investigate behavior of electrical contacts [41–43], to investigate failure modes of microstructures [44], or to assess mechanical stability [45]. A nanoindenter transducer has even been incorporated into a hand-built apparatus to measure the stiffness of single cantilevers [46]. Here a nanoindenter is used to analyze a more complex MEMS structure whose stiffness varies across its surface due to simultaneous bending and twisting motions of several coupled components—namely the *Ormia ochracea*-inspired acoustic direction-finding sensor.

The sensor used in this study is pictured in Fig. 2.1. It is constructed from the single-crystal (100) silicon device layer of a silicon-on-insulator (SOI) wafer, using the SOIMUMPs standardized commercial micromachining process [36]. The lateral and longitudinal axes of the sensor are oriented along $\langle 110 \rangle$ crystal directions. The silicon layer is nominally 10 μm thick, but was measured to be 9.5 μm thick using a KLA–Tencor AlphaStep D–120 stylus profiler. Notation and values for the sensor parameters are listed in Table 2.1.

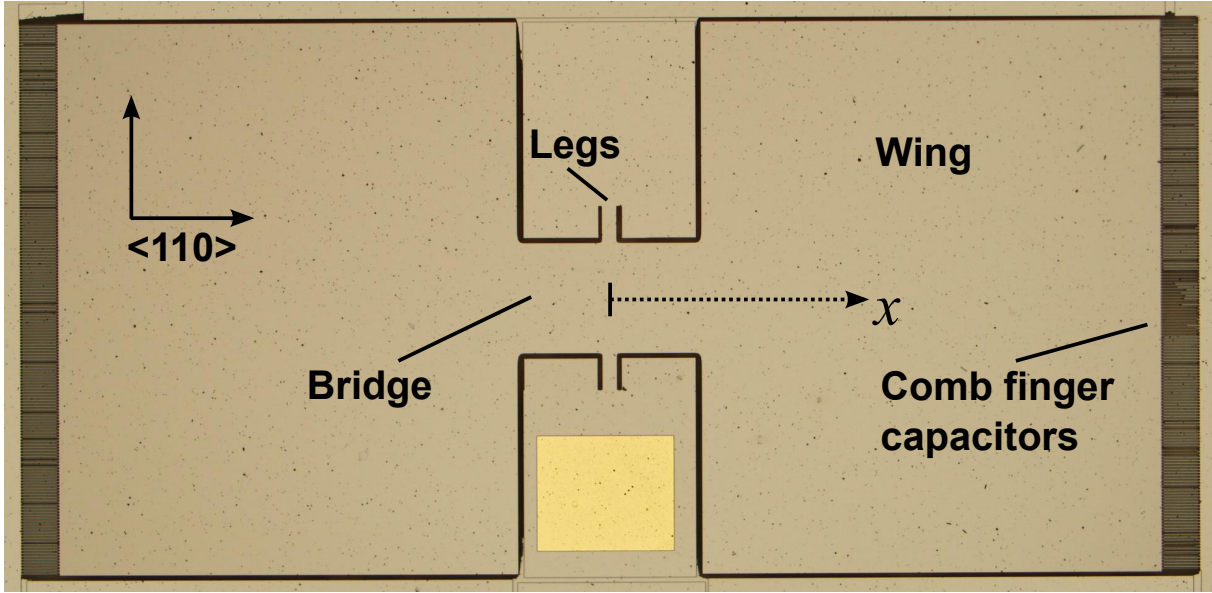


Figure 2.1: A photograph of the sensor used in this study. The two wings are coupled by the bridge, which is connected to the substrate by the legs. The legs act as torsion springs and each end of the bridge acts as a flexible cantilever beam. The sensor is 2.5 mm from wingtip to wingtip.

Since the vibrational response of the sensor depends on the stiffness of the bridge and legs, it is useful to measure the stiffness directly. Spring constants can be determined by measuring resonant frequencies with sound excitation, but for a device with multiple resonance modes, it may be difficult to associate each frequency with the corresponding structures. The advantage of the nanoindenter technique is that it enables precise, direct measurement of stiffness anywhere on the sensor. By comparing the measured stiffness with simple models, it is possible to identify the source of each resonant frequency. The nanoindenter can also be used to explore the maximum loads the sensor can withstand, when it may not be practical to generate such high loads using sound pressure or other means.

In the following, the MEMS sensor's stiffness vs. location of an applied loading force are predicted using analytical and numerical linear elastic models. Those models are used to predict the resonant frequencies, and their validity is checked by comparing with nanoindenter measurements. A nanoindenter test is also used to estimate the maximum sound pressure the sensor can tolerate.

Table 2.1: Sensor parameters. Young's modulus and shear modulus are treated as scalar quantities [47]. The comb finger capacitors are modeled as a 100 μm extension of each wing tip with one quarter the density of silicon.

thickness	t	9.5 μm
bridge length		500 μm
bridge width	w_b	300 μm
leg length	l	100 μm
leg width	w_l	40 μm
wing length		1250 μm
wing width		1500 μm
Young's modulus	E	169 GPa
shear modulus	G	50.9 GPa
density		2330 kg/m^3

2.1 Linear elastic models

The MEMS sensor can be modeled as a collection of springs acting in series. To simplify the analysis, only points along the extended centerline of the bridge (defined as the x axis) are modeled. The overall stiffness $k(x)$ is the individual spring constants $k_i(x)$ added in series:

$$\frac{1}{k(x)} = \sum_i \frac{1}{k_i(x)}. \quad (2.1)$$

The three springs of the sensor model represent bending of the bridge, twisting of the legs, and vertical flexing of the legs and bridge. The vertical flexing does not affect the sensor's operation, but it is important for the nanoindenter study.

2.1.1 The bending mode

To estimate the bending stiffness, the bridge is modeled as a cantilever beam of rectangular cross section, fixed at the legs and free at the point where the load is applied (Figure 2.2). For a

cantilever of width w and thickness $t < w$, acted on by a transverse load F at a distance x from the fixed end, the deflection d is [48]

$$d(x) = \frac{4Fx^3}{Ewt^3}, \quad (2.2)$$

where E is the Young's modulus of the material. Strictly speaking, this model is only valid up to the end of the bridge. For a cubic material such as silicon, E may be taken as a scalar if all stresses are in the same crystal direction, as they are in the simple beam bending model. Because both of the MEMS sensor axes are oriented along $\langle 110 \rangle$ directions, the scalar Young's modulus is $E_x = E_y = 169 \text{ GPa}$ [47]. The bending stiffness of the cantilever $k_b = F/d$ is then

$$k_b(x) = \frac{Ew_bt^3}{4x^3}. \quad (2.3)$$

where w_b is the width of the bridge.

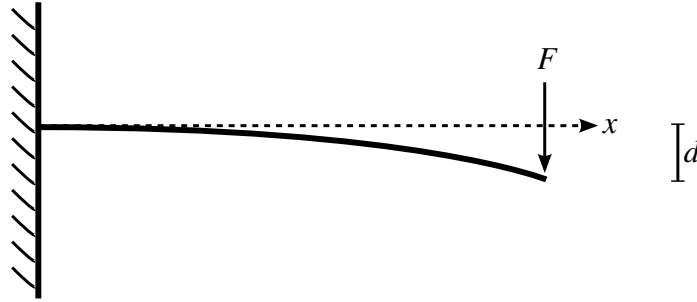


Figure 2.2: A simple model of the sensor's bending mode. The bridge is a flexible cantilever beam fixed on one end and free on the other end.

2.1.2 The rocking mode

To model the rocking stiffness, the bridge is treated as a rigid beam mounted on a pair of torsion springs (the legs) with rectangular cross section (Figure 2.3). The angular deflection of a pair of torsion springs acting in parallel is [48]

$$\phi = \frac{1}{2} \frac{\tau l}{GJ},$$

where τ is the torque applied, l is the length of each spring, G is the shear modulus of the material, and J is the torsion constant, a function of the cross-sectional dimensions of each spring with dimensions of length raised to the fourth power [48].

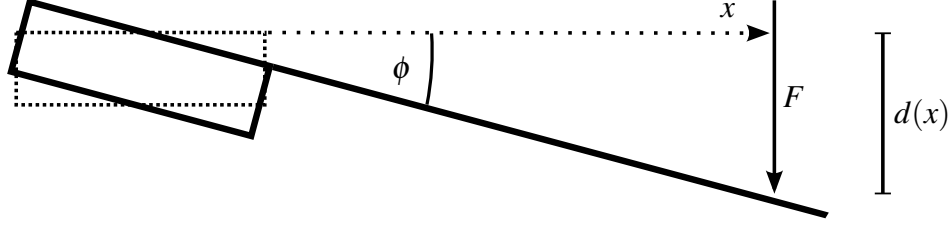


Figure 2.3: A simple model of the sensor's rocking mode. The legs twist while the bridge remains rigid.

The torsional stiffness for the rocking mode is

$$\kappa_r = \frac{\tau}{\phi} = \frac{2GJ}{l}. \quad (2.4)$$

The torsional stiffness is necessary to estimate the resonant frequency. However, the nanoin-denter measures linear stiffness, which depends on the position of the force. If a transverse load F is applied to the bridge at a distance x from the spring, the torque about the rotation axis is $\tau = Fx$. For a small twisting angle ϕ , the displacement of the cantilever at x is

$$d(x) = \phi x = \frac{Flx^2}{2GJ}.$$

Then the linear rocking stiffness $k_r = F/d$ is

$$k_r(x) = \frac{2GJ}{lx^2}. \quad (2.5)$$

For a rectangular torsion spring of cross-sectional width w_l and thickness t with $w_l \geq t$, the torsion constant J is [48]

$$J = w_l t^3 \left[\frac{1}{3} - 0.21 \frac{t}{w_l} \left(1 - \frac{t^4}{12w_l^4} \right) \right].$$

As with the Young's modulus, the shear modulus G may be treated as a scalar in a silicon crystal with the shear stresses about $\langle 110 \rangle$ directions. In this case $G = 50.9$ GPa [47].

It is clear from Equations 2.3 and 2.5 that both bending and rocking stiffnesses diverge at the center of the bridge, where x becomes small. Clearly the actual stiffness of the sensor cannot be infinite at $x = 0$. If measurements there are to be analyzed, a third stiffness term must be considered.

2.1.3 The flexing mode

The flexing stiffness k_f originates from flexing of the sensor's legs and bridge in the out-of-plane direction, and is not straightforward to compute analytically with a high degree of accuracy due to the relatively complex geometry of the sensor. However, an order-of-magnitude estimate is still useful. To that end are presented two rough but simple analytical models.

In the first model, the bridge is treated as rigid so that bending occurs only in the legs. In this model, the legs are a pair of fixed-guided cantilever beams acting in parallel, connected by a rigid beam. The corresponding spring constant is given by [48]

$$k_f = \frac{2Ew_l t^3}{l^3}, \quad (2.6)$$

where l , w_l , and t are the leg dimensions. Clearly, since the bridge is not in fact rigid, this model overestimates k_f .

Alternatively, the leg-bridge-leg system may be treated as one long narrow beam of constant width, fixed at both ends. This approach is also rough since the width of the “beam” actually increases greatly at the bridge. Assuming a single beam of length $2l + w_b$, the corresponding spring constant is [48]

$$k_f = \frac{16Ew_l t^3}{(2l + w_b)^3}. \quad (2.7)$$

Because the leg width is used, this model underestimates the stiffness.

To evaluate these two models, they are compared with the finite-element model (FEM), which will be described in more detail at the end of this section. For purposes of comparison, the deflection for each model is plotted as a function of position along the leg-bridge-leg system in response to a downward point load of 60 μN at the bridge center. In each case, the deflection is easily computed by solving the beam equation [48] $d^2z/dy^2 = -M/EI$ with appropriate boundary conditions, where z is the deflection, y is the position along the leg-bridge-leg system, and M is the bending moment. Figure 2.4 shows $z(y)$ for both of the analytical models and the FEM through the legs and bridge. As expected, neither analytical model is accurate. However, between the two of them, upper and lower bounds can be set on the flexing stiffness. Since the rigid-bridge model must overestimate the stiffness, and the long-beam model must underestimate it, it is certain that the actual flexing stiffness will lie somewhere between. As Figure 2.4 shows, the FEM bears this out. As will be shown below, the FEM provides the best estimate of

the actual flexing stiffness. However, to continue with the analytical model, it is necessary to choose either the rigid-bridge or the long-beam model. In fact, the long-beam stiffness is much closer to the FEM stiffness, and thus likely to be more accurate. Moreover, it conforms much more closely to the bending shape of the FEM than does the rigid-bridge model, as illustrated in Figure 2.4. For those reasons, the long-beam model is used from here on.

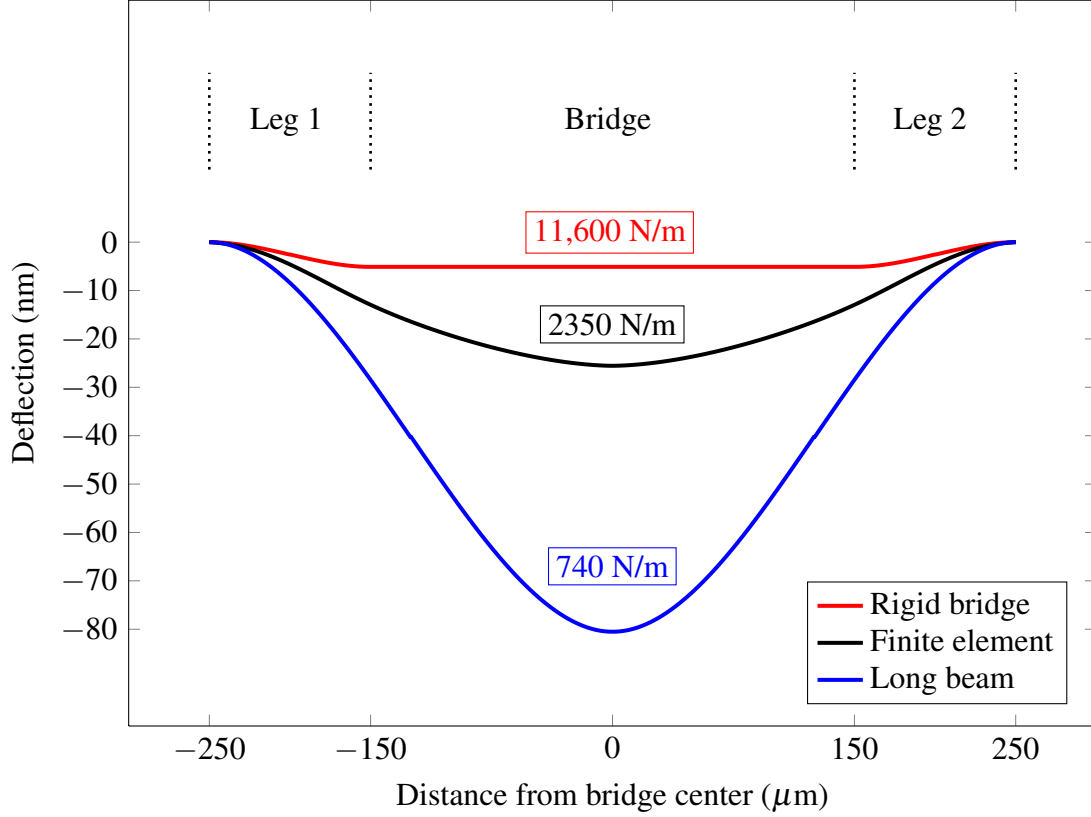


Figure 2.4: Comparison of the two analytical flexing models with the finite element model (FEM). The vertical scale is exaggerated. In each case, a 60 μN point load is applied at the bridge center, and the modeled flexing stiffness is the load divided by the absolute deflection.

With all three stiffness modes accounted for, Equation 2.1 becomes

$$\begin{aligned} \frac{1}{k(x)} &= \frac{1}{k_b} + \frac{1}{k_r} + \frac{1}{k_f} \\ &= \frac{4x^3}{Ew_bt^3} + \frac{lx^2}{2GJ} + \frac{(2l + w_b)^3}{16Ew_lt^3}. \end{aligned} \quad (2.8)$$

Once the numerical values for the various parameters (listed in Table 2.1) are inserted, the analytical model is complete. Figure 2.5 shows the relative contributions of each mode to the

overall stiffness along the x axis. Note that the overall stiffness is dominated by the smallest individual stiffness term based on Eq. (2.8), and also that the contribution from each mode becomes vanishingly small in the region where its model breaks down, i.e. close to $x = 0$ for the rocking and bending modes, and at large x for the flexing mode.

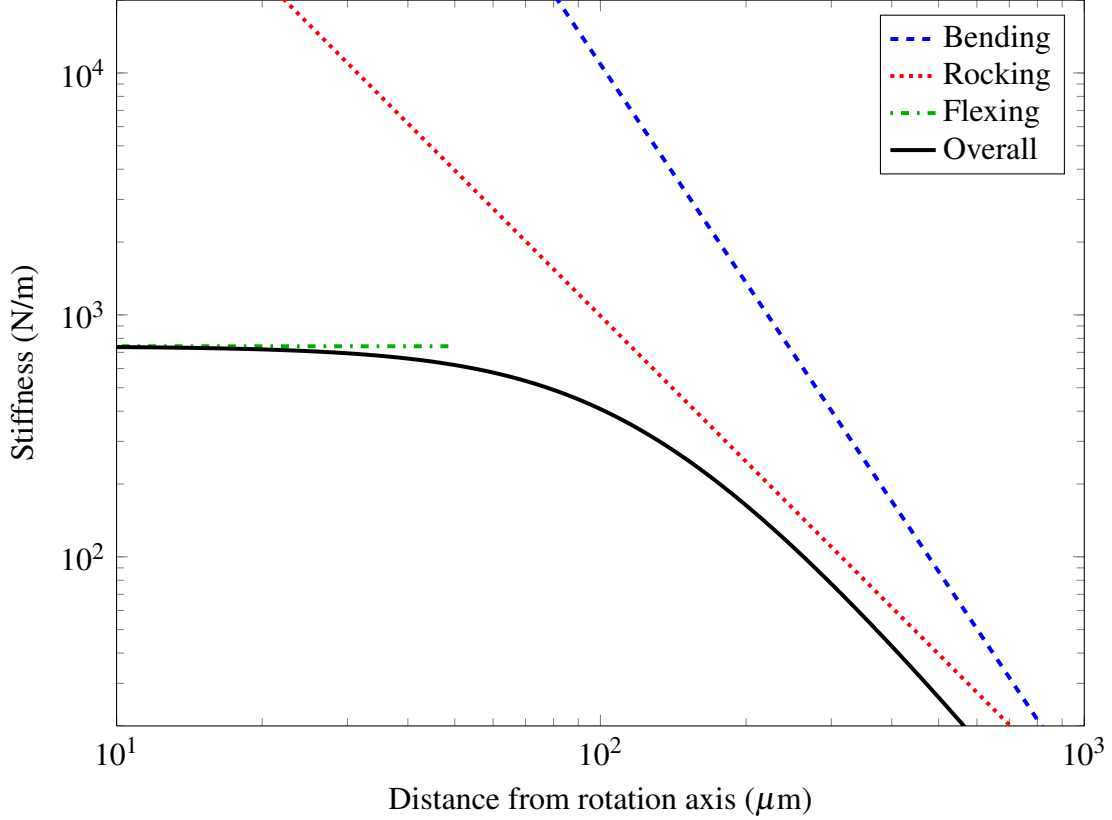


Figure 2.5: A logarithmic plot of the modeled stiffness components and the overall stiffness in the analytical model of the MEMS sensor. At any given position on the sensor, the overall stiffness is governed by the smallest of the individual terms.

2.1.4 Estimating resonant frequencies

From the individual modeled stiffness terms, it is possible to estimate the resonant frequencies of the corresponding modes. The resonant frequency f_r of the rocking mode can be estimated using

$$f_r = \frac{1}{2\pi} \sqrt{\frac{\kappa_r}{I_r}} \quad (2.9)$$

where κ_r is the torsional stiffness from Equation 2.4 and $I_r = \int_V \rho r^2 dV$ is the rotational moment of inertia of both wings rotating together, which for this sensor is $7.84 \times 10^{-14} \text{ kg m}^2$ including

the contribution from the comb fingers. Using the values from Table 2.1, the rocking frequency is estimated to be 1.79 kHz.

A similar method can be used to estimate the resonant bending frequency

$$f_b = \frac{1}{2\pi} \sqrt{\frac{\kappa_b}{I_b}}, \quad (2.10)$$

where I_b is the moment of inertia of a single wing and is equal to $I_r/2$. The torsional bending stiffness κ_b can be estimated using Equation 2.3 if the location of the force is known. Since the sensor is driven by sound pressure, the force is located at the center of mass x_{CM} of the wing-bridge combination. The torsional stiffness is then

$$\kappa_b = k_b(x_{CM})x_{CM}^2 = \frac{Ew_bt^3}{4x_{CM}}. \quad (2.11)$$

This model must underestimate κ_b because in reality the wing is wider and therefore stiffer than the bridge. As with the flexing stiffness, an alternative would be to treat the wing as rigid; however, that treatment is much more complex and not necessarily more accurate since the wing is not in fact completely rigid. Using the model described here, the estimated bending frequency is 2.83 kHz.

2.1.5 Simulations

To supplement the analytical model, a finite element model (FEM) of the MEMS sensor was created using COMSOL Multiphysics simulation software (the model is described in more detail in Appendix B). The directional Young's modulus, shear modulus, and Poisson's ratio were entered using the $\langle 110 \rangle$ constants for silicon [47]. To simplify the model geometry, each comb finger capacitor bank was modeled as a solid piece of reduced-density silicon. This simplification greatly reduced the complexity of the model without altering the rotational moment of inertia.

Even though the nanoindenter tip is much less than one micron in diameter, it may be modeled as a much larger circle. It has been shown [49] that the stresses in a thin plate caused by a load distributed over a small radius r_0 are similar to those that would obtain if the force were distributed over a larger radius $r'_0 = \sqrt{1.6r_0^2 + t^2} - 0.675t$, where t is the thickness of the plate. In this case, $r_0 \ll t$ and we may use $r'_0 = 0.325t \approx 3 \mu\text{m}$. Using the larger value for the tip size enabled coarser meshing without sacrificing accuracy.

A series of simulations were run over different nanoindenter tip locations along the lateral (x) axis of the sensor. For each location, a vertically downward boundary load was applied at the location of the tip, and the composite stiffness $k(x)$ was recorded as the load divided by the displacement. The FEM predicted a stiffness of 2.35 kN/m at $x = 0$, which differs from the two analytical models by factors of three and five respectively as discussed earlier (see Fig. 2.4). However, this study is most concerned with the stiffness at larger x , where the contributions from the rocking and bending modes dominate. At $x = 300\text{ }\mu\text{m}$, the analytical model differs from the FEM by 8%, and the models continue to converge with increasing x .

In addition to the stiffness study, the FEM was used to predict the eigenfrequencies of the sensor's vibrational modes, obtaining 1.53 kHz for the rocking mode and 2.91 kHz for the bending mode. These values are within 15% and 3%, respectively, of the analytical estimates. The discrepancies can be partly attributed to the use of isotropic moduli of silicon in the analytical models.

2.2 Nanoindenter measurements

Stiffness measurements were made using an Agilent G200 nanoindenter with the Dynamic Control Module (DCM) head [50] and a diamond Berkovich tip with a radius specification of $\leq 20\text{ nm}$ across. This tip was readily available, but any other tip could be expected to work equally well for a study of MEMS surfaces in which the tip does not appreciably indent the material. The G200 provides a motorized stage that positions the test sample under the tip to an accuracy of $1\text{ }\mu\text{m}$ in each direction. Nanoindenter tip displacements can be measured to a precision of less than 0.01 nm , but may be as large as $500\text{ }\mu\text{m}$, and available loads range from 50 nN to 500 mN . A schematic of the nanoindenter is shown in Fig. 2.6.

There were several instrumentation parameters for this study. Because the composite stiffness of the MEMS sensor ranged from over 2000 N/m at the center to just a few N/m near the wingtips, one of the primary considerations was the sensitivity of the nanoindenter to surface contact. The G200's "surface detection stiffness criteria" parameter allows the user to determine the surface stiffness that will trigger the instrument's surface detection routine. Repeated trials with various choices of this parameter confirmed that the lowest surface stiffness that was reliably detected by the instrument was about 20 N/m . Based on this limitation, the study was restricted to the parts of the MEMS sensor where the modeled composite stiffness was higher than 25 N/m , corresponding to values of x less than $500\text{ }\mu\text{m}$.

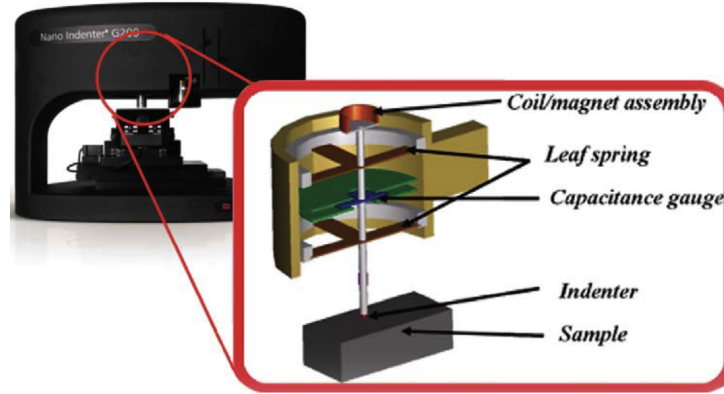
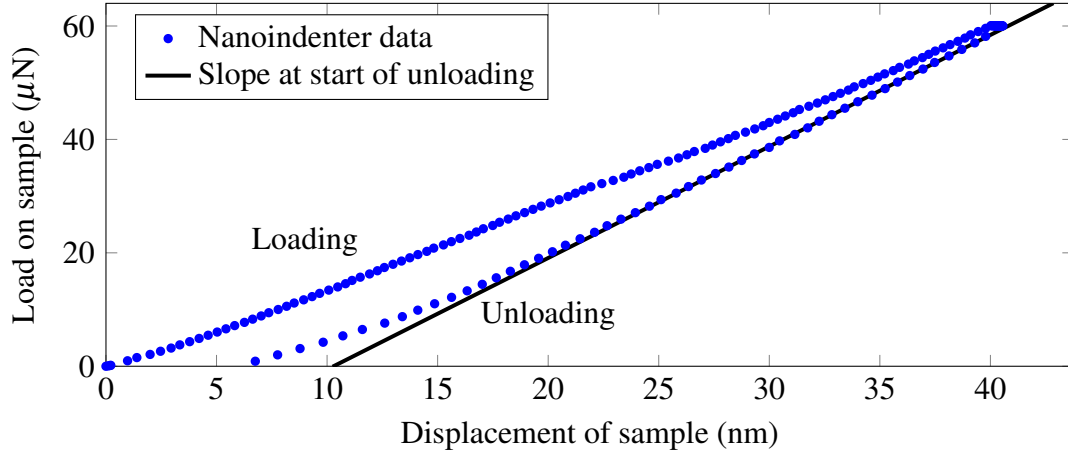


Figure 2.6: A schematic of the Agilent G200 nanoindenter, from the user manual.

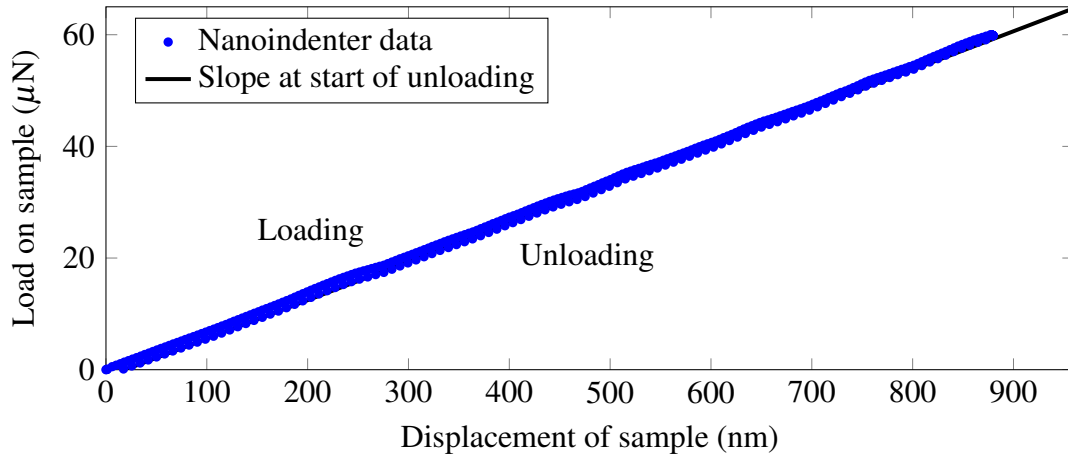
Another key testing parameter was the maximum load applied during each test. Higher loads produced somewhat cleaner data, but also greater deflection of the MEMS surface. Since excessive deflection would lead to the MEMS surface contacting the substrate below and could induce a nonlinear stiffness response, the maximum load was chosen to result in a deflection less than the thickness of the silicon layer ($9.5\text{ }\mu\text{m}$) at the sensor's wingtip. Based on the analytical and finite element models, this maximum was determined to be about $85\text{ }\mu\text{N}$ at $x = 500\text{ }\mu\text{m}$. Ultimately, a conservative yet productive maximum load of $60\text{ }\mu\text{N}$ was chosen for each test. Measured vertical displacement of the sensor surface ranged from 30 nm with the load applied at the center of the bridge to over 600 nm with the load applied beyond the end of the bridge.

Because in normal operation the deformation of the MEMS sensor is purely elastic, the quantity of interest is the elastic stiffness. In a typical nanoindentation test, the loading curve is nonlinear due to combined plastic and elastic deformation. On unloading, however, the deformation is purely elastic and thus the linear elastic stiffness is simply the slope of this curve just after unloading begins. When the curve does not have a well-defined slope, a power law fit can produce more precise measurements of elastic stiffness [51], but for this MEMS study the curve is linear enough to use a linear fit. Figure 2.7 shows two tests taken at different positions on the sensor. Figure 2.7a shows a test taken at the stiffest point, i.e. $x = 0$. Even though plastic deformation leads to visible nonlinearity, there is still a clear linear region on unloading, and thus a well-defined linear elastic stiffness. In the vast majority of tests, the elastic stiffness is even better defined. In most cases, the plastic deformation is dwarfed by the elastic deformation as shown in Figure 2.7b. In this example, where $x = 325\text{ }\mu\text{m}$, the loading and unloading portions of the curve are nearly overlapped, with their slopes differing by only 1%. This linear elastic

response is critical to this research because the analysis depends on a well-defined stiffness at each point.



(a)



(b)

Figure 2.7: Sample nanoindenter tests conducted at different points on the MEMS sensor illustrate the linear elastic response. The elastic stiffness is the slope of a line fit to the data just after unloading begins. (a) $x = 0$, the stiffest part of the MEMS sensor. (b) $x = 325 \mu\text{m}$, a more typical test.

2.2.1 Stiffness measurements

To establish the stiffness as a function of position on the sensor, tests were conducted at intervals of $5 \mu\text{m}$ along the x -axis and the elastic stiffness was computed for each test. Figure 2.8 shows the results plotted as a function of distance from the rotation axis, along with the results from the analytical model and FEM. At $x = 0$, the numerical model is clearly superior to the analytical

model. The discrepancy between measurement and FEM is 12% at that point, whereas the analytical model underestimates the stiffness by a factor of three. At larger x , the measurements validate both models. At $x = 500 \mu\text{m}$, the analytical model differs from measurements by 9% and the FEM by 6%. The nanoindenter measurements definitively show where each model is valid.

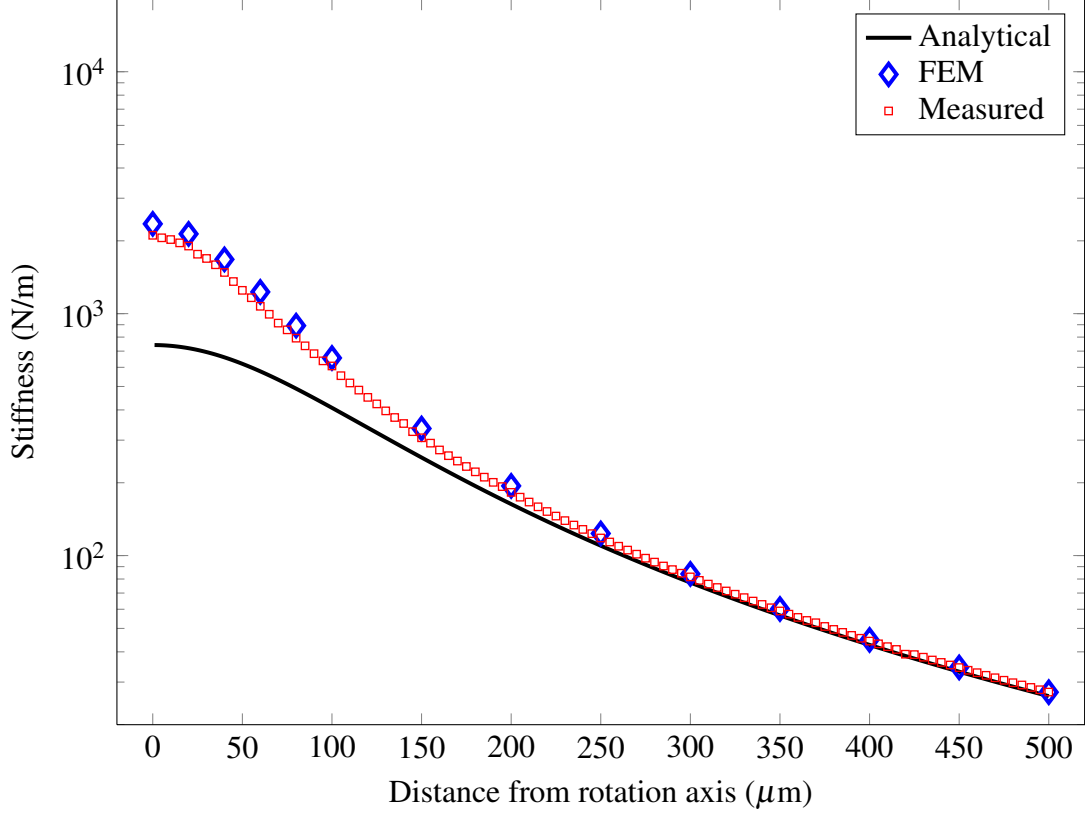


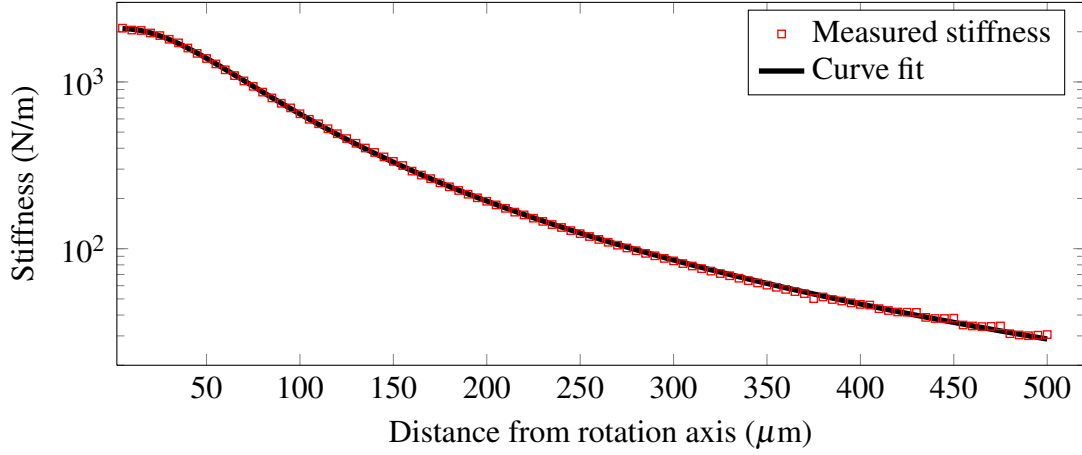
Figure 2.8: Comparison between the analytical model, the finite element model, and the nanoindenter results.

To evaluate the individual stiffness components $k_r(x)$ and $k_b(x)$, a curve was fit to the measured data using Matlab with the Ezyfit open-source fitting tool. The curve fit was based on the analytical expression in Equation 2.8 and given by

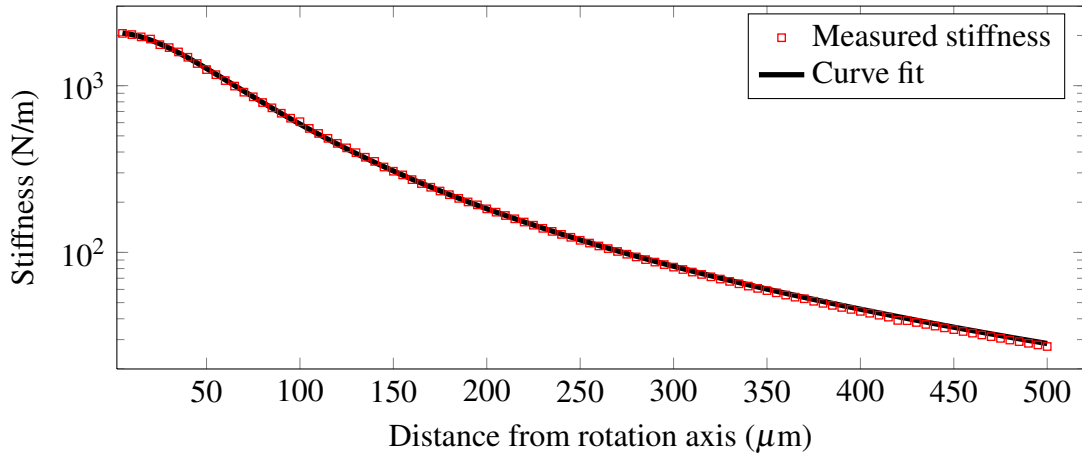
$$\frac{1}{k(x)} = \frac{(x-x_0)^3}{a_3} + \frac{(x-x_0)^2}{a_2} + \frac{1}{a_1}, \quad (2.12)$$

where a_1 , a_2 , and a_3 are parameters and an x offset is included to account for any systematic error in the coordinates of the stiffness tests. The curve in Equation 2.12 was fit to two separate data sets, one from the left side of the MEMS sensor and the other from the right side, as shown

in Figure 2.9. Table 2.2 lists the values for the parameters and the correlation coefficients R for both fits. From the curve fit parameters, it is possible to estimate the resonant frequencies of the rocking and bending modes. By matching the fit parameters to the corresponding values in the analytical model, it is straightforward to estimate the torsional stiffness for each mode and thence the resonant frequencies.



(a)



(b)

Figure 2.9: Equation 2.12 fit to the nanoindenter measurements: (a) left side of sensor; (b) right side. In both cases the correlation coefficient R is greater than 0.9999 using the fit parameters listed in Table 2.2.

The resonant frequencies estimated from the measured stiffness are listed in Table 2.3 along with the estimates obtained from the analytical and finite element models. Also listed for comparison are the resonant frequencies of an identical sound sensor as measured by a laser vibrom-

eter with the sensor excited by an external sound source. The sensor used in the nanoindenter study could not be removed intact from the mount for laser vibrometer testing. Because there is variation in resonant frequencies even between ostensibly identical sensors, the vibrometer results should be viewed as another estimate rather than an exact measurement.

Table 2.2: Parameters for the curves fit to the data from the left and right sides of the MEMS sensor. Values are in SI units except x_0 .

Fit parameter	Left side fit	Right side fit
a_1 ($= k_f$)	2.09×10^3	2.10×10^3
a_2 ($= 2GJ/l$)	9.05×10^{-6}	8.95×10^{-6}
a_3 ($= Ew_b t^3/4$)	1.72×10^{-8}	1.94×10^{-8}
x_0	$3.64 \mu\text{m}$	$-2.25 \mu\text{m}$
R	0.99994	0.99997

Table 2.3: Resonant frequencies from the analytical model, from the FEM, estimated from the measured stiffness, and directly measured using a laser vibrometer.

	Rocking frequency (kHz)	Bending frequency (kHz)
Analytical model	1.79	2.83
FEM	1.53	2.91
Estimated from stiffness	1.71	3.67
Vibrometer	1.41	2.80

The discrepancy between modeled, estimated, and measured values is greater for the bending mode frequency, which is to be expected since the measurements were taken in regions where the bending mode makes only a small contribution to the overall stiffness (as mentioned earlier, measurements were restricted to locations where the composite stiffness was above 25 N/m and was dominated by the rocking mode). Nevertheless, the estimates are close enough to suggest that the nanoindenter method is a valid means of estimating the resonant frequencies of a MEMS device. Also, it must be emphasized that the vibrometer measurements alone cannot distinguish the frequencies by their sources. The only way to associate each frequency with the corresponding physical structures is through modeling.

2.2.2 High load testing

The final test conducted with the nanoindenter was designed to estimate the maximum sound pressure level the sensor can tolerate without fracturing. For this measurement, the nanoindenter's DCM head was replaced by the XP head to allow for loads up to 500 mN [50]. The load was applied at the center of one of the sensor's wings, and was set to an arbitrary high value in the expectation that the sensor would fracture during the loading process. This fracture would be indicated by the load suddenly dropping to zero as the displacement continued to increase. However, the expected fracture did not occur. Instead, as the load was increased, the displacement eventually stopped increasing, as shown in Figure 2.10. The maximum load attained was 4.5 mN, and the ultimate displacement was about 32 μm . The halt in displacement suggests that the sensor had made contact with the side walls of the trench beneath.

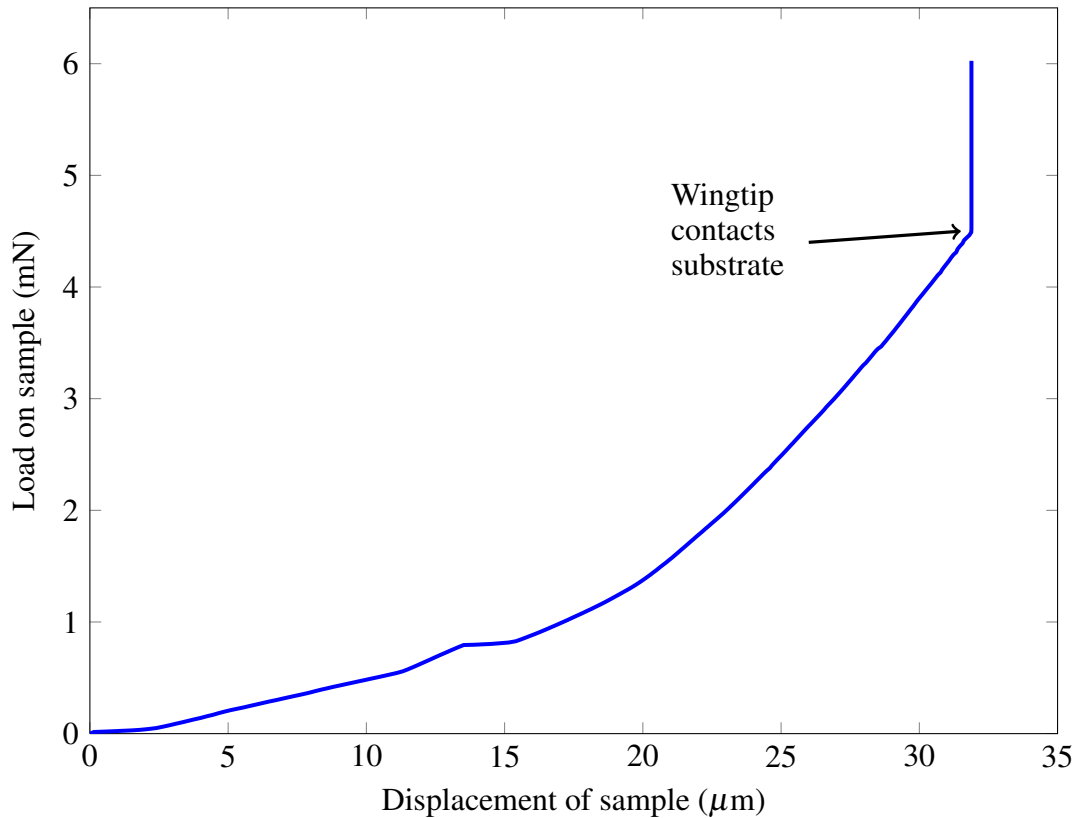


Figure 2.10: Failure testing of the MEMS sensor. Loads are two orders of magnitude higher than in the stiffness testing, and the response here is clearly nonlinear (compare to Figure 2.7). At about 32 μm , the load spikes, suggesting that the sensor has made contact with the substrate below.

The sensor remained intact, and subsequent inspection with an optical microscope showed no

visible damage. Moreover, repeated similar measurements showed identical results, suggesting that the sensor was not permanently affected by the test loads. Unfortunately, it was not possible to remove the sensor intact from the nanoindenter mount in order to directly test its acoustic response after the failure testing.

Even though the exact fracture load was not established, these results show that the sensor can withstand a sound pressure level (SPL) at least equivalent to the nanoindenter test load. The equivalent SPL is

$$SPL = 20 \log \left(\frac{P_{\text{equiv}}}{P_{\text{ref}}} \right) \quad (2.13)$$

where P_{equiv} is the equivalent acoustic pressure amplitude and P_{ref} is the standard reference pressure of 20 μPa . The acoustic pressure equivalent to the test load can be estimated as the load divided by the wing area, in this case about 2400 Pa (note that this is several orders of magnitude less than the yield strength of crystal silicon, 7 GPa [52]). The resulting SPL of about 162 dB suggests that the MEMS sensor can tolerate extremely high sound levels. Also, it is important to note that the actual failure load for the sensor must be higher than the test load used in the calculation. Thus the failure SPL for the sensor is higher than 162 dB. The nanoindenter technique provides a means of simulating high sound pressures not practical to generate in the laboratory.

Because the nanoindenter load is static, it does not perfectly simulate the dynamic stresses from actual acoustic pressure. Nevertheless, this technique can be used to estimate the sensor's maximum tolerated sound pressure level.

2.3 Conclusions

The nanoindenter is a useful tool for investigating basic properties of simple MEMS structures. Here a nanoindenter has been used to analyze several characteristics of a MEMS device with multiple coupled flexible components. First, direct measurement of the stiffness can confirm an overall linear response (i.e. Hooke's law) over the range of loads likely to be experienced by the sensor during operation. Second, by measuring the local stiffness at various points across the device surface, it is possible to relate the structural components of the device to the corresponding resonant frequencies for each vibration mode. In both of those applications, the nanoindenter validates analytical and numerical models. Third, the nanoindenter can be used

to find the failure load of the MEMS device and thence the maximum tolerable sound pressure level. Similar studies can be useful in analyzing other MEMS with coupled mechanical components.

CHAPTER 3:

Branched comb fingers improve sensitivity to out-of-plane motion

Note: the content of this chapter, in substantially the same form, has been submitted for publication to the IEEE/ASME Journal of Microelectromechanical Systems [39].

In this chapter, fabrication of a MEMS acoustic direction-finding sensor with substantially higher sensitivity is described. The increased sensitivity is enabled by larger capacitance of the sensor when the traditional straight comb finger capacitors are replaced by a branched capacitor design. The sensitivity increase is explained using a simple analytical model as well as a finite element model that incorporates the fringe field effects. Finally, it is shown that the sensitivity could be further improved by reducing the sensor's residual stress-generated curvature to increase the overlap between comb fingers.

The sensitivity of a capacitive readout system depends on how much the capacitance changes with displacement. The size of the capacitance change in turn depends on the size of the capacitors; for a parallel-plate capacitor, $C \propto A/d$, where A is the plate area and d is the gap. In order to maximize the sensitivity of the sensor's readout system while complying with the given design rules, comb fingers have until now been made as long, narrow, and close together as possible within the SOIMUMPs design rules [36]: $2\text{ }\mu\text{m}$ wide and $100\text{ }\mu\text{m}$ long, with a $2\text{ }\mu\text{m}$ gap between them [7]. For a given wing perimeter, there is a maximum number of these fingers that will fit along the wing, and thus an upper limit on capacitance and sensitivity. In addition, experience has shown that such long comb fingers are very susceptible to breakage during handling. An example of these comb fingers was shown in Fig. 1.1, and is repeated here as Fig. 3.1.

The goal of this work was to increase the durability and size of the comb finger capacitors without violating the design rules. To solve this problem, a branched comb finger design has been developed using a larger number of shorter fingers. It is important to note that unlike the lateral comb motion used in many other MEMS designs, the acoustic DF sensor uses out-of-plane motion between comb fingers. Because the relative motion is out-of-plane, it is possible to change the comb finger shape without affecting their function. An acoustic sensor incorporating the branched design, shown in Fig. 3.2, should be more sensitive to sound than the version with straight comb fingers due to the increased input capacitance.

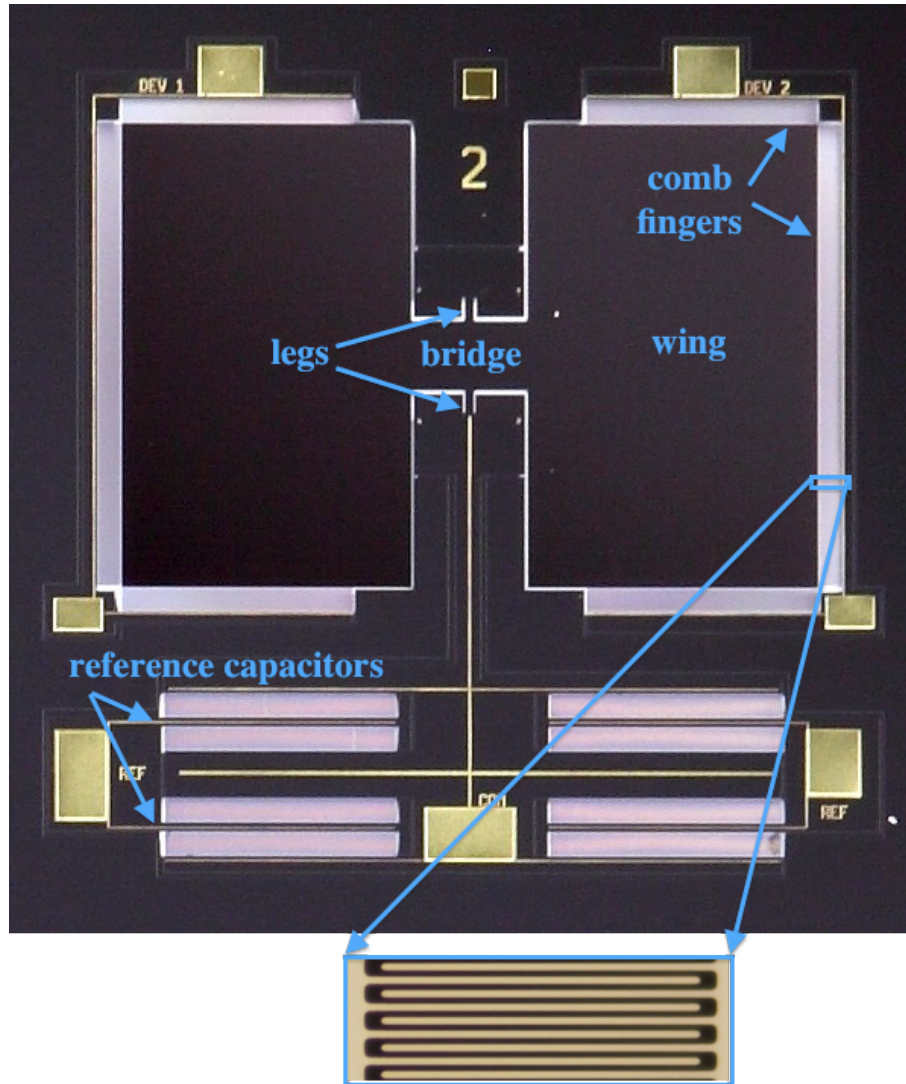


Figure 3.1: The acoustic DF sensor with straight comb fingers. Each wing has comb finger banks on three sides. The inset shows a closeup of the comb fingers.

3.1 Measurements

The crux of this experiment was to compare the electronic output of the branched-finger sensor to that of the straight-finger sensor, when both were exposed to the same acoustic signal. Although this comparison was straightforward, there were two secondary considerations that also required measurements to be made. Before comparing the electronic responses, it was necessary to establish the relative mechanical vibration responses of the two sensors. A larger mechanical response would be expected to produce a larger electronic output even if the capacitive readout system was not more sensitive. Because these sensors are designed to detect

broadband signals, the vibrational or electrical response is defined as the peak area rather than the peak height. In addition, to understand the results of the mechanical response and electronic output comparisons, it was necessary to consider the permanent bending of the two sensors' wings due to residual stress, and the effect of this bending on the comb finger capacitance.

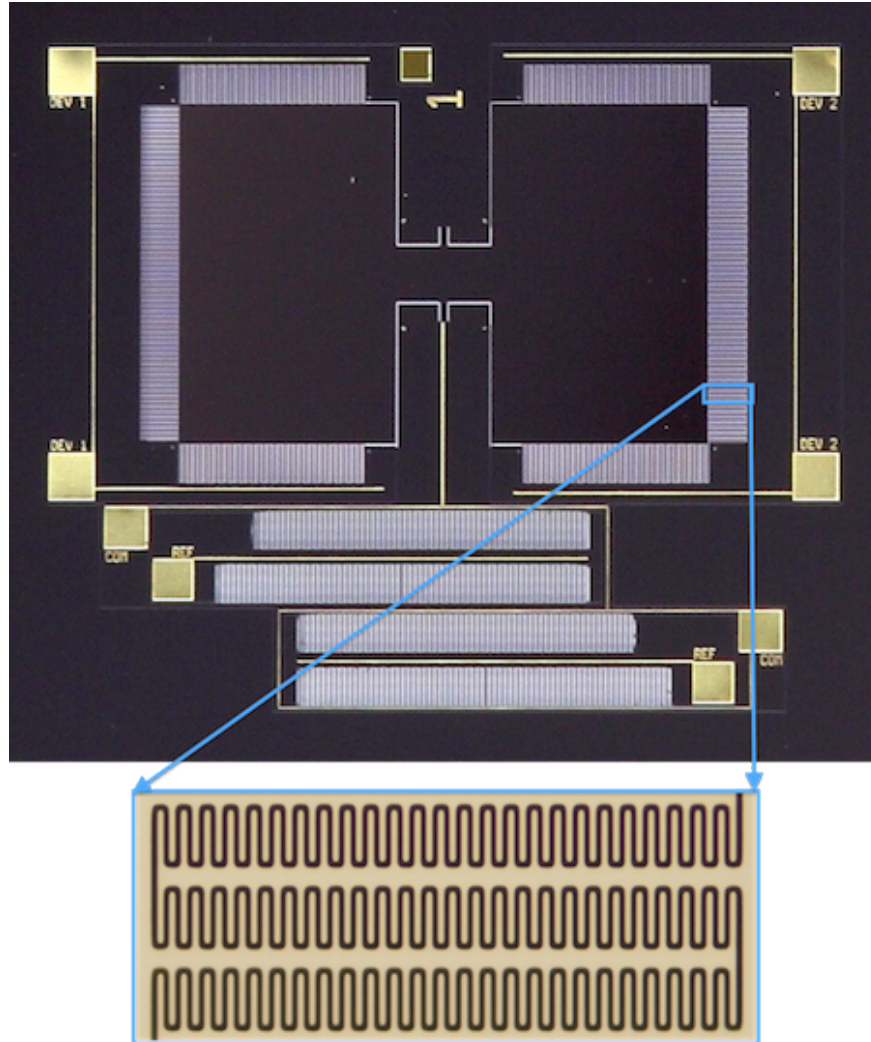


Figure 3.2: The sensor with branched comb finger design. The fingers are shorter but more numerous, and are mounted on thick spines. Including the comb fingers, the wings are the same length and width as the other sensor. The inset shows a pair of interlaced spines, each with 25 pairs of comb fingers.

3.1.1 Mechanical response comparison

The first phase of the experiment was to identify and measure the mechanical resonances for the straight-finger and branched-finger sensors. This was done by exposing each sensor to a

computer-generated sound signal that swept a wide range of frequencies. The vibration response spectra of the two sensors, shown in Fig. 3.3, were measured using a Polytec laser vibrometer aimed at one wingtip.

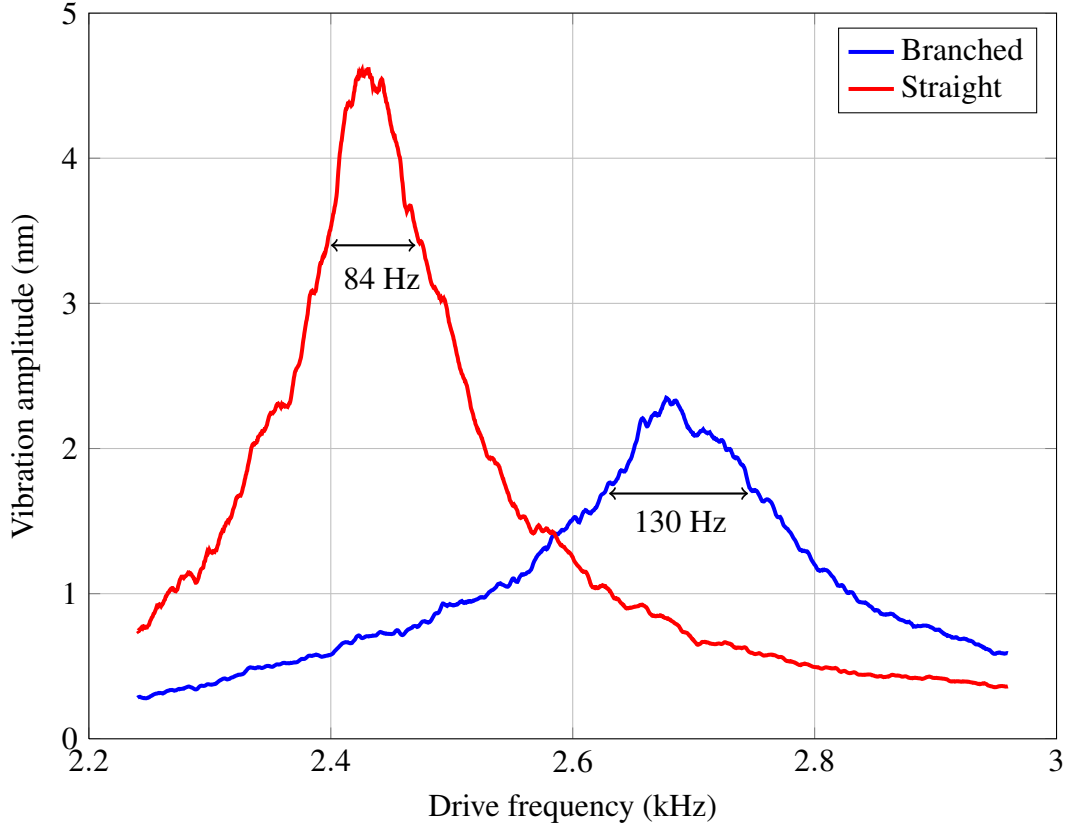


Figure 3.3: The vibration spectra (bending mode) of the two acoustic DF sensors. The sensor with branched comb fingers has a smaller, wider resonance peak at a higher frequency. Full width at half-maximum (FWHM) is shown for both sensors.

As mentioned earlier, each sensor is designed to have two normal modes (rocking and bending) and therefore two resonance peaks; however, in both cases the rocking amplitude is negligibly small compared to that of the bending and is not visible in the figure. This large difference in peak height is due to the physics of the two normal modes [1]. The bending resonance peak for the branched-finger sensor occurs at a slightly higher frequency, 2.7 kHz as opposed to 2.4 kHz for the straight-finger sensor. This is expected because the branched-finger sensor has slightly smaller mass; the wings are smaller to accommodate the larger size of the branched comb fingers. In addition, this peak has smaller amplitude and wider bandwidth than the other, meaning

that the branched-finger sensor does not respond as strongly to a pure tone at resonance, but responds to a wider range of frequencies.

The wider peak is associated with greater damping through the relationship $\gamma = \Delta\omega$ where γ is the damping coefficient and $\Delta\omega$ the full width at half-maximum (FWHM) of the peak [53]. A detailed analysis of damping is beyond the scope of this dissertation, but it is worth noting that the damping coefficient of the branched-finger sensor is 1.5 times that of the straight-finger sensor, while the perimeter of its comb finger array is 1.6 times longer. This similarity between ratios suggests that the damping coefficient may be roughly proportional to the perimeter of the comb finger capacitor.

3.1.2 Electrical signal

Having found the mechanical resonances for the two sensors, the next step was to measure their electrical output. The primary measure of success for the branched-finger sensor was whether it produced a larger electrical output than the straight-finger sensor, given the same acoustic input signal. To assess this, each sensor was exposed to a computer-generated sound signal and recorded the MS3110 output signals from both. The MS3110 delivers a voltage that varies linearly with changes in capacitance so that when the sensor wing oscillates harmonically, the output voltage follows the motion as shown in Fig. 3.4. The electronic response from each sensor was recorded by sweeping the incident sound frequency from 2.2 to 3.0 kHz. The measured electronic output spectra for the sensors are shown in Fig. 3.5.

From Fig. 3.5, it is clear that the branched-finger sensor's peak contains a much larger area than that of the straight-finger sensor (compare Fig. 3.5 to Fig. 3.3). This result shows that compared to the straight-finger sensor, the branched-finger sensor responds more strongly to a broadband sound signal due to the higher bandwidth.

3.1.3 Curvature measurement

To fully understand the mechanism for the increased electronic response, it was necessary to measure the residual stress curvature in both sensors to account for the comb finger overlap in both cases. It is obvious that the capacitance should depend on the overlapped area of the opposing surfaces of the comb fingers. What is not obvious is the fact that in these particular sensors, those opposing surfaces do not completely overlap due to curvature of the two wings

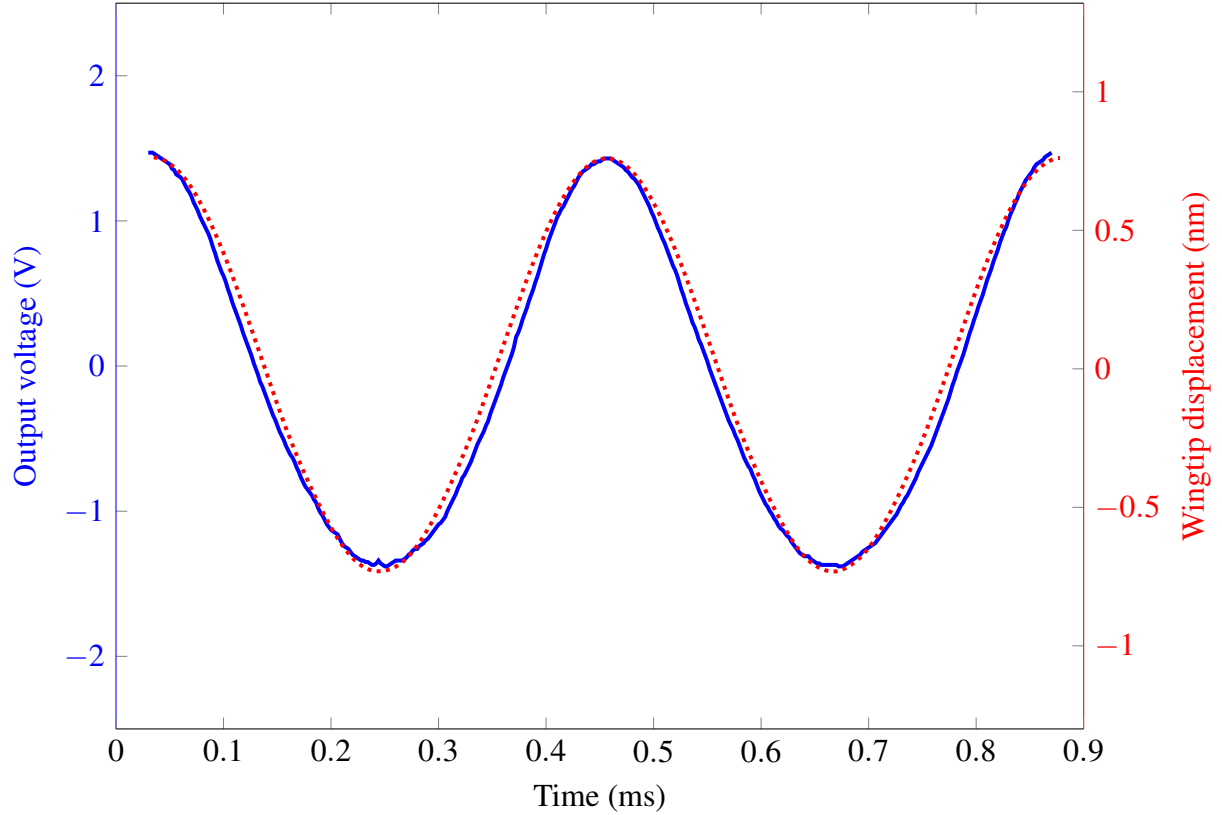


Figure 3.4: The output voltage of the electronic readout circuit during a typical measurement. The measured wingtip displacement from equilibrium is superimposed on a different scale. Both waveforms are clearly sinusoidal and have the same frequency (2.4 kHz in this case) as the acoustic drive signal. The similarity between the two waveforms confirms that the output voltage varies linearly with the wingtip displacement.

resulting from the residual stress. In fact, measurements showed that the curvature is so great that in most cases the fingers do not overlap at all, as sketched in Fig. 3.6.

To examine the effect of this curvature, the vertical offset between sensor wing and substrate was measured at regular intervals along the comb finger banks. This was done by placing each sensor under an optical microscope with a $100\times$ objective lens. At each interval, the offset was measured to the nearest micron using the difference in microscope focus settings between the wing and substrate. Finally, the average offset and standard deviation were computed for each sensor. The straight-finger sensor had an average offset of $20 \pm 5 \mu\text{m}$ and the branched-finger sensor had an average offset of $19 \pm 4 \mu\text{m}$. The range of offsets for both sensors was 10 to $27 \mu\text{m}$. These results, combined with the fact that the device layer is only $10 \mu\text{m}$ thick, show that the moving and fixed comb fingers are for the most part not overlapped at all.

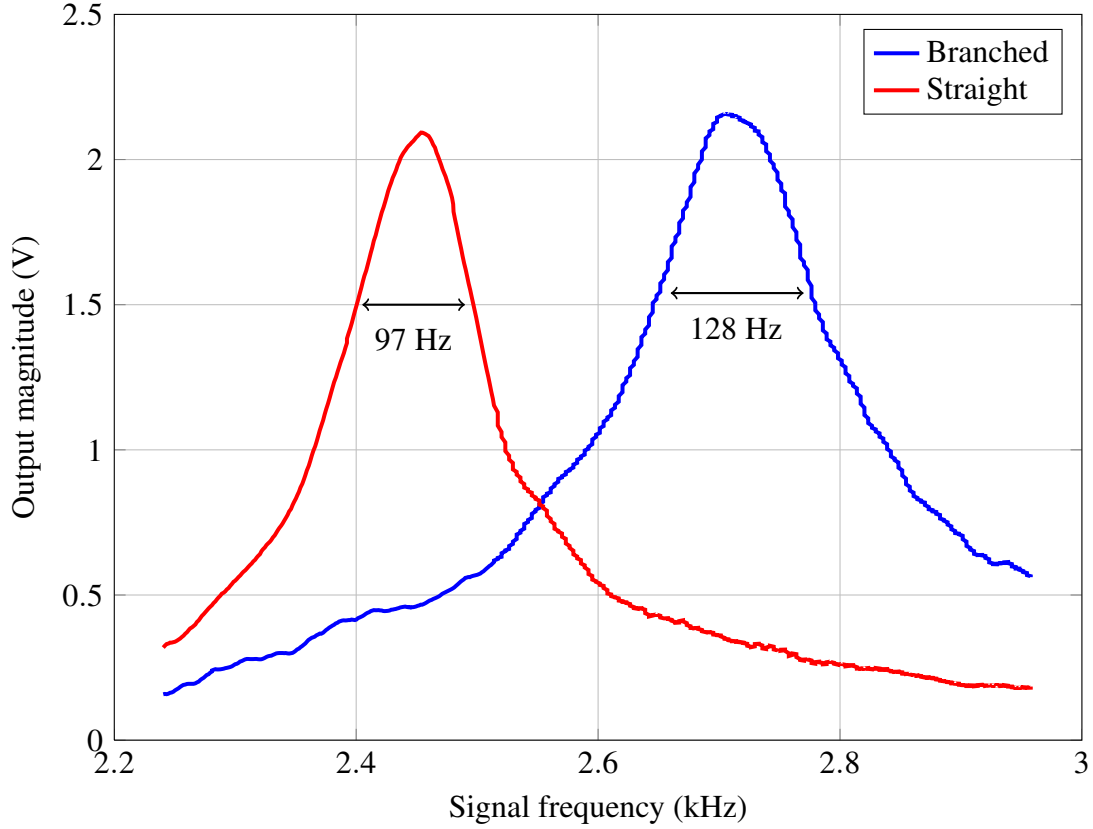


Figure 3.5: The measured electronic output spectra of the two acoustic DF sensors. Full width at half-maximum is indicated for both sensors.

It is interesting to note that the branched comb fingers do in fact appear to be more durable than the straight fingers. After all other measurements were completed, the chip carrier containing both sensors was inadvertently dropped onto a steel table from a height of approximately 25 cm. Prior inspection had shown no damage to any of the comb fingers. After the drop, many of the straight comb fingers were broken, but the branched fingers all remained intact. This result provides anecdotal evidence that the branched design is in fact more durable as intended.

In order to understand the effect of comb finger design on capacitance, taking curvature into account, both designs were analyzed and simulated as described next.

3.2 Discussion

The first assumption made in this study was that the branched capacitor design would function essentially the same as a traditional straight comb finger design, when employed to sense out-of-plane motion. This turned out to be correct, although the reason is not as straightforward as

expected. The sinusoidal waveform shown in Fig. 3.4 was seen from both sensors, demonstrating that in both cases the electronic readout circuit produced a voltage that varied linearly with sensor displacement. This observation indicates that the capacitance also varies linearly with displacement.

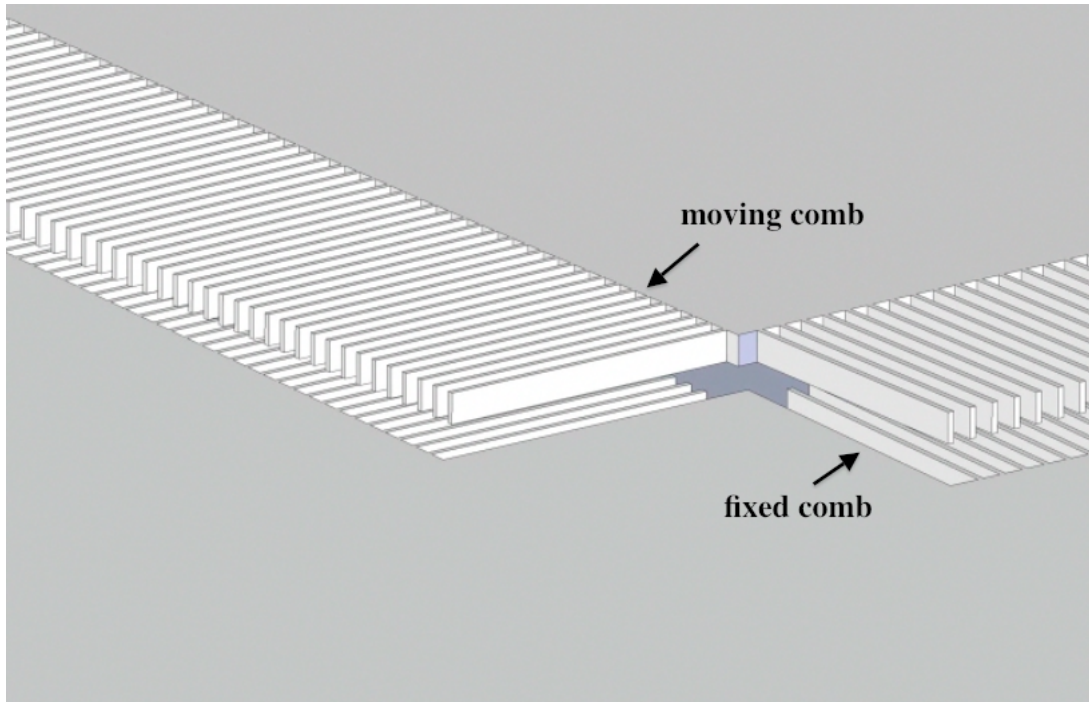


Figure 3.6: A sketch of the corner of the straight-finger sensor wing. The residual stress-generated offset between moving and fixed fingers is approximately to scale.

But it was also observed that the relative vertical offset between comb fingers is typically greater than their thickness as illustrated in Fig. 3.6. How can this fact be reconciled with the linear capacitance dependence on displacement? The hypothesis was based on the assumption that out-of-plane displacement of the moving comb fingers would change the vertical overlap between opposing capacitor “plates” and thereby alter the effective surface area of the capacitor. This was in fact the intended mechanism. But in fact this overlap is typically nonexistent. To understand why the linear relationship remained, a simple analytical model was developed of comb finger capacitance as a function of offset, when the offset is greater than the comb finger thickness. To check the accuracy of this model, a finite element model was also built. In each case the capacitance was modeled as a function of out-of-plane displacement.

3.2.1 Analytical model

For the analytical model, let z be the displacement of the moving fingers above the fixed, where the fingers have vertical thickness t equal to the thickness of the silicon device layer, and $z > t$ as depicted in Fig. 3.7. The moving and fixed fingers can be represented as the two plates of a single large parallel-plate capacitor separated by a gap $z - t$. The surface area is taken to be the area of the horizontal silicon surface of each plate (excluding the air gaps between fingers). This area is just the product of the finger width w and the combined length l of all fingers in the bank.

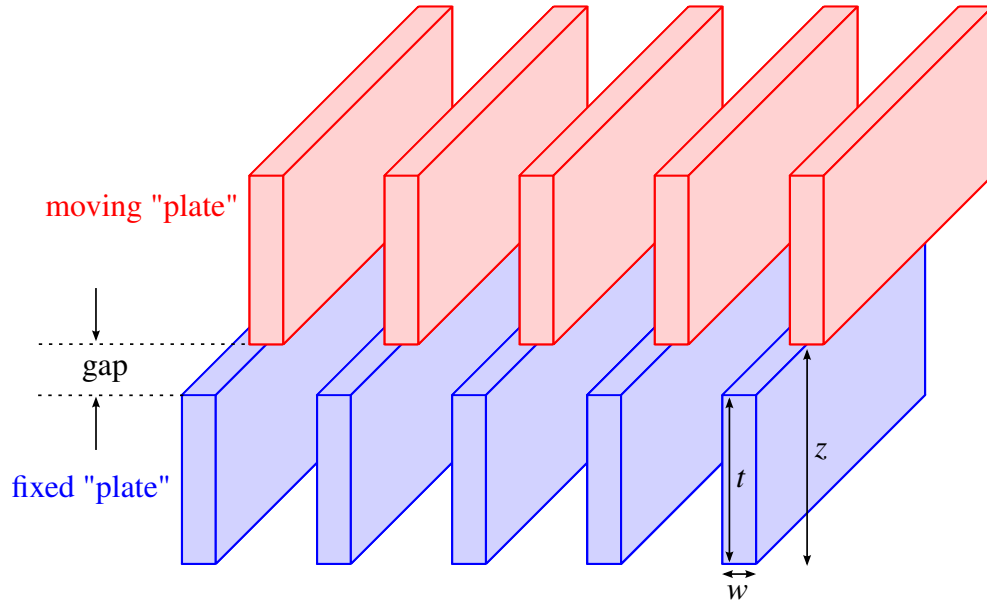


Figure 3.7: The two-plate model of non-overlapped comb fingers. The vertical offset between moving and fixed fingers is z and the capacitor gap between the two “plates” is $z - t$. This model applies to straight and branched comb fingers where $z > t$.

The capacitance of these virtual parallel plates is approximately

$$C(z) = \frac{\epsilon_0 w l}{z - t} \quad (3.1)$$

where $\epsilon_0 = 8.85 \times 10^{-12}$ F/m is the permittivity of free space. The capacitance in Eq. (3.1) is evidently not linear in the displacement z . However, over a sufficiently small range Δz , the capacitance change ΔC will be approximately linear. This condition is met in our measurements because Δz is on the order of nanometers, whereas $z - t$ is typically on the order of microns.

The change in capacitance with displacement is obtained by differentiating Eq. (3.1) as

$$|\Delta C| = \frac{\epsilon_0 w l}{(z - t)^2} |\Delta z|, \quad (3.2)$$

where $z - t$ is approximately constant over the range Δz . Thus the observed change in output voltage (see Fig. 3.4), which varies linearly with ΔC according to the readout circuit design, also varies linearly with Δz .

3.2.2 Numerical model

To validate the two-plate approximation, a two-dimensional finite-element model was created using COMSOL Multiphysics (for details, see Appendix B). The FEM simulated the vertical cross-section of a bank of capacitor fingers at variable relative offset z . In this model z was allowed to be greater or less than the device layer thickness t . During the simulation a positive voltage is applied to the moving fingers and negative voltage to the fixed; the software computes the resulting electric potential within the simulation volume. Two sample plots of the electric potential for different values of z are shown in Fig. 3.8.

The roughly flat shapes of the equipotential lines in Fig. 3.8 validate the key assumption of the two-plate model, namely that the moving and fixed banks can be approximated as thin charged plates. The flatter the equipotential lines, the closer the analytical model should agree with the FEM. Simulations for larger values of z produced less waviness, as seen in Fig. 3.8b compared to Fig. 3.8a. Thus it is expected that the models will agree best when z is large. Conversely, as z decreases toward t , the fingers begin to overlap and the two-plate model breaks down.

To compare the two-plate model with the FEM, the predicted capacitance per unit length $c(z)$ was examined in each case. From the two-plate model, this is obtained by dividing Eq. (3.1) by the combined finger length l :

$$c(z) = \frac{\epsilon_0 w}{z - t} \quad (3.3)$$

where w is the finger width. From the FEM, the capacitance per unit length is derived from the electrical energy stored in the capacitor using $u = c(\Delta V)^2/2$, where u is the energy per unit length and ΔV is the applied voltage difference. Finally, the z -dependence of c is found by repeating the simulation for different values of z . To compare the two models, their respective values for $c(z)$ were plotted together as in Fig. 3.9. Also plotted for reference is the capacitance

per unit length for $z < t$ as estimated using vertical overlap of the combs:

$$c(z) = \frac{\epsilon_0(t-z)}{d}, \quad (3.4)$$

where d is the gap between opposing fingers, $2\text{ }\mu\text{m}$ in this case.

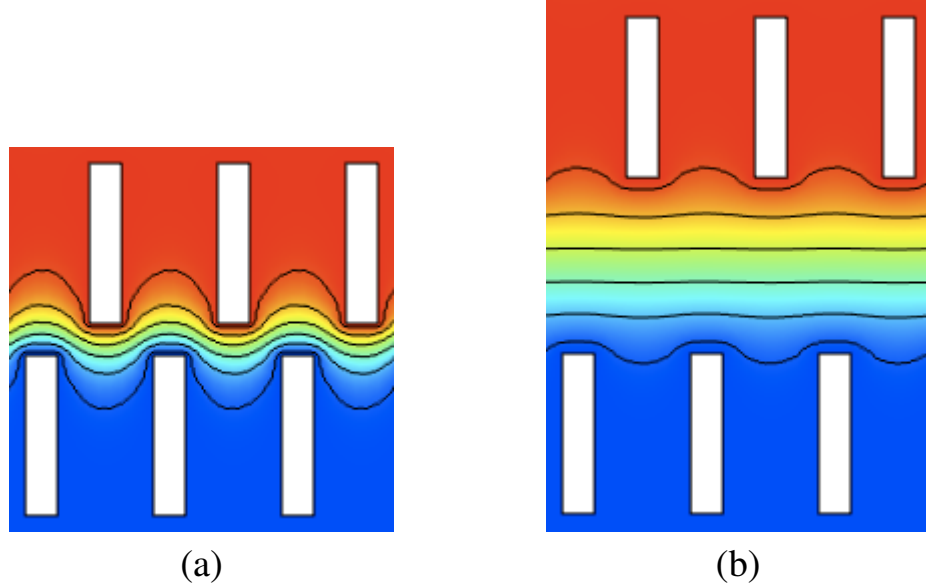


Figure 3.8: A 2D finite-element model of a comb finger bank cross-section, comb fingers shown in white. Electric potential is indicated by the color spectrum and equipotentials are shown in black. The offset z in (a) is $12\text{ }\mu\text{m}$, and in (b) is $21\text{ }\mu\text{m}$. With greater offset, the equipotentials are straighter, indicating better agreement with the two-plate model of Fig. 3.7 and Eq. (3.3).

The FEM suggests that Eq. (3.4) underestimates the actual capacitance for $z < t$. This is expected because fringing effects are neglected. However, except for z very close to zero, the fringe field appears to add a more or less constant capacitance until z approaches t , at which point the elementary model breaks down. As z increases beyond t , the two-plate model of Eq. (3.3) becomes valid. In fact, the larger z , the closer Eq. (3.3) agrees with the FEM, as expected. Taken together, these observations suggest that the FEM provides the best overall estimate of capacitance. However, the two-plate model appears to be reasonably good when z is in the range 15 to $25\text{ }\mu\text{m}$ as measured in the acoustic DF sensors. Thus, Eq. (3.3) should estimate the difference in electronic sensitivity between the two sensors.

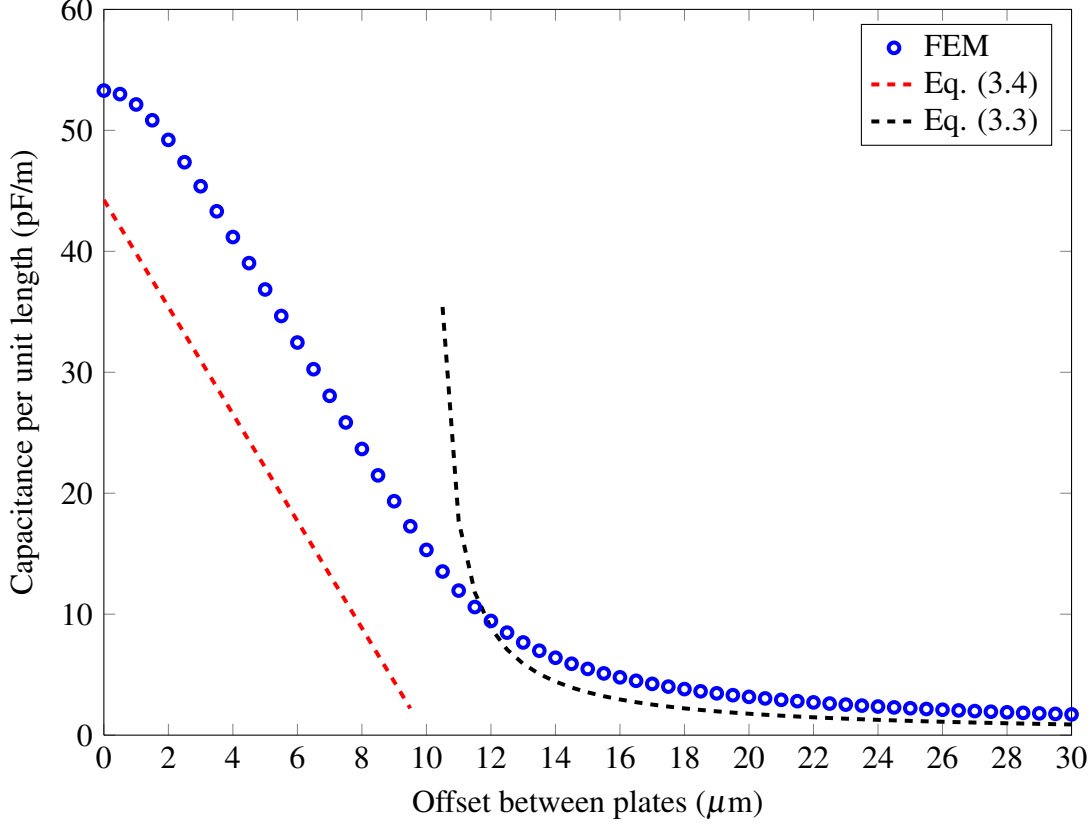


Figure 3.9: The capacitance per unit length c as a function of offset z between the two sides of the capacitor bank. Here the comb finger thickness $t = 10 \mu\text{m}$. The elementary theory, Eq. (3.4), is roughly valid where $z < t$ but neglects fringe field effects. The two-plate theory, Eq. (3.3), is reasonably accurate where $z \gg t$, and the FEM results are presumed valid everywhere.

3.2.3 Explanation of results

To use the two-plate model to compare the sensitivity of the two comb finger designs, the electronic sensitivity for each can be defined as $\eta \equiv |\Delta C / \Delta z|$. Designating these quantities η_B and η_S for the branched- and straight-finger sensors and using Eq. (3.2), their ratio is

$$\frac{\eta_B}{\eta_S} = \frac{l_B (z_S - t)^2}{l_S (z_B - t)^2}, \quad (3.5)$$

where l_B and l_S are the total length of all comb fingers for each sensor. This expression can be greatly simplified by noting that the mean offsets for the two sensors differ by less than half a micron. Thus $z_B - t$ and $z_S - t$ are approximately the same and may be canceled. With this

simplification, the ratio of sensitivities becomes

$$\frac{\eta_B}{\eta_S} \approx \frac{l_B}{l_S}. \quad (3.6)$$

Thus the branched-finger sensor, whose comb fingers have a greater combined length, are expected to produce greater output voltage for a given vibration amplitude.

To quantify the expected output difference, the values for the lengths must be inserted. The sensor with branched fingers has 66.5 spines, each holding 25 pairs of 20 μm fingers for a total length of 10.6 cm. The sensor with straight fingers has 500 finger pairs at 100 μm each for a total length of 5.00 cm. Thus, the branched-finger system should have approximately twice the output voltage for a given vibration amplitude. In fact, this is seen in the data already presented in Fig. 3.5. The vibration peak of the branched-finger sensor is just about half as high as the vibration peak of the straight-finger sensor as shown in Fig. 3.3. However, their electrical peaks are roughly equal as shown in Fig. 3.5. Thus, the branched-finger sensor's electronic sensitivity to vibration is roughly doubled as predicted by Eq. (3.6).

But does this really result in a greater overall sensitivity? At first glance, it may appear that even with this doubling, the branched-finger sensor's response in Fig. 3.5 is no better than that of the straight-finger sensor. However, it must be remembered that the sensors are designed to detect broad-band sound signals, and the peak width is as important as the height. In fact, an appropriate measure of the overall sensitivity of each sensor is the area under its resonance peak. When this integration was performed for both sensors in the mechanical response spectrum, the branched-finger sensor's total response between 2.2 and 3.0 kHz was found to be 24% less than that of the straight-finger sensor. But in the electronic response spectrum, the branched-finger sensor's integrated response was 32% greater. By this measure, the new design is clearly more sensitive as well as durable.

3.2.4 Effect of curvature on sensitivity

The above results show that for the two sensors in this study, branched comb fingers produce a greater electrical output. However, the measurements of the residual stress offset suggest a means of improving the sensitivity by an additional order of magnitude or more. Because the electronic sensitivity η is proportional to the slope of the $c(z)$ curve shown in the FEM data of Fig. 3.9, it is clear that the optimum offset z is wherever the slope is steepest. In the present case

that is somewhere between $2\text{ }\mu\text{m}$ and the device thickness $10\text{ }\mu\text{m}$. If z could be adjusted to be in this range, the slope would be an order of magnitude higher than in the present sensors, where z is predominantly in the range 14 to $25\text{ }\mu\text{m}$. Probably the simplest way to reduce curvature without adopting a whole new fabrication process would be to select a thicker device layer. Obviously this will affect the sensor's performance characteristics such as resonant frequencies, an effect that must be considered in the design.

3.3 Conclusions

In conclusion, these results show that the MEMS acoustic direction-finding sensor is made more sensitive by replacing the traditional straight capacitive comb fingers with a branched design. This design may also solve the problem of the fingers breaking when made too long. By using shorter fingers attached to a long, relatively wide spine, the branched design has greater capacitance and therefore greater sensitivity in a more robust structure. The results presented here also show that curvature due to residual stress likely reduces the sensitivity of the capacitive readout system by an order of magnitude. Armed with this understanding, we can design future sensors to maximize sensitivity by reducing curvature. These findings can be applied not only to this acoustic sensor, but to any MEMS device requiring readout of small out-of-plane displacements. Out-of-plane capacitive comb finger banks can be made more sensitive and durable by replacing the traditional straight comb fingers with a branched capacitor structure.

CHAPTER 4:

Residual stress-generated curvature reduces sensitivity

In Chapter 3 it was noted that the sensors being studied had substantial residual stress-generated curvature so that the opposing comb fingers were not overlapped at all. The residual stress is primarily due to the high-temperature doping step of the SOIMUMPs process [36]. It was also noted that the electronic sensitivity $\eta \equiv |\Delta C / \Delta z|$ (the slope in Fig. 3.9) is greatest when the offset generated by the residual stress is less than the device layer thickness. Because of the importance of this equilibrium offset in determining the sensor's sensitivity, it was useful to investigate it a little further. Three questions in particular raised themselves. First, can we develop a general rule to predict the comb finger offset at various positions on a sensor of given dimensions? Second, can we reduce the curvature, for example by including perforations in the wings? And third, does a sensor with less curvature really have greater electrical sensitivity as suggested at the end of Chapter 3?

4.1 Predicting curvature

In searching for a general rule to predict offset, it was hypothesized that the stress and strain should be roughly the same in all directions in the device plane. If so, then the curvature should be roughly constant everywhere on the sensor surface, and the surface would have a spherical shape. If it is spherical, then a plot of the offset z at various radial distances ρ from the device center will follow a circle of radius R centered at $z = R$, where R is the radius of curvature as sketched in Fig. 4.1.

Moreover, if there is a well-defined radius of curvature R , then the doping-induced residual stress in the device layer can be estimated using the well-known Stoney's formula [48] which relates curvature to stress in a thin film. If it can be established that this stress is consistent between devices, then it should be possible to predict radius of curvature based on device dimensions.

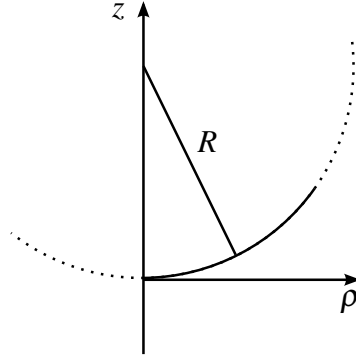


Figure 4.1: A sketch of circular curvature. If the sensor's surface has radius of curvature R , then a plot of the offset $z(\rho)$ should trace an arc of a circle with the same radius.

4.1.1 Results

To estimate the curvature, it was necessary to measure the offset carefully at a series of positions on each of several sensors. This was accomplished with the technique described in Chapter 3, using an Olympus BX51 optical microscope with a $100\times$ objective lens. With the comb fingers in view, the two sides (substrate and wing) were brought into focus one at a time as shown in Fig. 4.2, and the settings on the fine-focus knob were recorded. For this microscope and lens, each increment in the knob setting represents one micron, and thus the difference in settings is the offset between wing and substrate in microns. Using this technique, the offset can be measured with a precision of half a micron.

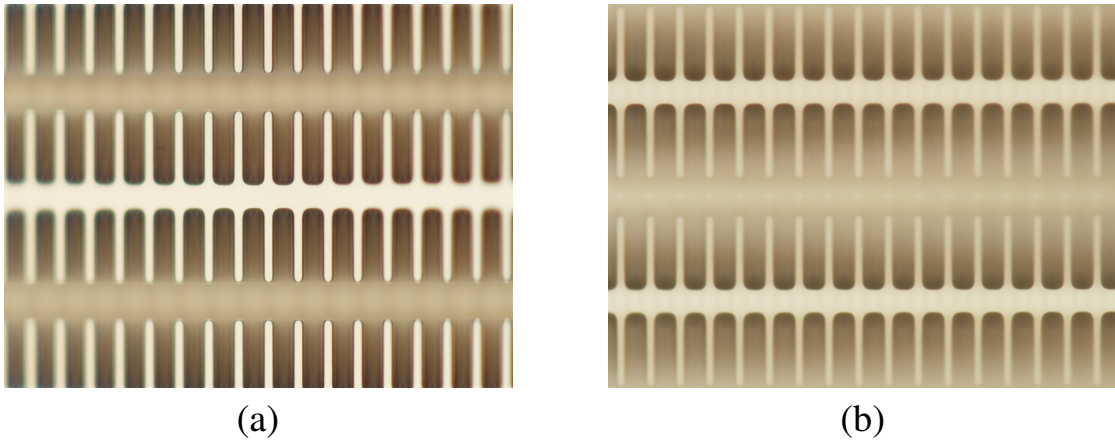


Figure 4.2: Photos illustrating the offset measurement technique. In (a) the comb on the wing is in focus, and in (b) the fixed comb attached to the substrate is in focus. The sample was not moved between photos. The offset is the difference in settings on the microscope fine-focus knob.

This technique was repeated at various positions on several sensors fabricated at different times using the SOIMUMPs process: Generation 9 with straight and branched fingers (the sensors discussed in Chapter 3), Gen. 6, and Gen. 7. All of these have device layer thickness of $10\text{ }\mu\text{m}$ except for Gen. 7 which is $25\text{ }\mu\text{m}$ thick. Measurement positions were chosen to maximize the range of radial distances ρ for each sensor; in some cases measurements were taken along the entire length of the comb finger banks, and in other cases measurements were taken only at certain positions as in Fig 4.3. For each measurement, ρ and the offset z were recorded. Finally, for each sensor z was plotted as a function of ρ , and the results were fit to a circle. These plots are shown in Figs. 4.4, 4.5, and 4.6. Some of the sensors have perforations in their wings; in the next section, it will be shown that this does not affect the curvature.

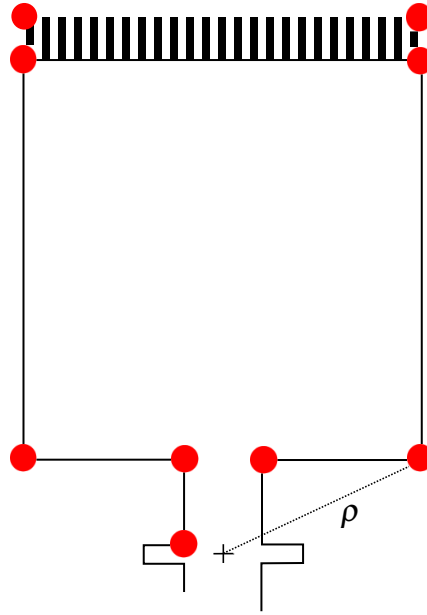


Figure 4.3: Typical positions where offset was measured on Gen. 6 sensors. The radial distance ρ is measured from the device center (crosshair) as indicated.

The measurements show that the $10\text{ }\mu\text{m}$ sensors (Figs. 4.4 and 4.5) all have a circular dependence $z(\rho)$. Moreover, they all have similar radii of curvature, between 63 and 78 mm. The thicker sensor's curvature shape (Fig. 4.6) is obviously not as well defined due to the small number of data points; it was not worthwhile to obtain more measurements on this sensor because the offset measurements were not much larger than the measurement precision. However, despite the small number of data points, circular curvature may now be assumed based on the results seen in the thinner sensors. Making this assumption, the $25\text{ }\mu\text{m}$ sensor's radius of curva-

ture is approximately 430 mm (Fig. 4.6). In other words, the thicker sensor is roughly six times flatter.

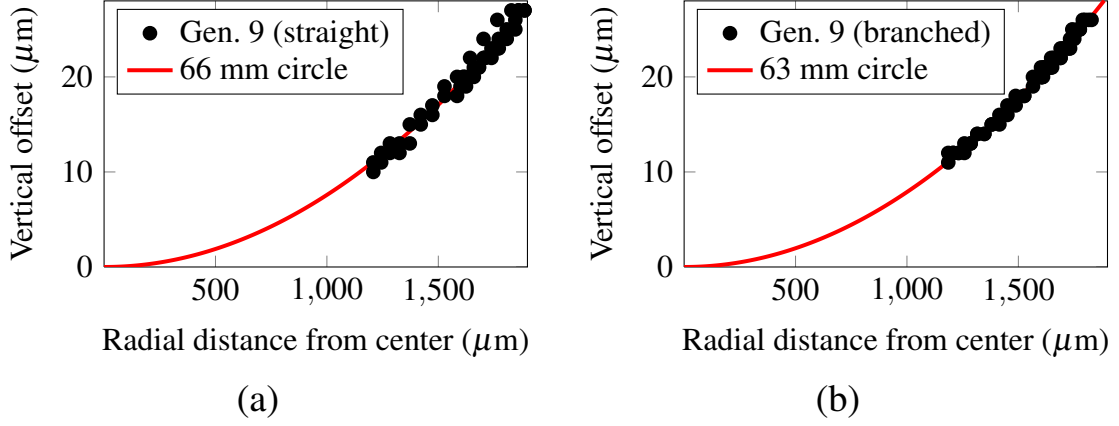


Figure 4.4: Curvature of Gen. 9 ($10\mu\text{m}$) sensors. In each case the measured data are fit to a circle with the radius noted. (a) Straight finger sensor. (b) Branched finger sensor.

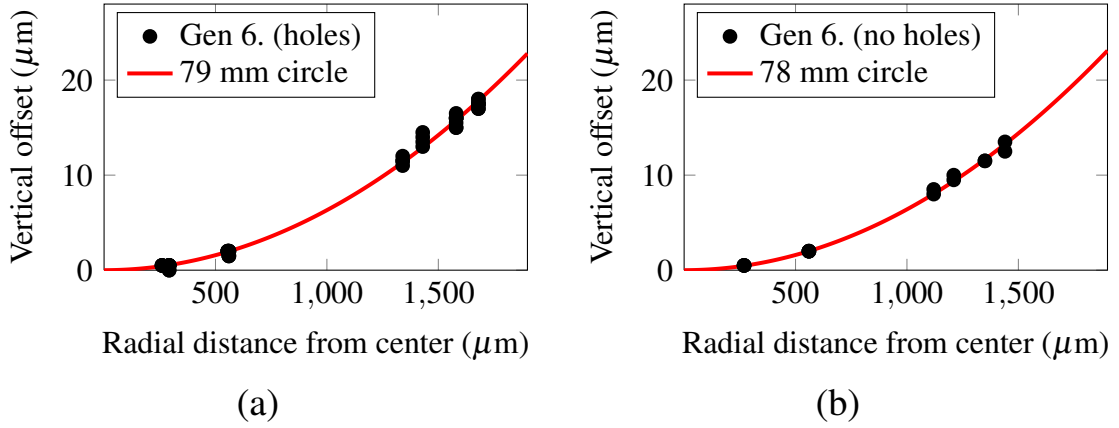


Figure 4.5: Curvature of Gen. 6 ($10\mu\text{m}$) sensors. (a) Three sensors with holes in wings. (b) Sensor with no holes.

4.1.2 Discussion of curvature measurements

To understand the results above, it is necessary to look at how stress leads to curvature. The SOIMUMPs process leaves stress mainly on the surface of the device layer [36]. The doped silicon device layer can therefore be roughly modeled as a thin film of doped silicon on top of an undoped substrate. In reality there is a doping gradient with the amount of dopant decreasing

away from the surface, but the thin-film model is a reasonable approximation. Based on this model, the curvature can be analyzed the same as if it occurred due to a thin film deposited on a substrate, a configuration that is ubiquitous in MEMS applications.

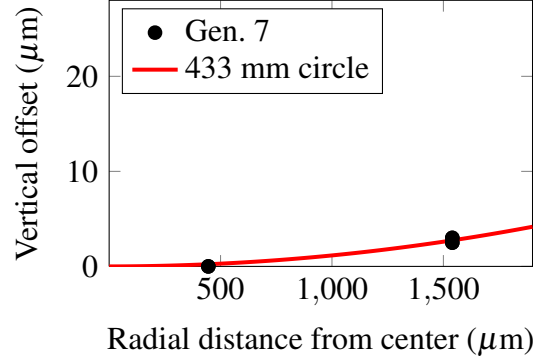


Figure 4.6: Curvature of a Gen. 7 (25 μm) sensor. Compared to the 10 μm sensors (Fig.4.4 and 4.5), the radius of curvature is roughly six times greater.

In the following analysis the device layer thickness is designated t_0 , with a doped surface film of thickness h and undoped substrate thickness $t = t_0 - h$. If the substrate Young's modulus and Poisson's ratio are E and ν , then the residual stress σ due to doping is given by Stoney's formula [48]

$$\sigma = \frac{Et^2}{6R(1-\nu)h}, \quad (4.1)$$

where R is the radius of curvature. In the case of single-crystal silicon, E and ν are tensor quantities; however, the quotient $E/(1-\nu)$ can be simplified as follows. For different directions in the (100) plane (the SOIMUMPs device plane), E varies from about 130 to 170 GPa and ν from 0.06 to 0.28 [47, Fig. 3], but the quotient $E/(1-\nu)$ remains constant at about 181 GPa.

The doped film thickness h is reported to be $1.0 \mu\text{m} \pm 0.5 \mu\text{m}$ for both the 10 μm and 25 μm device layer thicknesses [54]. The factor of three uncertainty in h leads to a similar uncertainty in σ . However, it is reasonable to assume that both h and σ are roughly the same across fabrication batches as long as the doping is conducted under the same conditions.

Even though h is not known precisely, if we can assume it is small compared to the device layer thickness t_0 , then the problem is greatly simplified. Making this assumption, $t \approx t_0$ in Eq. 4.1 and the approximate stress σ' is

$$\sigma' \approx \frac{E}{6(1-\nu)} \frac{t_0^2}{R} \frac{1}{h}. \quad (4.2)$$

Since both h and σ are roughly fixed, the ratio t_0^2/R will be a constant, providing a simple relationship between curvature and device layer thickness.

To check the range of h where this approximation is valid, the error is defined

$$\text{Error} \equiv \frac{\sigma' - \sigma}{\sigma} = \frac{t_0^2 - t^2}{t^2}. \quad (4.3)$$

Substituting $t = t_0 - h$ and neglecting terms of second order in h , this simplifies to

$$\text{Error} = \frac{1}{t_0/2h - 1}, \quad (4.4)$$

which is small when $h \ll t_0/2$. This is the condition for Eq. (4.2) to be a good approximation. In fact, the condition is met for both the 10 μm and 25 μm device layer thicknesses, since h is much smaller than half the thickness in either case.

Thus it is established that h can be treated as small. Then, as long as h and σ are reasonably consistent between batches, it is valid to assume that t_0^2/R is roughly constant as well. This simple relationship between t_0 and R provides an extremely straightforward means to estimate the curvature for a given device layer thickness.

Using the measured radius of curvature R along with the known values of t_0 and $E/(1 - \nu)$, it is trivial to estimate σ for various values of film thickness h . These estimates, computed using Eq. (4.1), are tabulated in Table 4.1. The “constant” t_0^2/R is given in units of nm ($\mu\text{m}^2/\text{mm}$) for convenience. The computed stress varies over a factor of about three to four between columns because it is roughly inversely proportional to h . However, it is reasonably consistent within columns. This is of course because the values for t_0^2/R are all roughly the same.

Table 4.1: Curvature, thickness, and stress of various sensors. The stress is computed using Eq. (4.1) with a set of h values.

	t_0 (μm)	R (mm)	t_0^2/R (nm)	Stress (MPa)		
				$h = 0.5 \mu\text{m}$	$h = 1 \mu\text{m}$	$h = 1.5 \mu\text{m}$
Gen. 9	10	65	1.54	84	38	22
Gen. 6	10	78	1.28	70	31	19
Gen. 7	25	430	1.45	84	40	26

In fact, the reported uncertainty in t_0 is $\pm 1 \text{ } \mu\text{m}$ [36], which combined with the rough value of R for the $25 \text{ } \mu\text{m}$ sensor is more than enough to account for the observed variation in t_0^2/R . These measurements could be made more precise by measuring the actual thickness t_0 of each sensor rather than using the reported values, and also by measuring curvature on a variety of $25 \text{ } \mu\text{m}$ devices instead of just one. Nevertheless, for a rough estimate of curvature, it should be sufficient to use

$$R \approx t_0^2/1.4 \quad (4.5)$$

where R is expressed in mm and t_0 in μm as above.

4.1.3 Conclusions

The preceding analysis rests on two key assumptions: first, that h and σ remain roughly the same from one fabrication batch to the next; and second, that h is much smaller than half the device layer thickness, $t_0/2$. As long as those assumptions are valid, Eq. (4.5) provides a simple relationship between t_0 and the radius of curvature. This relationship should enable reasonably good predictions of the residual stress-generated curvature in future sensor designs.

This understanding of curvature has two immediate benefits. First, it obviously can lead to design changes to reduce comb finger offset, such as smaller wing dimensions or thicker device layer. Second, a reliable curvature prediction could be used to optimize the size of reference capacitors, where there is no offset since both sides of the comb are fixed to the substrate. Ideally, these should match the wing capacitors to facilitate balancing the readout circuit. Until now reference capacitors have been designed to have the same surface area as the wing capacitors. But because the wing capacitors are effectively reduced in size by their permanent offset, their capacitance is reduced and the reference capacitance is therefore too high. A good prediction of curvature could be used to adjust the reference capacitor size to match the effective size of the wing capacitors.

4.2 Can perforations affect curvature?

It was mentioned briefly in Section 4.1 that some of the sensors whose curvature was measured have holes patterned into their wings. If the conclusions from these measurements are to be trusted, it must be shown that these perforations do not affect the curvature. If they do, then the curvature of the hole-filled $25 \text{ } \mu\text{m}$ device would not be a reliable data point and the analysis of Section 4.1 would be invalid. On the other hand, if holes do affect curvature, then they could

potentially be used to flatten the sensor wings and increase the effective capacitor size. Either way, it is important to understand the effect of holes.

Perforations have been shown to reduce residual stress by reducing the effective Young's modulus of the material [55]. The question is whether this effect could reduce the stress-generated curvature in SOIMUMPs devices. It turns out the answer is no.

4.2.1 Measured curvature with and without holes

To understand the effect of these holes on curvature, measurements of curvature on sensors with holes were compared with measurements on similar sensors without holes. The Gen. 6 sensors whose curvature is plotted in Figs. 4.5a and 4.5b provide a case study of the effect of holes on curvature. Among this group, the three sensors of Fig. 4.5a each have holes of different sizes, while the single sensor of Fig. 4.5b has no holes.

The Gen. 6 sensors have holes of 2, 5, or 10 μm square, spaced at a pitch equal to twice the hole size as sketched in Fig. 4.7. These holes are etched through the device layer after the doping step. The 25 μm sensor of Fig. 4.6 has holes 7 μm square, spaced at a pitch of 9 μm so that there is only 2 μm of silicon between holes. In all cases, the hole grid extends over the length and width of each wing. These features were incorporated for various reasons not related to curvature but provide an excellent test of the effect of holes.

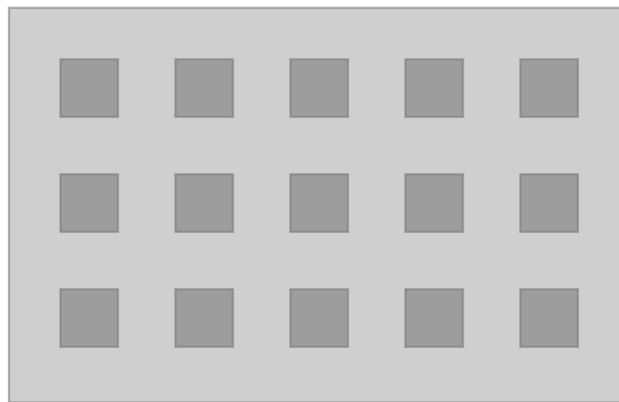


Figure 4.7: A sketch of the grid of perforations in the Gen. 6 sensors of Fig.4.5a. Holes are 2, 5, or 10 μm square and are separated by a distance equal to their size in both directions.

Comparing Fig. 4.5a to Fig. 4.5b, it is immediately clear that the radius of curvature is essentially the same regardless of the presence of holes (79 μm vs. 78 μm). Unfortunately, there was no unperforated 25 μm device available to compare with Fig. 4.6. However, it was straightforward to develop a finite-element simulation to investigate the effect of holes on curvature.

4.2.2 Curvature simulations

The finite-element curvature simulation was again developed using COMSOL (for details, see Appendix B). The model consists of a sound sensor wing with typical dimensions and a thickness of 10 μm . The wing is made of single-crystal (100) silicon, oriented so that the wing axes are along $\langle 110 \rangle$ directions. The top 1 μm of the wing is given an initial tensile stress of 35 MPa in both directions in the device plane, a value in line with the doped-layer stress values computed in Table 4.1 for $h = 1 \mu\text{m}$. The simulation was run once without holes in the wing, and then again with holes. These holes are larger (50 μm) than the holes in any of the real sensors. Larger holes simplify the model geometry and also improve visual clarity, but do not affect the outcome; simulations with smaller holes produced the same results as those with large holes or no holes at all.

Plots of the simulation results are shown in Figs. 4.8, 4.9, and 4.10. Displacement is indicated by the color scale, ranging from zero (blue) up to several microns (red). The deformation is depicted in Fig. 4.8. The total displacement at the wing corners is exactly the same with or without holes. In Fig. 4.9, contour lines are drawn highlighting that the vertical deflection increases from the device center outward. The curvature is uniform, with a radius of 108 μm as shown in Fig. 4.10. This radius is somewhat greater than is observed in the real sensors, with t_0^2/R less than 1 nm as compared to about 1.4 nm in the real sensors (Table 4.1). This discrepancy is attributable to various uncertainties. In the real sensors, the material property $E/(1 - \nu)$ and especially the doped layer thickness h may vary from the values used in the simulation. Nevertheless, the simulation result is reasonably close to the measured results.

4.2.3 Curvature and holes: discussion and conclusions

It is clear that measurements and simulation both show that holes have no effect on the curvature of these SOIMUMPs devices. This can be explained in three ways. The first is essentially a geometric argument. Considering only the doped-layer stress component in, say, the x direction, a beam oriented along x will bend upward according to that stress component. However, according to Eq. (4.1) the bending does not depend on the beam width but only on the stress,

thickness of the device layer and the doped layer, and the material property $E/(1 - \nu)$. Thus if we imagine an array of such beams side by side, their curvature is each the same regardless of the spacing between them. Finally, intersecting cross-beams between them clearly does not affect their curvature in the x direction. A similar argument applies to the perpendicular, y , direction. This collection of beams and cross-beams is essentially what is found in the hole-filled sensor wings. Just as the spacing between beams does not affect their bending, the hole size does not affect curvature.

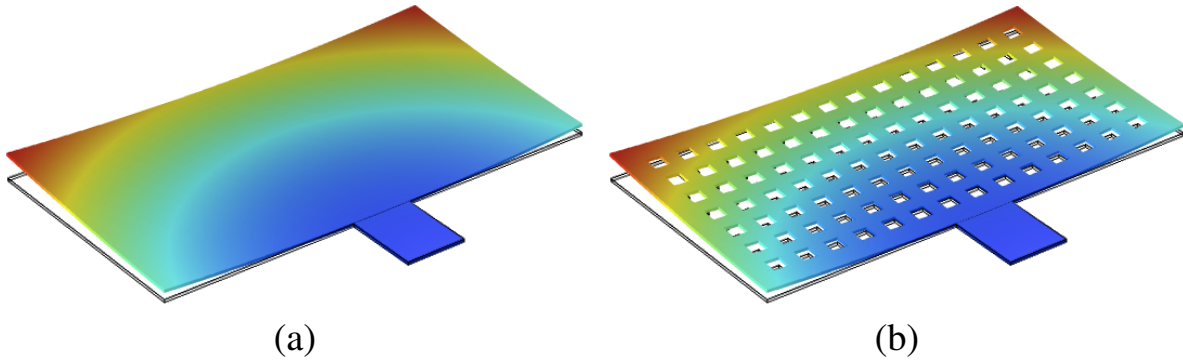


Figure 4.8: A plot of the COMSOL curvature simulation showing the vertical displacement everywhere. The simulated displacement at the wing corners is exactly the same with or without holes.

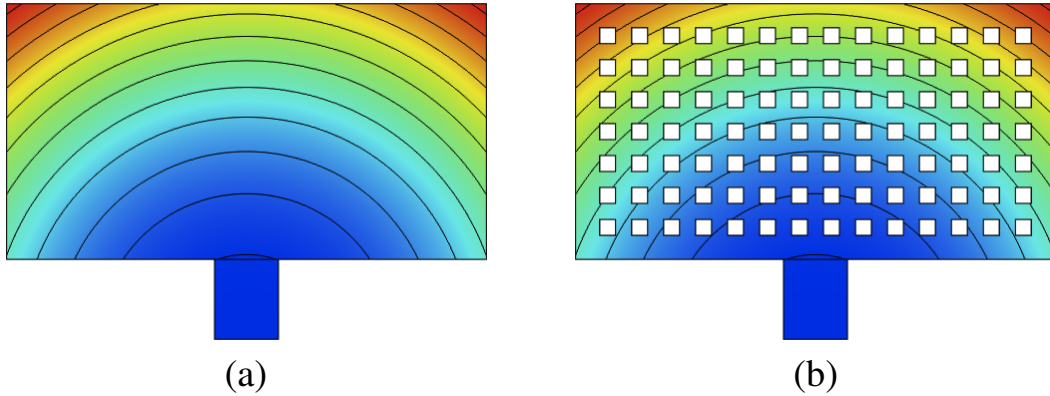


Figure 4.9: A bird's-eye view of the same simulation as in Fig. 4.8, with contour lines exactly the same regardless of holes.

A second way to explain the non-effect of holes on curvature is by looking at how holes reduce stress in the doped layer. The stress reduction is effectively a relative reduction in $E/(1 - \nu)$

v) [55]. However, in the SOIMUMPs case, the holes go through both the doped layer and the undoped layer beneath it, and therefore both layers have the same relative reduction in stiffness. Since both layers are equally affected by the holes, the overall effect is no change in curvature.

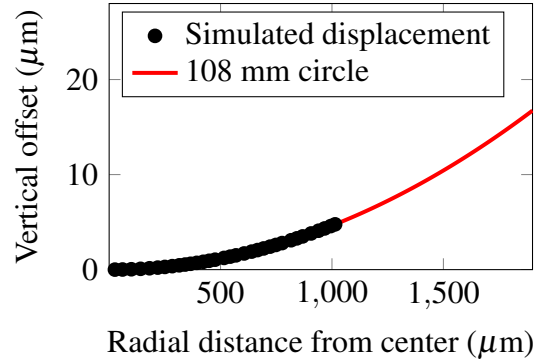


Figure 4.10: Curvature radius in the COMSOL simulation. Results were identical with or without holes.

The third explanation is probably the simplest. Since the wing is in equilibrium, the integral of stress through the device layer must be zero (the surface bends until equilibrium is reached). Etching a through-hole removes equal amounts of positive and negative stress, preserving the total curvature. The region immediately surrounding each hole will be affected, but the overall curvature will not.

Dimples etched only through the doped layer would be expected to reduce curvature. However, the SOIMUMPs process does not provide for partial etching of the device layer. Holes may continue to be useful in acoustic direction-finding sensors as a way of reducing stiffness, redistributing mass, or allowing fluid flow in areas where it is otherwise blocked. However, they cannot reduce the wingtip offset in a SOIMUMPs sound sensor. The only reliable way to do this is to choose a thicker device layer or reduce the wing dimensions.

4.3 Electrical sensitivity and capacitor overlap

In Chapter 3 it was suggested that a sensor with less curvature should have greater electrical sensitivity. This is because comb fingers that are overlapped rather than completely offset are effectively larger capacitors. Fortunately, there was a low-curvature sensor available for comparison with the Gen. 9 sensors discussed in Chapter 3. This was the 25 μm Gen. 7 sensor. As

indicated in Fig. 4.6, this sensor's comb fingers are offset by a maximum of about 3 μm , compared to the 10-27 μm offset of the Gen. 9 sensors with 10 μm device layer. In this section it is shown that the sensor with smaller offset does in fact have greater electrical sensitivity, even when normalized for the nominal capacitor size. Specifically, the output voltage (per comb finger, adjusted for device layer thickness) is greater, given the same wingtip vibration amplitude.

4.3.1 Measurements

The measurement process for this study was straightforward. Three sensors were chosen: the Gen. 9 straight- and branched-finger sensors and the 25 μm Gen. 7 sensor. In each case, the sensor was excited at its bending resonance frequency by a computer-generated, amplified sine wave signal at roughly normal incidence. The laser vibrometer was aimed at one wingtip, and the MS3110 capacitive readout IC was connected to read out the vibration-induced capacitance change. The root mean square (rms) vibration amplitude Δz was measured with the laser vibrometer, and the rms output voltage ΔV from the MS3110 was recorded at the same time. These measurements were repeated for various sound pressure levels.

The results ΔV are plotted against Δz for each sensor in Fig. 4.11. The 25 μm sensor's output is 77 V/ μm , whereas for the 10 μm sensors it is on the order of 2 V/ μm . It will be noted that the thicker sensor exhibits vibration amplitudes and output voltages that are orders of magnitude less than those of the thinner devices. This is primarily due to the higher resonant frequency associated with greater stiffness and the limited range of sound pressures that are practical to work with in the laboratory. However, the measurements show that the output is highly linear with respect to the vibration amplitude in all cases.

In order to compare sensors with different numbers of comb fingers and different device layer thicknesses, the measured output for each sensor was normalized as follows. First, the output voltage was divided by the device layer thickness and by the capacitor perimeter. Next, the results for all sensors were scaled by a common factor so that the Gen. 9 straight-fingered sensor has unit slope. This normalization enables the sensors to be compared as though they were the same except for curvature. The normalized output of each sensor is plotted in Fig. 4.12, where the slope represents the normalized sensitivity. The raw and normalized sensitivities of the three sensors are listed along with the capacitor perimeters in Table 4.2.

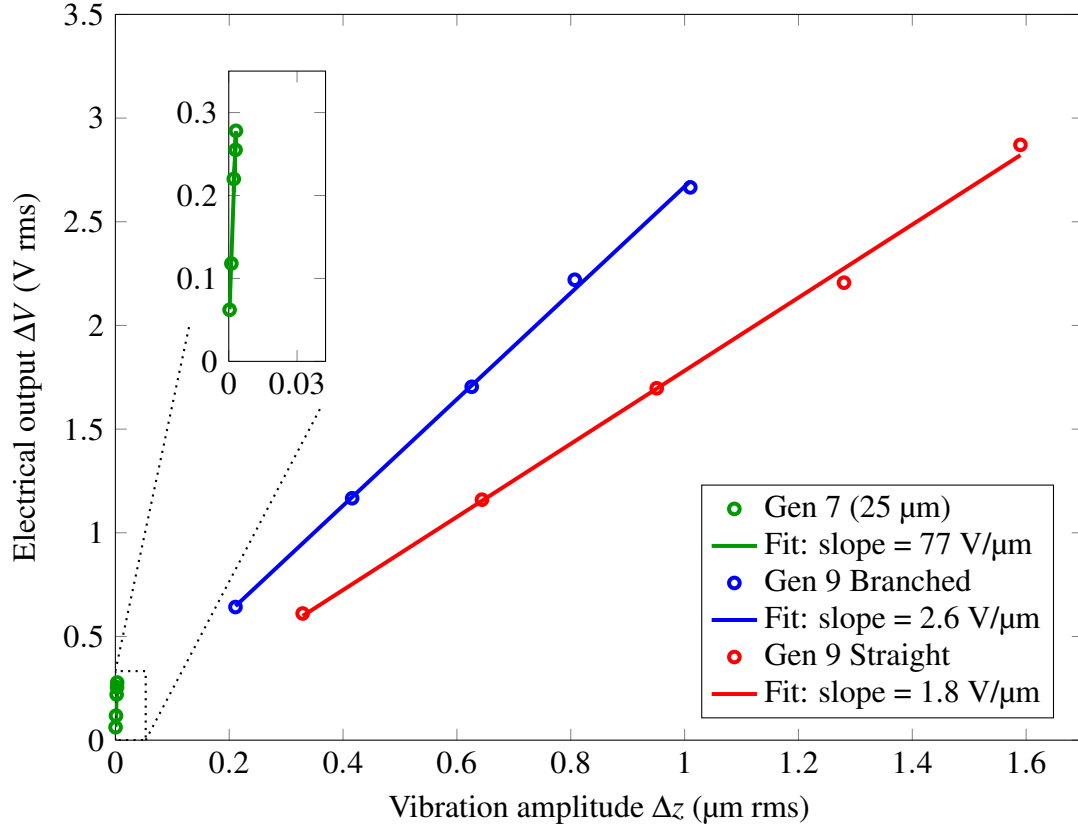


Figure 4.11: Electronic output vs. mechanical amplitude, in $\text{V}/\mu\text{m}$, of sensors with high curvature (Gen. 9) and low curvature (Gen. 7). The inset shows a closeup of the Gen. 7 plot.

4.3.2 Discussion: curvature and sensitivity

As seen in Table 4.2, the low-curvature sensor is five times more sensitive than the more highly curved sensors when their respective capacitor sizes are taken into account. The reason for this advantage was suggested in Chapter 3, where Fig. 3.9 shows the simulated capacitance per unit length of a set of comb fingers $10\ \mu\text{m}$ thick at various relative offsets z . This plot is repeated in Fig. 4.13 along with a similar plot for a $25\ \mu\text{m}$ comb finger bank. Average slopes are indicated in the regions corresponding to the measured offsets for the Gen. 7 and Gen. 9 sensors.

The electrical sensitivity is proportional to the slope of this curve, which is obviously highest when the offset is less than the device layer thickness. The Gen. 9 sensors, with their large offset, are far down the curve where the slope is low. But the Gen. 7 sensor's offset is only one tenth of its thickness, putting it nearly on the steepest part of the curve. The thicker sensor's simulated sensitivity is ten times greater than that of the thinner sensors, as indicated by the difference in slopes. Even when the sensitivity is normalized for device layer thickness (to

account for the larger surface area of the thicker comb fingers), the low-curvature sensor is four times more sensitive. This result agrees reasonably well with the measured result in Table 4.2 which shows a sensitivity ratio of about five.

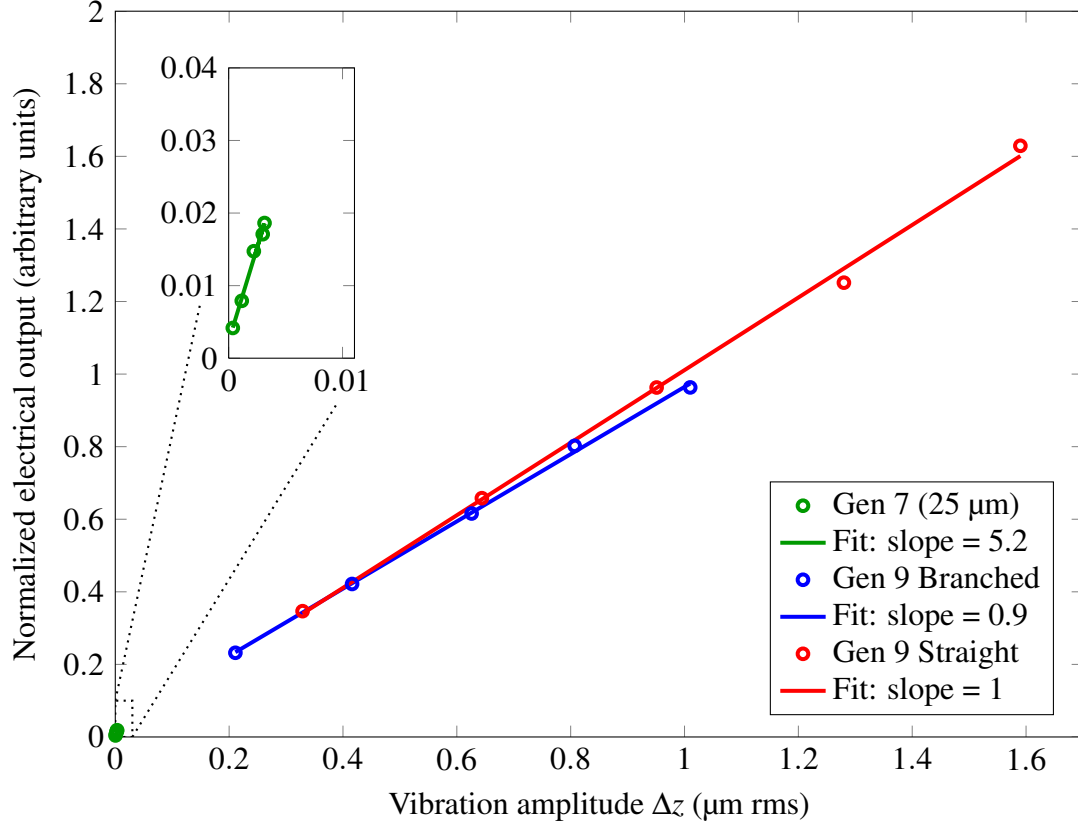


Figure 4.12: The same data shown in Fig. 4.11, normalized for capacitor perimeter and device layer thickness. For each sensor, the normalized sensitivity is the slope of the line fit to the data.

It is interesting to note that zero offset is not desirable, as both curves in Fig. 4.13 flatten near $z = 0$ due to fringe field effects, discussed in Appendix F. The maximum sensitivity occurs when the offset is anywhere between about 2 μm and the device layer thickness.

In summary, measurements and finite-element simulations indicate that the sensor with significantly overlapped comb fingers is four to five times more sensitive than the sensors with non-overlapped comb fingers. This result is normalized for the capacitor size in each case. Clearly, the greatest electrical sensitivity is obtained by designing a sensor so that the curvature-induced capacitor offset is less than the device layer thickness.

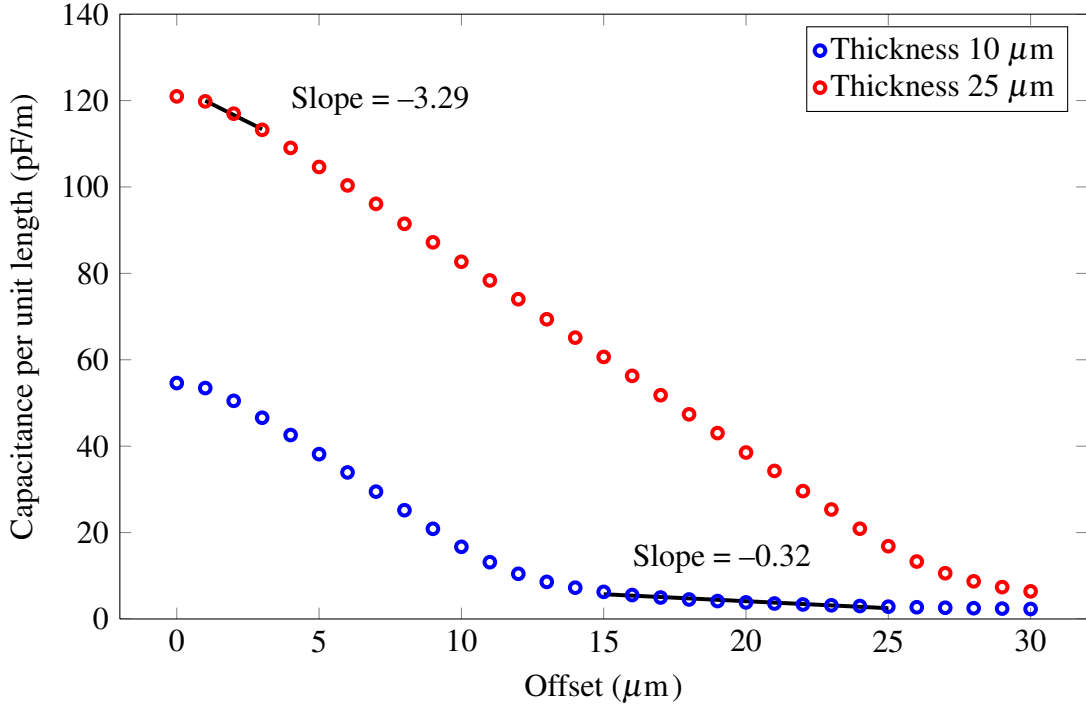


Figure 4.13: Simulated capacitance per unit length c as a function of offset z for the two different device layer thicknesses. Slopes are indicated in the regions corresponding to measurements.

Table 4.2: Normalized sensitivity. The low-curvature sensor is five times more sensitive than the highly curved sensors.

	Raw sensitivity (V/ μm)	Capacitor perimeter (mm)	Normalized sensitivity
Gen. 9 Straight	1.8	104	1
Gen. 9 Branched	2.6	163	0.9
Gen. 7 (25 μm)	77	352	5.2

4.4 Conclusions

In the acoustic direction-finding sensors, the residual-stress curvature is constant within the plane of each device, resulting in a well-defined radius of curvature. A simple rule of thumb predicts this radius given the device layer thickness. Also, holes or perforations have no effect on curvature in these SOIMUMPs devices. Finally, it is confirmed that, as suggested in Chapter 3, a sensor whose comb fingers are partly overlapped has much greater electrical sensitivity than one whose fingers are non-overlapped due to curvature.

THIS PAGE INTENTIONALLY LEFT BLANK

CHAPTER 5:

Conclusion

This body of research represents tangible progress toward a working MEMS acoustic direction-finding sensor based on the *Ormia ochracea* fly's ear. Through analytical models, computer simulations, and laboratory experimentation, several key advances have been made.

In Chapter 2 linear elastic stiffness models were presented and then validated by using a nanoindenter to measure the sensor's stiffness directly. The nanoindenter measurements verified two key assumptions about the sensor's function. First, the stiffness is linear in nature; i.e. Hooke's law applies to the MEMS structures under normal loading. Second, the resonant frequencies can be predicted using the analytical models presented. Specifically, the nanoindenter results enabled matching of the device structures to their corresponding resonant frequencies; this result validates a simple way to estimate resonant frequencies of future designs. Additionally, the nanoindenter was used to show that the sensor can be exposed to quite high sound pressures with no loss of function. The techniques presented can be applied to other MEMS sensors to verify linear stiffness, relate vibrational modes to specific structures, and conduct failure testing.

Chapter 3 presented an improved capacitive readout system using branched comb fingers in place of the traditional straight fingers. Again, the results are supported by analytical and numerical models. This system makes for more durable capacitor structures and increases electrical sensitivity to motion. These results can be applied to other MEMS sensors requiring readout of small out-of-plane displacements. Also in Chapter 3, it was discovered that the residual stress-induced curvature in the sensors greatly reduces the readout system's capacitance and therefore its sensitivity.

The nature and effect of this curvature was investigated in more detail in Chapter 4. A simple model of curvature was presented, and then verified by measurements. This model offers an extremely straightforward means of predicting curvature in SOIMUMPs structures. Perforations were also investigated, and found to have no effect on curvature. Finally, the role of curvature in electrical sensitivity was explored. It was found that a sensor with low curvature is indeed much more sensitive than one with high curvature.

The primary goal of this project is to replicate *Ormia ochracea*'s directional response to sound in a sensor with integrated capacitive readout. This has yet to be achieved. In order to design sensors that are more likely to exhibit the physics seen in the fly's ears, it will be necessary to use the results presented here. For example, accurate resonant frequency estimates based on sensor dimensions allow the sensor to be designed so that the bending and rocking frequencies are optimally separated to maximize the directional dependence. Also, reduced curvature and branched capacitors will boost the signal output of future sensors by an order of magnitude, raising the chance of detecting any directionally-dependent response. In short, the results presented here provide several essential tools for the continued development of the MEMS acoustic DF sensor.

APPENDIX A:

Sensor dimensions

This appendix provides the dimensions of the 10 μm Generation 9 sensors (SOIMUMPs run #37), which are the straight-finger and branched-finger sensors studied in Ch. 3 and some of the curvature subjects of Ch. 4. Also included are dimensions of the Gen. 7 sensor studied in Ch. 4. Dimensions of Gen. 6 (Ch. 4) and Gen. 8 (the sensor in the nanoindenter study of Ch. 2) are given in M. Touse’s dissertation [29, App. A].

Fig. A.1 shows the layout of the Gen. 9 chip. This is the proof image provided by MEMSCAP Inc. as part of the fabrication process. Sensor 1, at top left, has the branched comb fingers, and Sensor 2, top right, has the straight fingers. Sensors 3 and 4 are identical to Sensors 2 and 1 respectively. Note that Sensors 1 and 4 have features extending into the shaded area at the top left and bottom right of the diagram. This is the boundary of the “useable area” defined in the SOIMUMPs manual [36, Sec. 2.7.1]. The features outside this area were not patterned onto the device. Because of this design error, these sensors have only one wing each that is able to produce electronic output. In the malformed wings, the “device” side of the capacitor bank is electrically shorted to the rest of the chip and therefore does not function as a capacitor.

The outer dimensions of the Gen. 9 sensors (wing size plus comb finger length) are all the same: wings are 2000 μm wide including fingers and 1350 μm long. All capacitor gaps are 2 μm . Detailed dimensions are given in Table A.1 along with the Gen. 7 dimensions. Dimensions and numbers of the comb fingers are given in Table A.2.

Table A.1: Dimensions of the Gen. 7 and 9 sensors, in μm .

Sensor	Wing	Bridge	Leg	Finger
9-1 & 9-4	1800×1150	300×500	40×100	Branched
9-2 & 9-3	1900×1250	300×500	40×100	2×100
7-2	700×1150	550×700	100×100	2×100

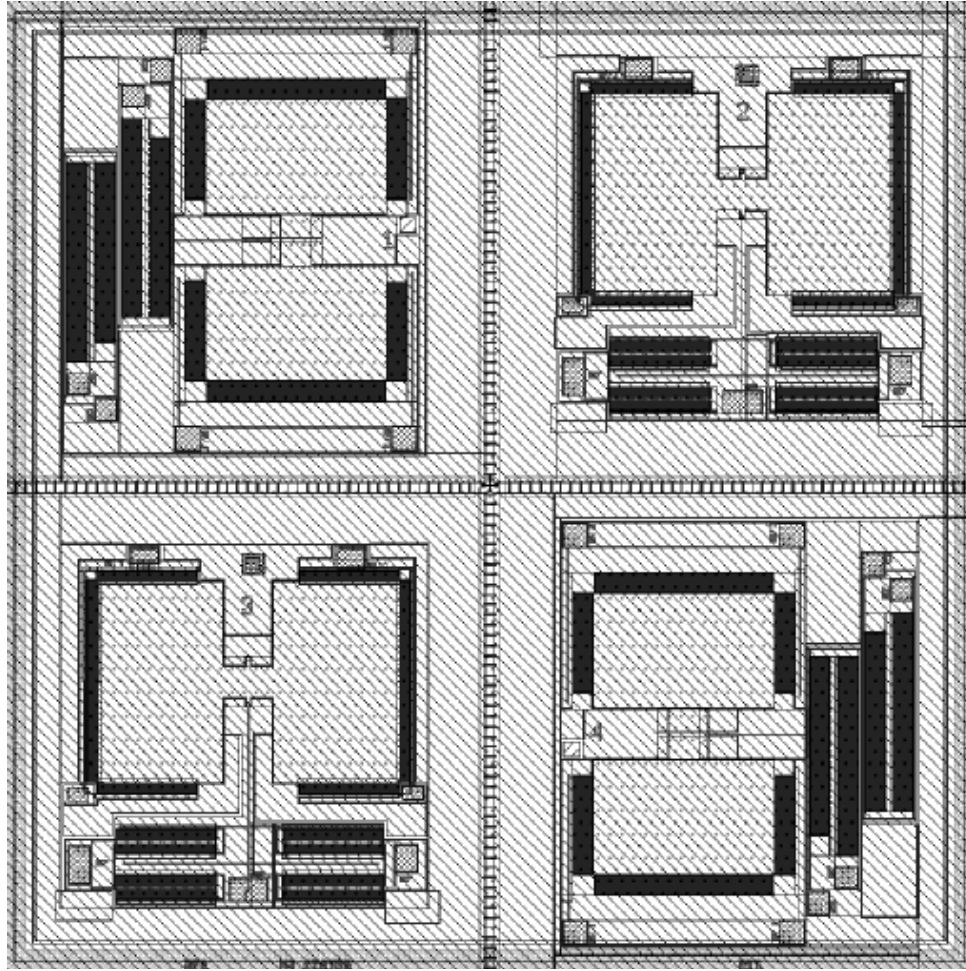


Figure A.1: Layout of the Gen. 9 sensor chip.

Table A.2: Parameters of the branched comb fingers, dimensions in μm .

Spine	6×200
Rib	2×20
Ribs per spine	25 pair
Spines on wing end	31.5
Spines on wing side	17.5 per side
Total spines per wing	66.5

APPENDIX B:

COMSOL Multiphysics models

In MEMS research, it is often helpful to use numerical models. Throughout this research, COMSOL Multiphysics simulation software (COMSOL, Inc.) was used extensively to evaluate proposed designs for new devices and to simulate various aspects of device performance including solid mechanics, electricity, and acoustic response. This appendix presents some general techniques to get the most out of COMSOL with the least time, and describes the specific models used in this work.

B.1 Recommended COMSOL techniques

In this section several COMSOL modeling techniques are presented. These techniques range from general programming principles to more specific tricks applicable to COMSOL in particular.

B.1.1 Start simple

First, start simple. Although it is tempting to begin by building the entire geometry of the finished product, this approach is rarely a good idea. As with any computer programming task, it is recommended to begin with a model that is much simpler than the one that is eventually desired, and whose accuracy can be verified by comparing with known analytical models. For example, if the desired model is a complicated structure on a cantilever beam, the initial model might be a simple cantilever beam. This approach serves two purposes. First, it makes troubleshooting much easier. By adding one layer of complexity at a time, it is obvious when an addition to the program causes a problem. By contrast, beginning with a complex program makes it much harder to identify any mistakes.

The second advantage of the start-simple approach is the ability to check the simulation's output after each addition. When the initial model performs as expected, it is relatively easy to add features one at a time, recomputing the simulation after each step to make sure it returns a sensible solution. Continuing with the example of the cantilever beam model, the first simulation might be an eigenfrequency study whose results could be compared to the textbook formula for the resonant frequency of a cantilever beam. This approach of iterative additions provides greater confidence in the final model's results.

B.1.2 Meshing

One particular challenge in MEMS simulations is meshing the model. This is made difficult by the extreme aspect ratios that are often involved in the device geometry. Device structures may be hundreds or even thousands of microns across but only a few microns thick, with some features even smaller. These extreme ranges of size can make it very difficult to build a model mesh that works. Often it is challenging just to get the mesh to build without errors. It can be even more challenging to create a mesh with few enough elements to be solvable with the computing power available. However, there are a couple of techniques that may be helpful.

First, avoid meshing parts of the model where no interesting physics is happening, for example the substrate wafer. If possible, build the model geometry so that these areas are not included in the simulation at all. For example, in an acoustic model, any domain with a “hard” boundary is probably safe to remove from the simulation.

For models with air included, it may be helpful to create separate domains where there is air between small device features. It may seem natural to build only the solid material into the model geometry, leaving the air space around the device as one big domain. However, the software may have a much easier time meshing the model if each small air space is a separate domain. This technique makes it somewhat more complicated to build the model geometry, but the extra time spent on the geometry will pay off if the software is able to create a suitable physics-defined mesh without user intervention.

Often, mesh elements tend to be concentrated in corners even when the physics of the model does not require such concentration. In that case, it may be possible to reduce the number of elements by meshing the corner edges first using an Edge mesh of the desired size.

If it does become necessary to build a user-defined mesh, some general guidelines apply. First, it is best to work from the inside out, in the sense that the smallest features should be meshed first. For large, flat structures such as those often appearing in MEMS devices, it may be helpful to use a two-dimensional mesh such as `Free Triangular` on one of the surfaces and then “sweep” it through the structure. If a `Swept` mesh is used, it must be remembered that the edges of the structure will be covered with rectangular elements. These must be divided into triangles using `Convert` before they can be joined with a tetrahedral mesh. Also, if a swept mesh is used, it is advisable to assign it a `Distribution` of at least 3 elements, and make it fine enough so that the height of the elements is not much less than their width and length.

B.1.3 Anisotropic material

In addition to meshing, it can be challenging to incorporate the anisotropy of single-crystal silicon. Single-crystal silicon is available in the materials database, but if the model to be simulated is not oriented along $\langle 100 \rangle$ directions, then the elasticity matrix needs to be rotated accordingly. In particular, a standard wafer as used in SOIMUMPs [36] is oriented along $\langle 110 \rangle$ directions. For such a wafer, the orthotropic elasticity constants and the elasticity matrix are given in the excellent paper by Hopcroft et al. [47, Eq. (8)]. Once these values have been entered, it may be useful to save the material to the list of user-defined materials for future use.

B.1.4 Tiny features

If comb finger capacitors or other tiny features are incorporated into the MEMS device, it may not be practical to include them in the simulation model due to their large numbers and small size. Depending on the physics to be explored with the model, the means of simulating comb fingers can vary. For simulations involving air, they may be simulated by a drag force applied to the location of the comb finger bank. For example, in the case of harmonic motion a frequency-dependent drag force proportional to velocity may be applied. This can be done using the automatically generated velocity variable, by multiplying the velocity at each point in the comb fingers by the appropriate drag coefficient [7, 56, 57] and then applying the resulting force to the surface. For simulations involving solid mechanics, such as computing resonant frequencies, comb fingers may be simulated by a reduced-density material. For example, if each comb finger is $2\text{ }\mu\text{m}$ wide and the gaps between them are also $2\text{ }\mu\text{m}$ wide, then the density of the moving side of the comb bank is one fourth that of the device material.

B.1.5 Computing capacitance

For electrostatic models, there is an easy way to compute the capacitance of a model. Where a voltage is to be applied, define a `Terminal` boundary condition instead of `Electric Potential`. When the simulation is complete, the `Terminal` creates a global variable `es.C11` that can be accessed from `Derived Values` as a `Global Evaluation`. There is then no need to compute capacitance by integrating energy density or surface charge.

B.1.6 Infinite element domains

Often in electrostatic simulations it is desirable to have a boundary condition such that the potential goes to zero at infinity. This can be accomplished very neatly using the Infinite Elements feature, which creates a series of domains around the model that the simulation will treat as exponentially increasing in size. At the risk of getting too version-specific, here is a guide to using infinite elements as of COMSOL 4.3:

1. Enclose the model geometry with a sphere, cylinder or box (circle or rectangle in 2D) as the bounding domain.
2. Add domains where the infinite elements will go. The easiest way to do this is using layers. With the bounding domain highlighted in the Model Builder, open the Layers tab and enter a thickness for Layer 1. Use the check-boxes to select where layers should be added, then build the geometry.
3. Right-click Model->Definitions and select Infinite Element Domain. This creates a new set of domains inside the layer created in the previous step. While Infinite Element Domain is highlighted in the Model Builder, select the appropriate coordinate system for the geometry of the bounding box. Finally, enter the coordinates of the center of the bounding box under Center Coordinate. If the coordinate system and center coordinate are not chosen correctly, the infinite elements will not work.
4. Mesh the model excluding the infinite element domains as desired, but in the infinite element domains, use a Mapped mesh. Along the edges connecting the inner and outer boundaries of the infinite element domains, add a Distribution of 5 or more elements.
5. To avoid showing the infinite element domains in the results plot, attach a Selection to the Solution. In this selection, choose only the domains that should appear in the results plot.

Similar techniques apply to the use of the Perfectly Matched Layer feature, which is applicable to frequency-domain models.

B.1.7 Symmetry in acoustic models

In many cases, it may be possible to exploit symmetry to simplify a model and reduce the number of mesh elements. However, it is not obvious how to tell COMSOL to treat a model as one half of the whole model. In the case of an Acoustic-Structural Interaction model, there are three essential steps and one important caveat. The three steps are:

1. Apply a Sound Hard Boundary condition on the air boundary at the symmetry plane.
2. On the other air boundaries of the model, apply a Cylindrical Wave Radiation condition, or similar condition appropriate to the boundary geometry. Make sure the Sound Hard Boundary condition at the symmetry plane is not overridden.
3. Apply a Symmetry condition on the solid material boundaries at the symmetry plane.

The important caveat is that the Symmetry condition precludes the simulation of antisymmetric modes. To find these modes, the model must be modified and re-run with an Antisymmetry condition at the symmetry plane in the solid material.

It is advisable to build a full model for comparison, to make sure the symmetry is properly accounted for in the partial model. However, once that is ascertained, the partial model may be more efficient than the full model.

B.2 Models used in this project

A COMSOL solid mechanics model was used to estimate the flexing mode deflection depicted in Fig. 2.4, to estimate the elastic stiffness $k(x)$ as shown in Fig. 2.8, and also to estimate the rocking and bending eigenfrequencies in Table 2.3. Electrostatic models were used to simulate the capacitance $c(z)$ as shown in Fig. 3.9 and 4.13. The graphics in Fig. 4.8 and 4.9 were produced using a second solid mechanics model to simulate the curvature due to surface stress. The same model generated the simulated $z(\rho)$ values in Fig. 4.10. In this section these models are described in more detail.

B.2.1 Linear Elastic Stiffness

The stiffness simulation whose results are shown in Fig. 2.4 and 2.8 and Table 2.3 was a 3D Solid Mechanics model. Various values were defined as Parameters, including sensor dimensions, nanoindenter tip position along the x and y axes, the load applied by the nanoindenter, and several different mesh size parameters to facilitate adjusting the mesh fineness.

The model geometry was built in a single Work Plane and extruded through the device layer thickness. The sensor legs, wings, bridge, and comb fingers were represented as rectangles and the nanoindenter tip was represented as a circle. Even though this circle was much larger than the actual tip, it was still quite small compared to the other model features. To facilitate meshing, a larger concentric circle was added around the tip. The sensor wings were divided

into a central section, along the x axis, and two outer sections. This division enabled the mesh to be finer along the axis, where the load was to be applied, and coarser elsewhere. COMSOL's Mirror feature was used to simplify the geometry description by exploiting the symmetry of the model. The geometry is shown in Fig. B.1.

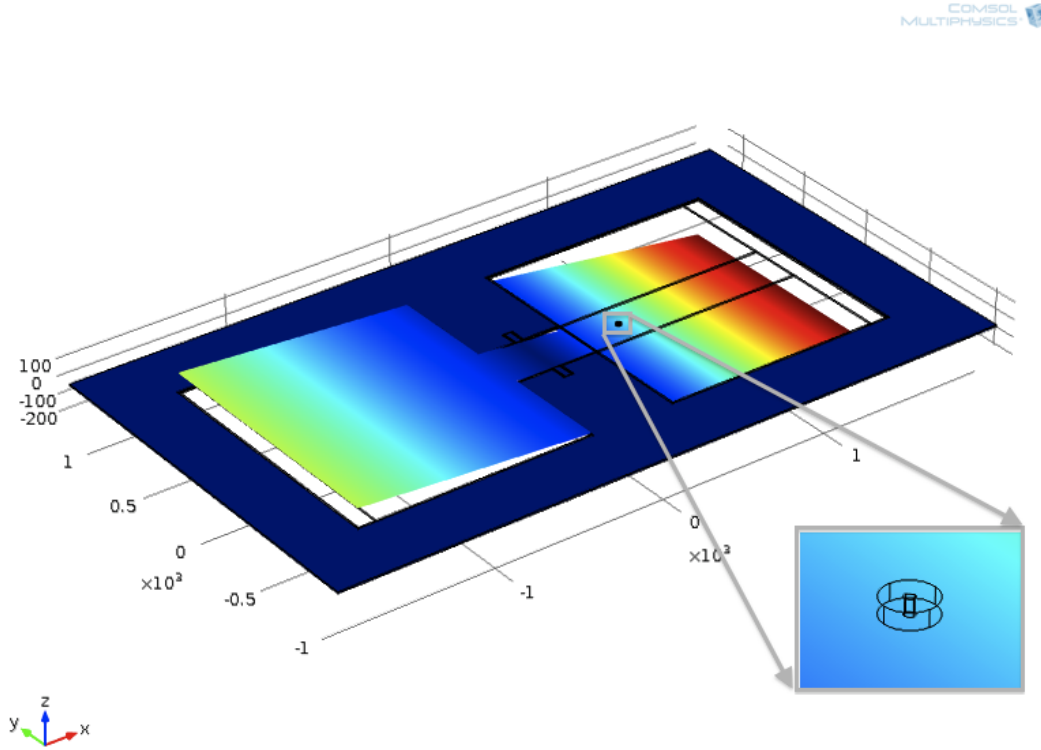


Figure B.1: The linear elastic stiffness model. The inset shows the extruded concentric circles representing the nanoindenter tip.

The main model material was $\langle 110 \rangle$ silicon, but the comb fingers were modeled using the same material with one quarter the density as explained in Ch. 2. The material was modified from the single-crystal silicon material in the COMSOL Material Library by editing the anisotropic properties using Orthotropic values given by [47, Eq. 8]. For the lower density material, the density was edited in the Linear Elastic Model condition applied to the comb finger domains.

The boundary conditions were a Fixed Constraint on the substrate domain and a Boundary Load at the nanoindenter tip boundary. The load was applied only to the inner of the two circles. The outer circle was used only to help the software with meshing.

To mesh this model efficiently, several steps were used. First, a Free Triangular mesh was applied to the top boundaries of the tip, the outer circle around the tip, and the legs. A Size was applied to this mesh which defines a maximum element size given by one of the model parameters. This was the finest mesh used. Next, a second Free Triangular mesh was applied to the top boundary of the bridge. This mesh was also given a Size with a higher maximum element size, also parameterized. A third Free Triangular mesh was applied to the wing center sections and given a Size of Extremely Fine, which was coarser than the first two meshes. To complete the mesh of the top surface, the substrate and outer wing sections were meshed with a fourth Free Triangular mesh of Normal size. Thus, the parts of the model where most of the physics occurs were given the finest mesh. Finally, the mesh was Swept through the model thickness and given a Distribution of three elements.

To find the optimum mesh size parameters, an Eigenfrequency study was repeated for various mesh sizes. As the mesh was made finer and finer, the eigenfrequencies returned by the simulation converged to particular values. The optimum mesh size was then chosen to be the coarsest mesh that returned eigenfrequencies within a tenth of one percent of the converged value. For this model, the final maximum element sizes for the finest meshes were 8 μm and 12 μm respectively. This eigenfrequency study was used to produce the simulated rocking and bending frequencies reported in Table 2.3.

The primary purpose of this model, however, was to estimate the sensor's linear stiffness $k(x)$. To accomplish this, a Stationary study was added, with a Parametric Sweep of nanoindenter tip positions. When this study was computed, the stiffness values were extracted by means of a Surface Average (found under Derived Values). The Data Set was the parametric solution, the Parameter Selection was All, and the boundary Selection was the nanoindenter tip boundary. The Expression was defined as the nanoindenter load parameter divided by the generated variable `solid.disp`, where the load corresponds to F in Ch. 2 and the simulated displacement `solid.disp` corresponded to $d(x)$. When evaluated, this expression produces a table of $k(x)$ vs. x , the values plotted alongside analytical models and measurements in Fig. 2.8.

The same model was used to evaluate the so-called flexing models as shown in Fig. 2.4. In that case the nanoindenter tip was kept at $x = 0$ and a Parametric Sweep was run on the y tip position. The simulation returned the displacement $d(y)$, which was plotted as the deflection in Fig. 2.4.

B.2.2 Capacitance vs. offset

In Ch. 3 and 4 a COMSOL model was used to estimate the capacitance per unit length c as a function of offset z , in Fig. 3.9 and 4.13. This was a 2D Electrostatics model.

In this model, the offset was a Parameter, as was the number of comb finger pairs N to be simulated. The geometry was very simple. A rectangle represented one of the fixed comb fingers, and an Array was generated to make N copies spaced the appropriate distance apart. The rectangle corners were rounded using Fillet to simulate the real comb fingers, whose corners are somewhat rounded due to the fabrication process. A Copy of the fixed array was made to represent the moving comb fingers. A larger rectangle was then created to bound the model, and a Difference was applied to subtract the comb fingers from the bounding box. This had the effect of removing the interiors of the comb fingers from the model entirely, so that they were not meshed. This was acceptable since they were to be treated as perfect electrical conductors. Finally, an Infinite Element Domain was used to simulate the bounding box extending to infinity. This geometry is partly shown in the cropped images of Fig. 3.8.

For this model, materials were not important as long as the material between the comb fingers was given relative permittivity $\epsilon_r = 1$. It was adequate to define an artificial material with only that property.

In the Electrostatics simulation, a Ground condition was applied to the fixed comb fingers and a Terminal of constant non-zero voltage to the moving fingers. An Electric Potential could have been used instead, but would not have provided the built-in capacitance computation provided by the Terminal condition.

The mesh in this model was a Free Triangular applied to all domains except the infinite elements at the edges of the model. In those elements a Mapped mesh was used with a Distribution along selected edges between the inner and outer boundaries of the infinite element domain.

To find the optimum number of comb finger pairs to simulate, a Parametric Sweep was run with N ranging from small to large values (the size of the bounding box was parameterized based on N as well). Values of N larger than 25 produced essentially the same capacitance, so $N = 25$ was used for the final model.

To compute the capacitance per unit length, a Stationary study was run, with a Parametric Sweep of offset ranging from zero to 30 μm . The capacitance was retrieved by creating a Global

Evaluation as follows. The Data Set was the parametric solution, and the Parameter Selection was All. The Expression to be evaluated was `es.C11`, which was the capacitance of the entire model returned by the Terminal condition. However, since this included all the capacitor gaps, it was divided by the number of gaps ($2N - 1$). When evaluated, this expression produced the capacitance per unit length as a function of offset, or $c(z)$ as in Fig. 3.9 and 4.13.

B.2.3 Perforations and curvature

The simulations of curvature in sensors with and without perforations in Ch. 4 were made using another 3D Solid Mechanics COMSOL model (see Fig. 4.8, 4.9, and 4.10).

In this model the wing and bridge dimensions were parameterized, as were the doped layer thickness h and a value for stress. For the geometry, a Block was created for the undoped layer of the wing and similarly for the bridge. Another block was inserted to represent one of the perforations, and an Array was made from that. A Difference was then applied, in which the perforations were subtracted from the wing and bridge. This process was repeated for the doped layer.

The material used in this model was $\langle 110 \rangle$ silicon with the rotated stress tensor applied using the Anisotropic setting in the Linear Elastic Material model. The residual stress was simulated by applying an Initial Stress and Strain to the doped layer. The stress matrix consists of the (negative-valued) stress parameter in the x and y diagonal elements and all other elements zero. Finally, a Fixed Constraint was applied to the end of the bridge.

The mesh in this model was a Free Triangular mesh on the top surface, Swept through the doped layer and then Swept again through the undoped layer. The swept mesh in the undoped layer was given a Distribution of three elements. Finally, the deformation was computed by running a Stationary study. To compare the deformation with and without perforations, the model was rerun with the perforation geometry elements disabled.

The plots of Fig. 4.8 were generated by creating a 3D Plot Group with a Surface plot of the generated displacement variable `solid.disp`. The contour lines shown in Fig. 4.9 were added by adding a Contour to the 3D Plot Group. Finally, the offset z as a function of radial displacement ρ was found by creating a Cut Line 3D along the model centerline, then adding a 1D Plot Group with a Line Graph of the expression `solid.disp`. The data from this line graph were exported as a table using the Export feature. These data were used to plot Fig. 4.10.

THIS PAGE INTENTIONALLY LEFT BLANK

APPENDIX C:

Wire bonding

In order to perform any experiments involving the electronic readout from the MEMS device, it was necessary to make electrical connections between the device and the chip carrier it was mounted on. These connections were made using the Kulicke & Soffa 4524D wire bonder, shown in Figure C.1. Researchers who need to use the wire bonder should expect that it will take several hours of practice to become proficient. While that learning period is unavoidable, the guidelines presented here may hasten proficiency and improve early outcomes.

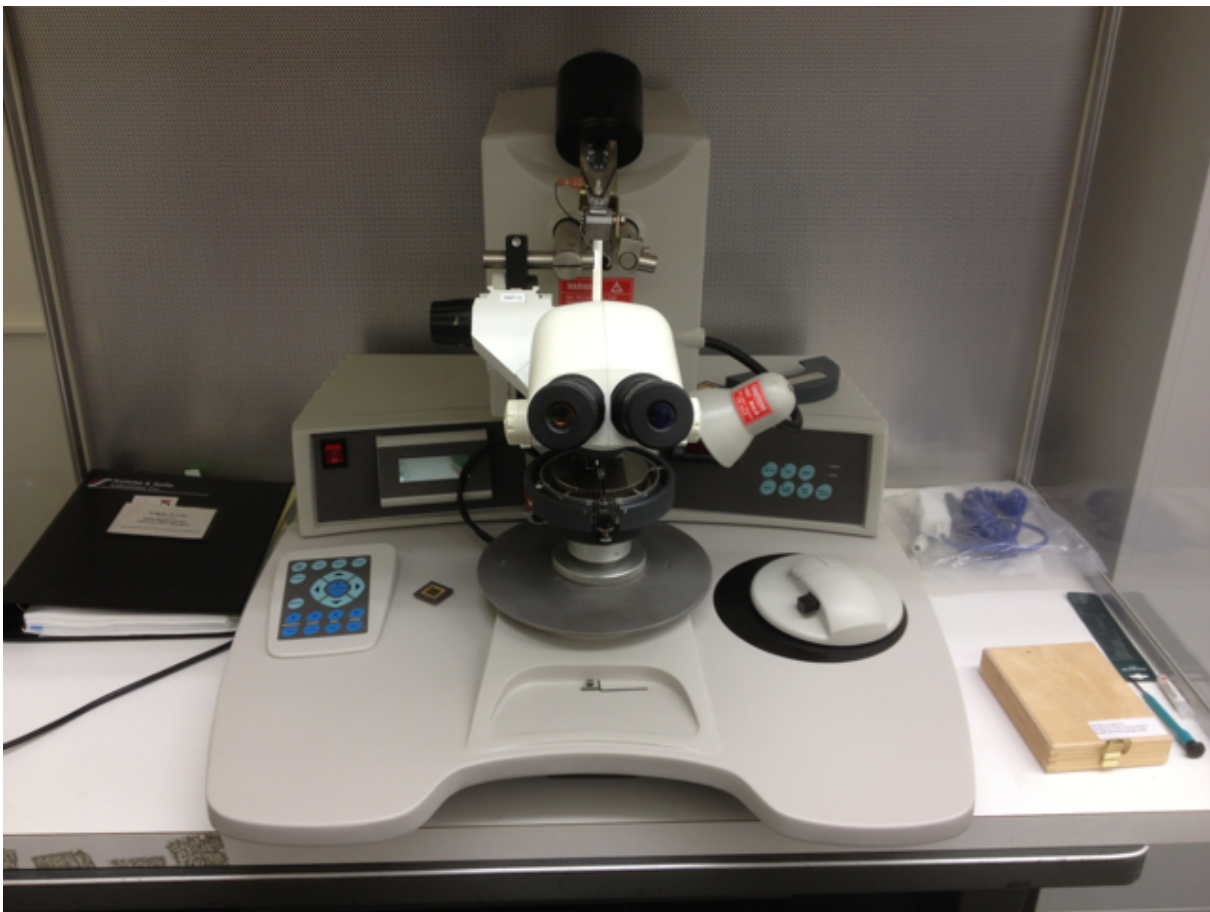


Figure C.1: The Kulicke & Soffa 4524D wire bonder.

The operating manual for the wire bonder is fairly complete and easy to read. This guide does not replace the manual, but describes where to find the necessary instructions and provides some additional information that may be helpful.

The wire bonder can be operated in semiautomatic mode or in “Manual Z” mode. Between the two, the manual mode is recommended, as it produces more reliable bonds and is easier to use. This guide assumes the use of the manual mode.

The basic steps involved in wire bonding are:

1. Place the chip carrier onto the workholder.
2. Turn on the wire bonder.
3. Set the bonding parameters.
4. When the workholder reaches working temperature, create bonds.
5. Turn off the wire bonder.
6. Remove the chip carrier when it is cool enough to handle.

The remainder of this guide focuses on setting the bonding parameters and creating the bonds, but first some of the wire bonder parts are described.

C.1 Wire bonder parts

The wire bonder is described in detail in the operator’s manual. Three key parts necessary for basic operation are shown in Figures C.2 and C.3. First is the capillary, indicated by the arrow in Figure C.2. The capillary is the white pointed tube that guides the end of the wire. Second is the the Negative Electronic Flame Off (N.E.F.O.) solenoid. The N.E.F.O. solenoid is used to create a new ball on the wire end when necessary (see Section C.3). Last is the capillary unplugging, shown in Figure C.3. The unplugging is used to clean out the capillary when it gets clogged with bits of wire.

C.2 Bonding parameters

Before using the wire bonder, the bond parameters must be set. This is done using the liquid-crystal display and keypad, and may be done while the work surface is warming up. Bond parameters for 25 μm gold wire are found in the wire bonder manual on p. 6-32, and are not repeated here.

When the wire bonder is turned on, the work surface begins to heat up. The recommended temperature setting is 120 °C. While the surface is heating, the bond parameters may be set

using the display. The first screen on the display prompts the user to enable or disable the password. Highlight DISABLE by using the arrow keys, then press the ENTER key.

The next screen contains the settings for the first of the two bonds, as indicated by the highlighted numeral “1” at the top of the display. See p. 4-13 of the manual for the description of the screens and how to set the parameters. The SEARCH setting controls the height of the wire in semi-automatic mode and may be ignored if using manual mode as recommended. The remaining parameters for the first bond should already be set to the recommending settings. If necessary, they may be adjusted using the arrow keys to select a parameter and the plus/minus keys to adjust the parameter setting. To continue to the next screen, use the down arrow key.

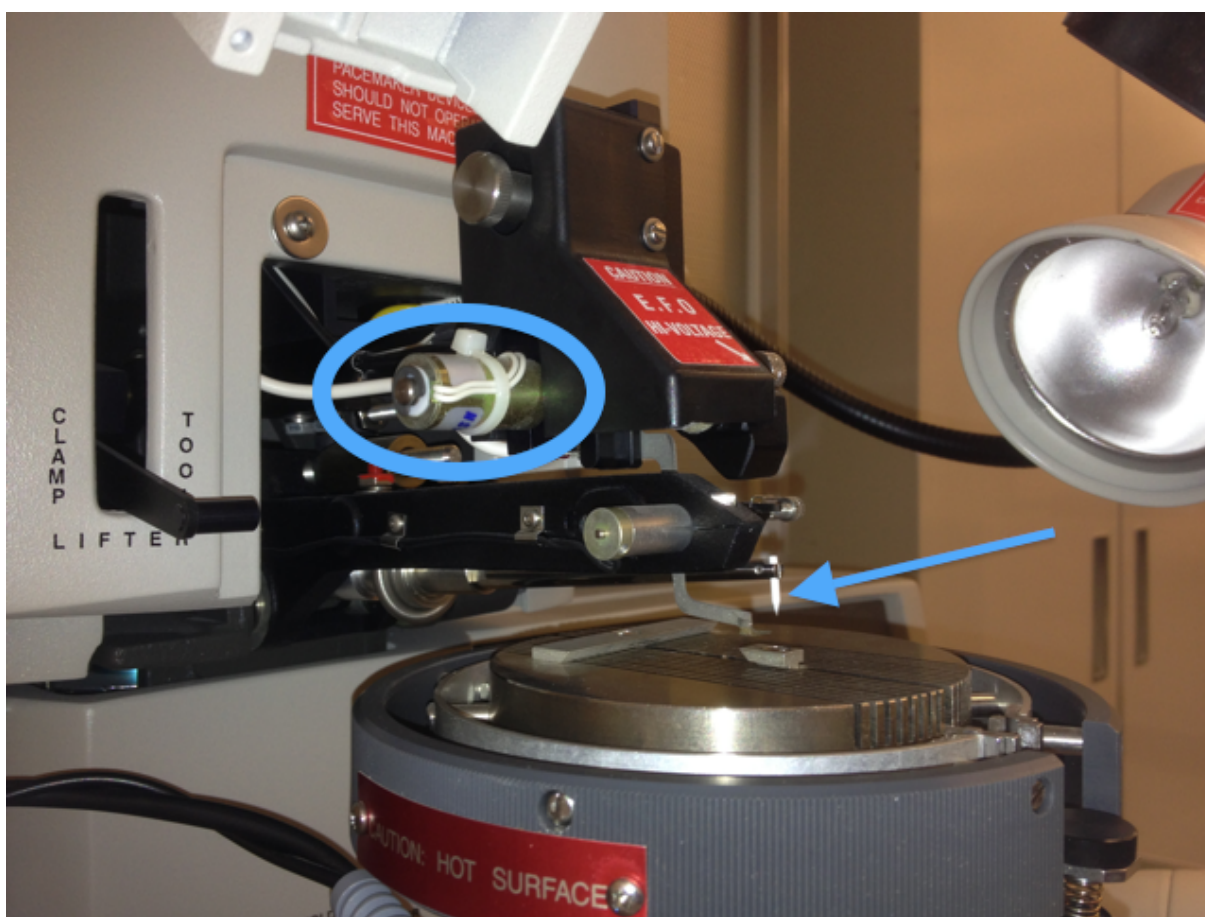


Figure C.2: A closeup view of the wire bonder, showing the locations of the capillary (arrow) and the N.E.F.O. solenoid (oval).

The second screen contains the settings for the second bond, as indicated by the highlighted numeral “2” at the top of the screen. As with the previous screen, if using the manual mode,

SEARCH may be ignored. Parameters POWER, TIME, FORCE, and BALL are adjusted using the arrow keys. Parameters LOOP and TAIL each have dedicated plus/minus keys.

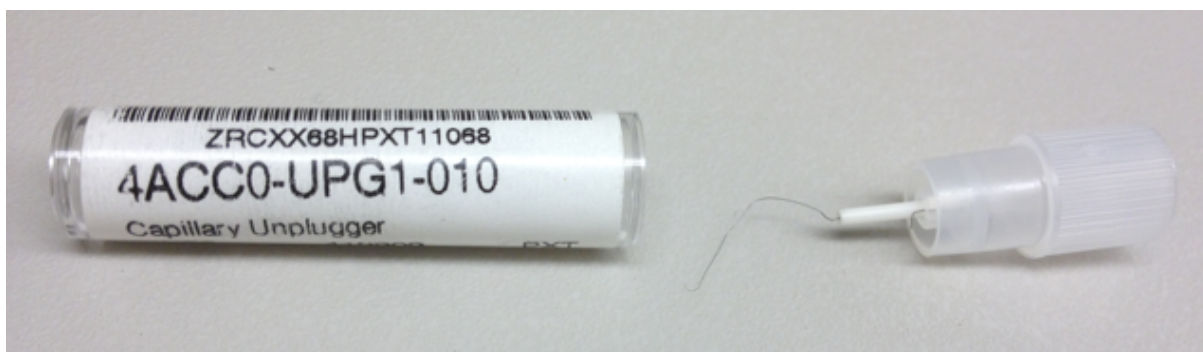


Figure C.3: The capillary unplugging and its container.

It is important to navigate back to the screen for the first bond before starting to bond. If bonding is started while the second screen is displayed, the wire bonder will use the wrong settings and will not bond properly.

C.3 Normal operation techniques

Operation of the wire bonder is explained in the operating manual. In particular, Section 6.3.1 on p. 6-23 covers creation of a ball on the wire end, and Section 6.3.2 covers “Manual Z” bonding starting at the bottom of p. 6-25. Rather than reproducing those instructions, this section covers recommended techniques and common problems. Again, the manual bonding technique is recommended and is assumed to be used throughout this guide.

Wire bonding technique is a skill that must be developed through practice. However, there are some tips that may help the novice. First and foremost is to plan carefully before starting. It is much easier to make short bonds than long ones. Before beginning a wire bonding job, the bonds should be mapped out to minimize the length of each and to ensure that they will not overlap. If possible, devices should be designed with this in mind, so that bonding pads are close to the edges and positioned so that bonds do not need to overlap each other.

When it is time to begin bonding, the most important technique recommendation concerns the method of positioning the work surface under the fixed capillary. Although the work surface can be moved by moving the mouse, this is not the easiest way to control the position of the

work surface. Instead, it is recommended to hold the mouse fixed with the right hand and use the left hand to directly slide the workholder into position. Compared to moving the mouse, this technique provides better control of fine movements.

The second matter of technique involves creating bonds with a good arc, which is important in order to prevent a bond from contacting the wrong surfaces, including other wire bonds. This is much easier with short bonds than long ones. Getting the desired arc is somewhat of an art form, but is worth learning. The arc height may be controlled by adjusting the length of wire pulled out between the first and second bonds. Once the wire is the desired length, the capillary is slowly lowered toward the surface where the second bond is to be made. As the capillary approaches the surface, the wire must be kept slack enough so that the portion of wire extending out of the capillary is not stretched tight to the side. With proper slack, when this portion of wire touches the surface, it bends upward, creating the desired arc just before the second bond is made. If the wire is stretched too tight to the side, it will not make a good arc. On the other hand, if the wire is too loose, it may sag. Again, the best way to make good bonds is to keep them as short as possible.

Finally, on some surfaces with poor adhesion properties it may help to place a ball on the surface before attempting to make a bond. This ball then becomes the new surface to be bonded to. To make the ball on the surface, a bond is created at the desired position and then the second bond is placed directly on top of the first one.

C.4 When something goes wrong

Manual bonding is actuated using the black thumb button on the mouse. If the wire bonder does not respond to pushing this button, the most likely cause is that the wire end does not have a proper ball. This will be indicated by the OPEN light being lit. The solution is to create a new ball using the procedure described in the manual on p. 6-23. Getting the wire through the capillary is an exercise in patience. The wire loading tips on p. 5-12 of the manual may be helpful.

If the capillary does not reach the surface to be bonded, or if the capillary does not rise from the surface after the first bond is made, the workholder height needs to be adjusted. This adjustment is described in the manual on p. 5-10.

C.5 Conclusion

The wire bonder may be intimidating at first, but with practice it is actually fairly easy to use. Also, the operating manual is fairly comprehensive and easy to follow. This guide is intended to supplement the manual by pointing out particularly helpful sections of the manual and by recommending a few techniques not covered in the manual.

APPENDIX D:

MS3110 capacitive readout integrated circuit

Electronic readout of the MEMS device's response to sound has been achieved using the Micro Sensors, Inc. MS3110 Capacitive Readout Integrated Circuit (IC). This IC (pictured in Figure D.1) consists of a 16-pin chip in a dual inline package, and a separate evaluation board (pictured in Figure D.2) that the package may be mounted on to facilitate experimentation. The specifications and instructions for operation are contained in the MS3110 documentation and will not be repeated here. However, there are some lessons learned that are specific to operation of the MS3110 with the MEMS acoustic direction finding sensor. These include some tips on balancing the capacitance bridge circuit and some conflicts with the laser vibrometer software.



Figure D.1: The MS3110 as used in the evaluation board.

Balancing the trim capacitors is not always straightforward, especially if the reference capacitors are not well matched to the device comb fingers. If there is a large mismatch, the MS3110 trim capacitors may not have enough range to balance the circuit. However, there is a solution. When using the evaluation board, it should be possible to balance the circuit by inserting an external capacitor between the CSCOM and either CS1 or CS2 as shown in Figure D.2. By choosing a different size capacitor, e.g. 10 pF or 18 pF, and trying the CS1 or CS2 sides in turn, it should be possible to balance the circuit. Once the circuit is balanced using this technique, it should balance from then on using the same external capacitor configuration.

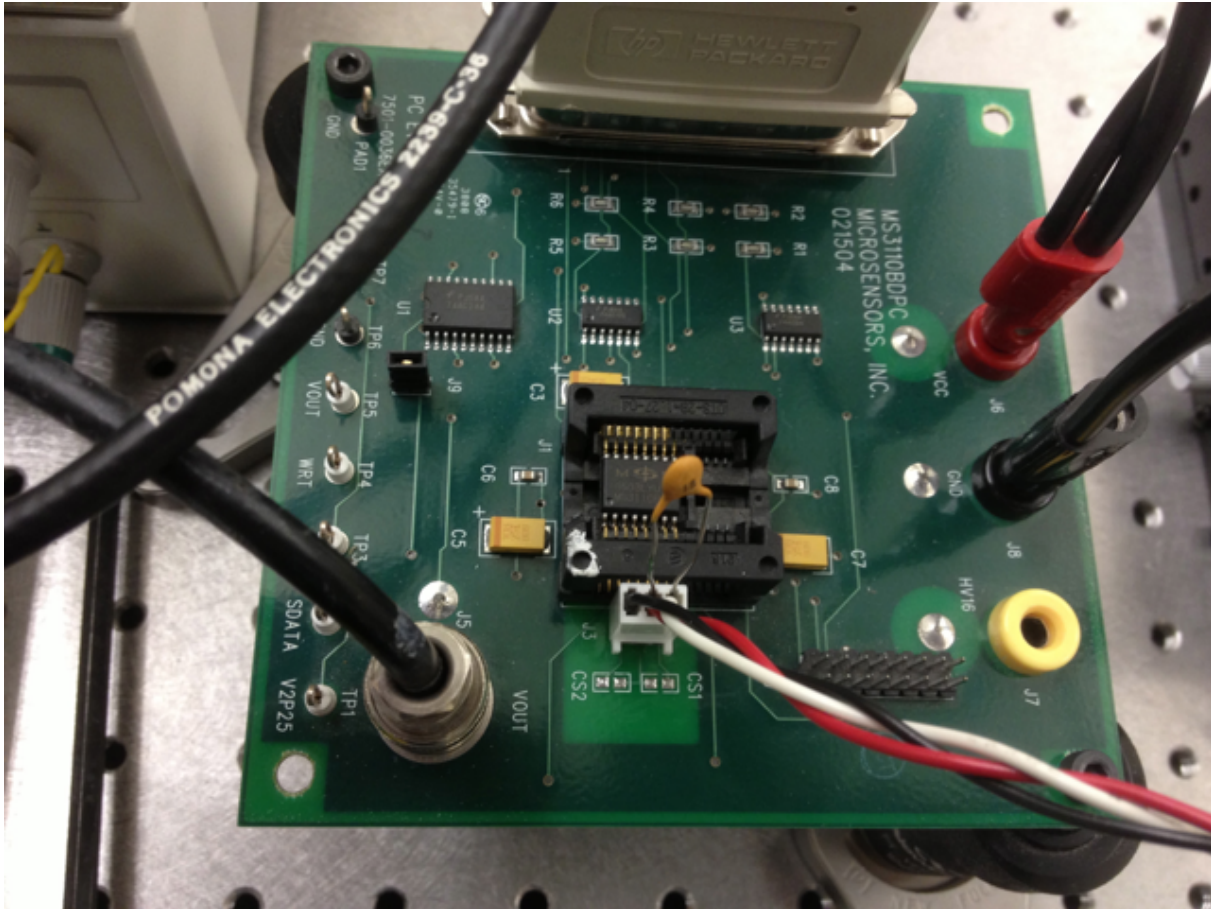


Figure D.2: The MS3110 evaluation board, with an external capacitor connected between the CSCOM and CS1 pins (red and white wires).

A second challenge in using the MS3110 arises when the evaluation board is connected to a computer also running the VibSoft 4.7 vibrometer software. For unknown reasons, certain actions in the vibrometer software can cause the MS3110 to behave erratically. When using both applications simultaneously, it is advisable to check the MS3110 output signal after conducting operations in the VibSoft application. If the MS3110 had been operating normally, but is no longer producing the expected output, rewriting the control registers should correct the situation. Alternatively, if the desired control parameters have been programmed into the MS3110's read-only memory, then a chip reset should also correct the situation.

In conclusion, the primary source of information on the MS3110 is the operation manual. This guide may be of some additional help in using the MS3110 with the acoustic direction-finding sensor.

APPENDIX E:

Light and the sound sensor

In the course of this research, it was discovered that intense light may affect the capacitive readout system of the acoustic DF sensor. In particular, if the laser vibrometer was aimed at the comb finger bank being used for readout, then interrupting the light had a dramatic effect on the circuit balance. For devices with two wings, aiming the laser at the wing opposite to the comb finger bank in use has a smaller but still observable effect on the readout circuit.

It is likely that this effect of laser light is due to the doped silicon of the device acting as a photodiode. Intense light increases the conductivity and thus the capacitance of the illuminated comb finger bank. Since the reference bank is not illuminated by the narrow laser beam, its capacitance remains steady and the capacitance bridge becomes unbalanced.

In contrast to laser light, ambient light does not have a significant effect on the capacitive readout circuit. This was confirmed by turning off the laboratory room lighting and observing no change in circuit balance. One likely reason is that the ambient light is less intense than laser light. A second reason is that ambient light tends to illuminate both the device capacitor bank and the reference bank equally. Thus any light-induced capacitance change in one bank is matched with an equal change in the other bank, and the circuit balance is not affected.

THIS PAGE INTENTIONALLY LEFT BLANK

APPENDIX F:

Analytical treatment of fringe fields

This appendix presents an analytical method to include the fringe fields (edge effects) in an estimate of the capacitance of offset plates, as in the capacitive readout of the fly-ear sensor. The analysis is due to A. E. H. Love [58], but it is supplemented with MATLAB scripts to carry out Love's calculations and COMSOL simulations to verify the accuracy of the results.

When designing or characterizing a capacitive comb finger readout system, it may be useful to include the fringe field effects in an analytical model of capacitance. Usually a finite-element model (FEM) will provide the most accurate estimate, as seen in Ch. 3, but in some cases an analytical approach is desired. For a fully aligned parallel-plate capacitor, the fringe field can be estimated by several means as described in a technical report by Leus and Elata [59]. This report compares various approximate computations of the capacitance of parallel plates. However, in the case of the acoustic DF sensor, the plates are generally not completely aligned (overlapped). In this case a different approach is required.

Approximations for the capacitance of offset plates can be found in a paper published in 1924 by A. E. H. Love [58]. This paper uses conformal mapping to estimate the capacitance between two upright plates of height $2b$, separated by a horizontal gap $2h$ and offset or displaced by a vertical distance d . Derivations for various relative magnitudes of d , $2b$, and h are found in [58, Sec. 7-9]. The derivations are complicated, but the results can be used without following every detail and may be verified using FEM. It is particularly helpful that some computed examples are provided to assist the reader. In these sections formulas are given to approximate the capacitance per unit length for three regimes of plate dimensions and displacement, all of which may be relevant to the capacitive readout system. These regimes are:

- (Sec. 7) The displacement or offset is of the same order as the capacitor gap.
- (Sec. 8) The displacement is large compared to the gap, but the overlapped length of the plates is still substantially larger than the gap.
- (Sec. 9) Both displacement and overlap may be of the same order as the gap.

In each case, the capacitance per unit length is given as $K'/(4\pi K)$ in Gaussian units, where K' and K depend on the plate configuration and dimensions. In SI units this result is multiplied by $4\pi\epsilon_0$ to obtain

$$c = \epsilon_0 K' / K. \quad (\text{F.1})$$

In the following sections are presented MATLAB functions to compute the capacitance according to the three regimes described above. In each case, the MATLAB function produces results identical to those in [58]. Also, in each case a COMSOL FEM is used to verify the results. Unlike in the theory, in the COMSOL model the capacitor plates are given a non-zero thickness which results in slightly greater capacitance.

F.1 Small displacement

In the first case, for small displacement, the capacitance is given by the equation at the top of [58, p. 348]:

$$\frac{K'}{K} = \frac{b}{h} \left\{ 1 + \frac{h}{\pi b} \left(2 - \cosh \gamma + \log \frac{2\pi b}{h} \right) \right\}, \quad (\text{F.2})$$

where \log represents the natural logarithm and γ is found by solving the transcendental equation

$$\gamma + \sinh \gamma = \frac{\pi d}{2h}. \quad (\text{F.3})$$

Note that the term in curly braces is a correction factor that is multiplied by the elementary capacitance per unit length $c = \epsilon_0 b/h$ to get the approximate capacitance including fringe field effects. The following MATLAB function performs these computations, taking as inputs the dimensions b , h , and d .

```
function capacitance = smalloffset(b,h,d)

gamma=zeros(1,length(d));
for i=1:length(d)
    f=@(g) g+sinh(g)-pi.*d(i)/(2*h); % finding zeros of f solves for gamma
    gamma(i)=fzero(f,1);             % find zeros of f
end

capacitance = ...                    % in picofarads
    8.854188*(b/h)*( 1+( h/pi/b ).*( 2-cosh(gamma)+log( 2*pi*b/h ) ) );
```

The output of this function is the total capacitance of the plates including fringe field effects. We can check this function by comparing to the example given in Love's paper. He mentions that "if $b/h = 100$, the change in K'/K as d increases from 0 to h is a decrease from 102.37 to 102.27." The MATLAB function produces the same results. Also, a COMSOL simulation with $2b = 200\mu\text{m}$ (and therefore $2h = 2\mu\text{m}$), and plate thickness of $0.1\mu\text{m}$, produces similar results: as d increases from 0 to h , the capacitance decreases from $1.0244\epsilon_0$ to $1.0235\epsilon_0$. As mentioned earlier, the higher capacitance in the COMSOL simulation can be attributed to the non-zero plate thickness.

F.2 Large displacement, large overlap

The second regime is where the displacement is large compared to the capacitor gap but the remaining overlap between plates is still large compared to the gap between them; specifically where $b - d/2$ and d are both large compared to h [58, Sec. 8]. In this case the capacitance is given at the top of [58, p. 350] as

$$\frac{K'}{K} = \frac{b - d/2}{h} \left[1 + \frac{2h}{\pi(b - d/2)} \left\{ 1 + \log(2\beta_2 \sqrt{K'}) \right\} \right], \quad (\text{F.4})$$

where the parameter β_2 is found by solving the two equations at the bottom of p. 349 as follows. First β_1 is approximated by solving

$$\frac{4\beta_1^2 K' + 1}{4\beta_1^2 K' - 1} = \frac{b + d/2}{b - d/2} \quad (\text{F.5})$$

in terms of K' , and then β_2 is approximately

$$\beta_2 = \frac{4\beta_1 K'}{4\beta_1^2 K' - 1}. \quad (\text{F.6})$$

With β_2 thus approximated in terms of K' , Eq. (F.4) still contains K' on the right-hand side. However, on the right K' can be approximated as $\pi(b - d/2)/(2h)$ [58]. The following MATLAB function performs these computations.

```
function corr = largeoffsetlargeoverlap(b,h,d)

KprimeApprox = pi*(b-d/2)/(2*h);      % used in RHS of Love's equation
beta1 = sqrt( b/( 2*d*KprimeApprox ) );
```

```

beta2 = 4*beta1*KprimeApprox/( 4*beta1^2*KprimeApprox-1 );

corr = 1+2*h/( pi*( b-d/2 ) )*( 1+log( 2*beta2*sqrt(KprimeApprox) ) );

```

This function's output is the factor in square brackets on the right-hand side of Eq. (F.4). Sample values of this factor are tabulated at the end of [58, Sec. 8]. Note that there is a typographical error in this table: the label d/b in the upper left corner should read $d/2b$, where $2b$ is the full height of the plates. The above MATLAB script returns the tabulated values exactly, and the COMSOL simulation returned values differing by less than 0.3% from these values.

F.3 Large displacement, small overlap

The third and last regime of interest computed by Love is for relatively short plates with a large offset; specifically, where the displacement or offset d is large compared to the gap, but the remaining overlap $2b - d$ is not [58, Sec. 9]. Once again the capacitance is $c = \epsilon_0 K'/K$, where in this regime K is approximately $\pi/2$ and K' is found as follows. First the quantity v_2 is found by solving the transcendental equation found near the top of p. 351:

$$\frac{b-d/2}{h} = \frac{2}{\pi} (v_2 - \coth 2v_2). \quad (\text{F.7})$$

With v_2 thus known, K' is given by the last equation on the same page:

$$e^{K'} = \frac{\pi\sqrt{2}\sinh 2v_2}{\sqrt{\cosh 2v_2}} \frac{b+d/2}{h}. \quad (\text{F.8})$$

The following MATLAB function performs these computations.

```

function capacitance = largeoffsetsmalloverlap(b,h,d)

f=@(v2) -( b-d/2 )/h+2/pi*( v2-coth(2*v2) );
v2solution=fzero(f,1); % find zeros of f

Kprime=log( pi*sqrt(2)*sinh(2*v2solution)/sqrt( cosh(2*v2solution) )*...
    ( b+d/2 )/h );

capacitance = 8.854188*Kprime/( pi/2 ); % in picofarads

```

As an example, Love states that if the offset is complete so that the overlap is exactly zero, and $b/h = 100$, then the value of K' is 7.4516 and the corresponding value of K'/K is 4.74. The above MATLAB function produces the same result, and the COMSOL simulation returned a capacitance of $4.875\epsilon_0$ which is in reasonably good agreement.

THIS PAGE INTENTIONALLY LEFT BLANK

REFERENCES

- [1] R. N. Miles, D. Robert, and R. R. Hoy, “Mechanically coupled ears for directional hearing in the parasitoid fly *Ormia ochracea*,” *Journal of the Acoustical Society of America*, vol. 98, no. 6, pp. 3059–3070, Dec. 1995.
- [2] D. Robert, R. N. Miles, and R. R. Hoy, “Directional hearing by mechanical coupling in the parasitoid fly *Ormia ochracea*,” *Journal of Comparative Physiology A*, vol. 179, no. 1, pp. 29–44, 1996.
- [3] D. Robert, R. N. Miles, and R. R. Hoy, “Tympanal mechanics in the parasitoid fly *Ormia ochracea*: intertympanal coupling during mechanical vibration,” *Journal of Comparative Physiology A*, vol. 183, no. 4, pp. 443–452, 1998.
- [4] A. C. Mason, M. L. Oshinsky, and R. R. Hoy, “Hyperacute directional hearing in a microscale auditory system,” *Nature*, vol. 410, pp. 686–690, Apr. 2001.
- [5] M. Denny, “Physics between a fly’s ears,” *European Journal of Physics*, vol. 29, no. 5, pp. 1051–1057, 2008.
- [6] R. N. Miles and R. R. Hoy, “The development of a biologically-inspired directional microphone for hearing aids,” *Audiology and Neuro-otology*, vol. 11, no. 2, pp. 86–94, 2006.
- [7] M. Touse, J. Sinibaldi, K. Simsek, J. Catterlin, S. Harrison, and G. Karunasiri, “Fabrication of a microelectromechanical directional sound sensor with electronic readout using comb fingers,” *Applied Physics Letters*, vol. 96, no. 17, pp. 173701(1-3), 2010.
- [8] C. Gibbons and R. N. Miles, “Design of a biomimetic directional microphone diaphragm,” in *Proc. Int. Mech. Eng. Congr. and Expo. (IMECE)*, Orlando, FL, 2000.
- [9] R. N. Miles, S. Sundermurthy, C. Gibbons, R. R. Hoy, and D. Robert, “Differential microphone,” U.S. Patent 6 788 796 B1, Sept. 7, 2004.
- [10] A. Saito, N. Ono, and S. Ando, “Micro gimbal diaphragm for sound source localization with mimicking *Ormia Ochracea*,” in *Proc. 41st Soc. Instrument and Control Eng. Annu. Conf.*, Osaka, 2002, pp. 2159–2162.

- [11] N. Ono, A. Saito, and S. Ando, "Design and experiments of bio-mimicry sound source localization sensor with gimbal-supported circular diaphragm," in *TRANSDUCERS, Solid-State Sensors, Actuators and Microsystems, 12th Int. Conf. on*, vol. 1, 2003, pp. 935–938.
- [12] R. N. Miles, Q. Su, W. Cui, M. Shetye, F. L. Degertekin, B. Bicen, C. Garcia, S. Jones, and N. Hall, "A low-noise differential microphone inspired by the ears of the parasitoid fly *Ormia ochracea*," *Journal of the Acoustical Society of America*, vol. 125, no. 4, pp. 2013–2026, Apr. 2009.
- [13] K. Yoo, C. Gibbons, Q. T. Su, R. N. Miles, and N. C. Tien, "Fabrication of biomimetic 3-D structured diaphragms," *Sensors and Actuators A-Physical*, vol. 97–98, pp. 448–456, 2002.
- [14] L. Tan, R. N. Miles, M. G. Weinstein, R. A. Miller, Q. T. Su, W. L. Cui, and J. Gao, "Response of a biologically inspired MEMS differential microphone diaphragm," in *Proc. SPIE 4743, Unattended Ground Sensor Technologies and Applications IV*, Orlando, FL, 2002.
- [15] W. L. Cui, B. Bicen, N. Hall, S. A. Jones, F. L. Degertekin, and R. N. Miles, "Optical sensing in a directional mems microphone inspired by the ears of the parasitoid fly, *Ormia ochracea*," in *MEMS 2006: 19th IEEE Int. Conf.*, Istanbul, 2006, pp. 614–617.
- [16] P.-H. Sung, J.-Y. Chen, K.-H. Yen, and C.-Y. Wu, "CMOS compatible directional microphone," in *Int. Conf. Microsystems, Packaging, Assembly and Circuits Technology*, Taipei, 2007, pp. 149–152.
- [17] P. An, W. Yuan, and R. Sen, "MEMS biomimetic acoustic pressure gradient sensitive structure for sound source localization," *Sensors*, vol. 9, no. 7, pp. 5637–5648, July 2009.
- [18] A. P. Lisiewski, H. J. Liu, M. Yu, L. Currano, and D. Gee, "Fly-ear inspired micro-sensor for sound source localization in two dimensions," *Journal of the Acoustical Society of America*, vol. 129, no. 5, pp. E166–E171, May 2011.
- [19] C.-C. Chen and Y.-T. Cheng, "Physical analysis of a biomimetic microphone with a central-supported (C-S) circular diaphragm for sound source localization," *Sensors Journal, IEEE*, vol. 12, no. 5, pp. 1504–1512, 2012.
- [20] H. J. Liu, M. Yu, and X. M. Zhang, "Biomimetic optical directional microphone with structurally coupled diaphragms," *Applied Physics Letters*, vol. 93, no. 24, Dec. 2008.

- [21] H. Liu, L. Currano, D. Gee, B. Yang, and M. Yu, "Fly-ear inspired acoustic sensors for gunshot localization," in *Proc. SPIE 7321, Bio-Inspired/Biomimetic Sensor Technologies and Applications*, pp. 73210A(1-10), 2009.
- [22] H. J. Liu, M. Yu, L. Currano, and D. Gee, "Fly-ear inspired miniature directional microphones: Modeling and experimental study," in *ASME Int. Mech. Eng. Congr. & Expo.*, Lake Buena Vista, FL, 2009.
- [23] H. Liu and M. Yu, "A new approach to tackle noise issue in miniature directional microphones: bio-inspired mechanical coupling," in *SPIE 7647, Sensors and Smart Structures Technologies for Civil, Mechanical, and Aerospace Systems*, San Diego, CA, 2010, pp. 76470P (1–9).
- [24] H. Liu and M. Yu, "Effects of air cavity on fly-ear inspired directional microphones: a numerical study," in *Proc. SPIE 7981, Sensors and Smart Structures Technologies for Civil, Mechanical, and Aerospace Systems*, San Diego, CA, 2011, pp. 79811V(1–9).
- [25] E. C. Hannah, "MEMS directional sensor system," U.S. Patent 7 146 014 B2, Dec. 5, 2006.
- [26] M. Akçakaya and A. Nehorai, "Biologically inspired coupled antenna beampattern design," *Bioinspiration & Biomimetics*, vol. 5, no. 4, 2010.
- [27] M. Akçakaya, C. H. Muravchik, and A. Nehorai, "Biologically inspired coupled antenna array for direction-of-arrival estimation," *Signal Processing, IEEE Transactions on*, vol. 59, no. 10, pp. 4795–4808, 2011.
- [28] N. Behdad, M. A. Al-Joumayly, and M. Li, "Biologically inspired electrically small antenna arrays with enhanced directional sensitivity," *Antennas and Wireless Propagation Letters, IEEE*, vol. 10, pp. 361–364, 2011.
- [29] M. Touse, "Design, fabrication, and characterization of a microelectromechanical directional microphone," Ph.D. dissertation, Naval Postgraduate School, 2011.
- [30] T. J. Shivok, "MEMS POLYMUMPS-based miniature microphone for directional sound sensing," Master's thesis, Naval Postgraduate School, 2009.
- [31] S. C. W. Harrison, "Free field modeling of a MEMS-based pressure gradient microphone," Master's thesis, Naval Postgraduate School, 2009.

- [32] D. Grevenitis, "Effects of substrate on response of MEMS directional sound sensor," Master's thesis, Naval Postgraduate School, 2010.
- [33] D. D. Davis, "Characterization of the MEMS directional sound sensor in the high frequency (15 - 20 kHz) range," Master's thesis, Naval Postgraduate School, 2012.
- [34] C. W. Lim, "Designing an electronic readout for a directional micro electrical-mechanical (MEMS) sound sensor," Master's thesis, Naval Postgraduate School, 2012.
- [35] J. D. Roth, "Integration of a high sensitivity MEMS directional sound sensor with readout electronics," Master's thesis, Naval Postgraduate School, 2012.
- [36] A. Cowen, G. Hames, D. Monk, S. Wilcenski, and B. Hardy, *SOIMUMPs Design Handbook: a MUMPs® process*, MEMSCAP Inc., 2002–2011, revision 8.0.
- [37] R. H. Downey, L. N. Brewer, and G. Karunasiri, "Determination of mechanical properties of a MEMS directional sound sensor using a nanoindenter," *Sensors and Actuators A-Physical*, vol. 191, pp. 27–33, March 2013.
- [38] R. Downey, L. Brewer, and G. Karunasiri, "Nanoindenter stiffness measurements on a MEMS sound sensor," *Bulletin of the American Physical Society*, vol. 57, 2012.
- [39] R. H. Downey and G. Karunasiri, "Acoustic direction-finding MEMS sensor with branched comb fingers," February 2013, submitted to *Journal of Microelectromechanical Systems*.
- [40] T. P. Weihs, S. Hong, J. C. Bravman, and W. D. Nix, "Mechanical deflection of cantilever microbeams - a new technique for testing the mechanical properties of thin films," *Journal of Materials Research*, vol. 3, no. 5, pp. 931–942, Sep-Oct 1988.
- [41] H. Lee, R. A. C. Jr, S. Mall, and P. E. Kladitis, "Nanoindentation technique for characterizing cantilever beam style RF microelectromechanical systems (MEMS) switches," *Journal of Micromechanics and Microengineering*, vol. 15, pp. 1230–1235, 2005.
- [42] A. Koszewski, D. Levy, and F. Souchon, "Study of mechanical properties of RF MEMS switches by nanoindentation: characterization and modeling of electro-mechanical behavior," *Sensors and Actuators A-Physical*, vol. 163, no. 1, pp. 205–212, Sep. 2010.

- [43] A. Broue, T. Fourcade, J. Dhennin, F. Courtade, P.-L. Charvet, P. Pons, X. Lafontan, and R. Plana, “Validation of bending tests by nanoindentation for micro-contact analysis of MEMS switches,” *Journal of Micromechanics and Microengineering*, vol. 20, no. 8, Aug. 2010.
- [44] L. Chen, R. Ballarini, H. Kahn, and A. H. Heuer, “Bioinspired micro-composite structure,” *Journal of Materials Research*, vol. 22, no. 1, pp. 124–131, Jan. 2007.
- [45] Y. Wu, C. Zhang, H. Wang, and G. Ding, “Torsion/cantilever-based MEMS bistable mechanisms with different support configurations: Structure design and comparison,” *Journal of Micromechanics and Microengineering*, vol. 21, no. 4, Apr. 2011.
- [46] J. D. Holbery, V. L. Eden, M. Sarikaya, and R. M. Fisher, “Experimental determination of scanning probe microscope cantilever spring constants utilizing a nanoindentation apparatus,” *Review of Scientific Instruments*, vol. 71, no. 10, pp. 3769–3776, Oct. 2000.
- [47] M. A. Hopcroft, W. D. Nix, and T. W. Kenny, “What is the Young’s modulus of silicon?” *Journal of Microelectromechanical Systems*, vol. 19, no. 2, pp. 229–238, Apr. 2010.
- [48] C. Liu, *Foundations of MEMS*, 1st ed., ser. Illinois ECE Series. Upper Saddle River, New Jersey: Pearson Education, Inc., 2006.
- [49] W. C. Young, *Roark’s Formulas for Stress and Strain*, 7th ed. McGraw-Hill, 2002.
- [50] *Agilent Technologies G200 Nanoindenter: User’s Guide*, Agilent Technologies, Inc., 2009, manual part number G2A-13192-1.
- [51] W. C. Oliver and G. M. Pharr, “Measurement of hardness and elastic modulus by instrumented indentation: Advances in understanding and refinements to methodology,” *Journal of Materials Research*, vol. 19, no. 1, Jan. 2004.
- [52] K. E. Petersen, “Silicon as a mechanical material,” *Proceedings of the IEEE*, vol. 70, no. 5, pp. 420–457, 1982.
- [53] L. E. Kinsler, A. R. Frey, A. B. Coppens, and J. V. Sanders, *Fundamentals of Acoustics*. Hoboken, NJ: John Wiley & Sons, Inc., 2000.
- [54] A. Cowen, private communication, March 2013.

- [55] V. L. Rabinovich, R. K. Gupta, and S. D. Senturia, "The effect of release-etch holes on the electromechanical behaviour of MEMS structures," in *Transducers '97: Int. Conf. Solid-State Sensors and Actuators*, vol. 2, Chicago, 1997, pp. 1125–1128.
- [56] W. Zhang and K. Turner, "Frequency dependent fluid damping of micro/nano flexural resonators: Experiment, model and analysis," *Sensors and Actuators A–Physical*, vol. 134, pp. 594–599, 2007.
- [57] T. Klose, H. Conrad, T. Sandner, and H. Schenk, "Fluidmechanical damping analysis of resonant micromirrors with out-of-plane comb drive," in *Proc. COMSOL Conf.*, Hannover, 2008. [Online]. Available: <http://www.comsol.dk/papers/5208/download/Klose.pdf>
- [58] A. E. H. Love, "Some electrostatic distributions in two dimensions," *Proceedings of the London Mathematical Society*, vol. S2-22, no. 1, pp. 337–369, 1924.
- [59] V. Leus and D. Elata, "Fringing field effect in electrostatic actuators," Technion – Israel Institute of Technology, Tech. Rep. ETR-2004-2, May 2004. [Online]. Available: <http://meeng.technion.ac.il/Research/TReports/2004/ETR-2004-02.pdf>

Initial Distribution List

1. Defense Technical Information Center
Ft. Belvoir, Virginia
2. Dudley Knox Library
Naval Postgraduate School
Monterey, California